Advanced Mechanical Design, University of Rochester
Final Design Report
Spring 2024

L3HARRIS – 3D METAL-PRINTED SECONDARY MIRROR SUPPORT STRUCTURE

Alex Nagy **Calvin Tourangeau** **Declan Bhagwat** **Noah Schloff** **Shelinee Hernandez Espino**

ABSTRACT

Additive manufacturing is an emerging technology that increases the efficiency and lowers the costs of production within the aerospace industry. Companies like L3Harris have begun embracing the capabilities of manufacturing satellite components using this technique. The goal of this project is to design and develop a Secondary Mirror Support Structure (SMSS) that can be fabricated using additive manufacturing, more specifically 3D metal printing. To meet the goals of this project, the team continued from last year's accomplishments to help influence our initial concept designs. Then a combination of topology, shape, and sizing optimization was used to further progress our designs towards the requirements and specifications outlined by the project sponsor, L3Harris. After reviewing the previous team's findings, this year's design progression centered around the use of shelled models – focusing on the load-bearing geometry of the structure rather than internal lattice supports. This report will highlight the iterative design process, finite element analysis (FEA), manufacturing, printability, and supporting testing results. These techniques combined to a model that met all the provided requirements and specifications.

PROBLEM DEFINITION

Lightweight Secondary Mirror Support Structures (SMSS) require affordable, fast, and structurally sound manufacturing methods, such as additive manufacturing, to precisely align optical components without obstructing the field of view. These mounts are crucial in the advancement of imaging technology; without them, knowledge of both the earth and deep space would not be able to grow at the rate it has in this millennium. Current solutions for SMSS include using a graphite composite layup which is incredibly expensive and time consuming to produce. Improving additive manufacturing methods for SMSS is crucial for the next step in aerospace development. It is one of the most tightly toleranced parts of satellites, so being able to manufacture them with 3D printing will decrease satellite manufacturing time, increase reliability, and increase production.

REQUIREMENTS, SPECIFICATIONS, DELIVERABLES

The requirements, specifications, and deliverables for the project were provided by the project sponsor, L3Harris. After the team reviewed and discussed these project expectations with L3Harris, the team agreed to satisfy all outlined requirements, specifications, and deliverables. In addition, the team requested to add one more deliverable which was the 3D printed material coupon testing results. The requirements, specifications, and deliverables are noted in the following lists.

<u>Requirements</u>

1. The project scope is the design, analysis, and prototype of the SMSS only.
2. The project shall focus on additive manufacturing solutions to the problem statement.
3. The SMSS shall provide interfaces for and support the secondary mirror and mounts, actuator assembly, shade assembly, and all miscellaneous thermal hardware.
4. The design shall be producible with additive manufacturing methods.
5. The following design factors of safety shall be used in analysis:
    a. Yield: 2.0
    b. Micro-Yield: 1.0
    c. Ultimate: 2.5
    d. Buckling: 4.0
6. The following mass contingency factors shall be used:
    a. Concept design: 20%
    b. Preliminary design: 15%
    c. Final Design: 10%
    d. Post Final Design: 5%
    e. Measured hardware: 0.10%
7. There shall be no trapped cavities in the SMSS.

Specifications

TABLE 1
SPECIFICATIONS AND VERIFICATION

Specification	Verification
1. The outer diameter of the SMSS (interface to the FMS) shall be 48 inches.	An NX sketch of a 48-inch circle around the model will confirm the diameter of the SMSS.
2. The SMSS shall interface to the Forward Metering Structure (FMS) at three locations 120 degrees apart.	The FARO Quantum Max ScanArm will confirm the angles between each mount pad.
3. The first mode of the SMSS shall be 120 Hz or greater when grounded at the FMS interface and supporting all hosted hardware.	NX modal analysis will be used to confirm the first mode of vibration.
4. The mass of the SMSS shall be 18 lbm or less.	The model will be inspected in NX to confirm the mass.
5. The SMSS shall have positive margins of safety against yield and ultimate failure when exposed to a quasi-static load of 12 G laterally and 18 G axially simultaneously (lateral swept 15° increments) combined with a 5°C to 35°C temperature range (nominal room temp is 20°C) while supporting all hosted hardware.	NX will be used to display the yield and ultimate stress for the launch loads described, and then a margin of safety calculation will be performed to ensure positive margins in the worst-case load environment.
6. The SMSS and hosted hardware shall not obstruct more than 14% of the Primary Mirror (PM) clear aperture area (assume 1.1 m diameter clear aperture).	NX will be used to calculate the area of the PM covered by the SM and SMSS.
7. The SMSS shall provide a stable mounting platform for the Secondary Mirror (SM) in thermal environments. The average motion of the SM interfaces under a 1°C isothermal load should be 0.66 micro-inches translation (RSS of X and Y) or less and 0.037 micro-radians rotation (RSS of Rx and Ry) or less.	The model will be simulated in NX to find the translational and rotational displacements of the SM under 1°C isothermal loading.

Deliverables

1. CAD file prototypes with 2D drawings in NX and a finite element model (FEM) in Nastran of the SMSS.
2. A final design report.
3. Host design review meetings and provide supporting slides for L3Harris.
4. A concept design review, preliminary design review, and final design review.
5. The creation of a 3D-printed model of the SMSS which can be scaled and composed of a material of choice.
6. Test results of 3D-printed material coupons.
7. Model validation of the 3D-printed model.

The work breakdown structure and critical path plan that were developed to accomplish these specifications and deliverables are present in Appendix A, Figures 1, 2, and 3.

CONCEPTS

The team created several concept sketches of a potential SMSS which were then created as CAD models with corresponding Finite Element Model (FEM) analysis. Concept 1, as seen in Appendix B, Figure 1, followed the design concept of last year's design. The dimensions throughout the design were similar to last year's model. The design was also shelled to minimize weight, leaving only a thin wall of material on the outer edges of the structure, similar to a box beam. The shell concept slightly differs from last year's model because their model was shelled with interior lattice support while this year's concepts were all hollowed out on the inside. Concept 1 served as the baseline for the concept selection process. All other concepts were shelled in a similar manner to minimize the mass of the SMSS for a more representative comparison during the selection process.

Concept 2, as seen in Appendix B, Figure 2, incorporated I-beams to the concept 1 design with the intent to increase structural stiffness for bending and shear stress. There was also additional material removed at the triangular cut outs of the leg interfaces to reduce the weight of the SMSS. While the flanges of the I-beam were kept solid, the web portion of the structure was shelled throughout.

Concept 3, as seen in Appendix B, Figure 3, applied the idea of a circular center with the intent of reducing the weight of the SMSS and reducing the area of obstruction for the field of view. The design also incorporated legs which would interface tangent to the circular center. These considerations were intended to reduce the displacement of the SM under a temperature load. With a circular center and legs tangent to the center, the translation and rotation of the SM would likely be concentrated in and about the Z direction, reducing translation and rotation of the SM in and about the X and Y.

Concept 4, as seen in Appendix B, Figure 4, attempted to incorporate aspects of the previous three concepts. The legs of the structure tapered out from the mount face and interfaced with the center at an offset angle, similar to concept 3's legs. The intent was to retain some of the stiffness from concept 3 that was anticipated during a temperature load. In addition, material in the central portion of the legs was removed to reduce weight and reduce the projected area of obstruction, similar to how concept 1 and concept 2 removed material at the leg interfaces.

Concept 5, as seen in Appendix B, Figure 5, incorporated a circular center with legs interfacing tangent to the center, similar to concept 4. The legs were also constructed to mimic I-beams with the intent to increase the stiffness of the SMSS, similar to concept 2. The design looked to address the strength of the structure while enduring launch loads and the displacements of the SM under temperature loads while in orbit. The flanges of the I-beam legs were kept solid, and the web portion was shelled in addition to the remainder of the structure.

Once each of the concepts had a corresponding FEM created, the modal analysis, launch load analysis, and temperature load analysis solutions were created. For consistent comparison of each concept's performance, each model applied the same mesh type, material, loads, and boundary conditions. The loads and boundary conditions were applied to each SMSS's FEM as outlined by the requirements and specifications provided by the sponsor, L3Harris. The team determined several performance measurements from the FEM solutions which would inform the concept selection process and were based on the requirements and specifications provided. The performance measurements included the following: a yield stress margin of safety calculation using NX's Aluminum-6061 and the model's worst case von Mises stress load case with a factor of safety of 2, the Root Sum Squared (RSS) of the SM's translation in the X and Y directions under a 1°C isothermal load, the RSS of the SM's rotation about the X and Y directions under a 1°C isothermal load, the mass of the SMSS, and the first mode of vibration of the SMSS. The resulting performance measurement values are shown below in Table 2.

TABLE 2
CONCEPT PERFORMANCE EVALUATION

Concept Performance					
	1	**2**	**3**	**4**	**5**
Margin of Safety	-0.5979	-0.7175	-0.1929	-0.7346	-0.2218
RSS of SM Translation (in)	3.18E-6	3.92E-6	8.68E-8	3.67E-6	8.49E-7
RSS of SM Rotation (rad)	7.90E-7	3.17E-7	2.99E-8	2.58E-6	2.19E-7
Mass (lbm)	25.48	22.74	18.16	19.71	24.90
First Mode (Hz)	154.99	162.83	119.71	175.11	135.80

After collecting and documenting all performance measurements from each concept, the team compared the concepts using a Pugh matrix. The criteria used in the Pugh matrix were manufacturability, strength, thermal stability, mass, and modal frequency. The team deemed these criteria to be the most indicative of a concept's potential to satisfactorily meet the requirements and specifications as the design process continued. The manufacturability of the structure using additive manufacturing techniques was a critical focus for the project. Printing structures with overhang angles or sharp corners decreases the feasibility of a print while increasing the print time, complexity, and potential of failure. Additionally, the structure must be capable of enduring all launch loads without failure. The strength of the structure was determined by the margin of safety value which measures the amount of overdesign, or in this case under design, with respect to the highest stresses in the structure. Furthermore, the thermal stability of the SMSS while supporting all hosted hardware is crucial for the alignment of the SM. Any displacement that would cause the SM to be misaligned with respect to the PM and detector would prove to be detrimental to the performance of the system. Lateral translations, tipping, or tilting of the SM would put the image out of focus or direct a fraction of the light away from the detector. The thermal stability criterion was determined by the RSS of the translation and rotation of the SM while the SMSS is in orbit. Lower translation and rotation values indicated a more favorable concept. The mass of the SMSS was also an important consideration because a heavier model would require more material, and in turn, cost more to manufacture. The last consideration for the Pugh matrix was the modal frequency of each SMSS. The modal frequency is a strong indication of the stiffness of the structure and a minimum first mode of vibration was noted in the specifications. A higher first mode indicated a more favorable concept due to more potential for optimization of the design. The completed Pugh matrix is shown below in Table 3.

TABLE 3
PUGH MATRIX FOR CONCEPT SELECTION

Pugh Matrix					
	1	**2**	**3**	**4**	**5**
Manufacturability	0	-	-	0	-
Strength	0	-	+	-	+
Thermal Stability	0	+	+	-	0
Mass	0	+	+	-	+
Modal Frequency	0	+	-	+	-
TOTAL	0	1	1	-2	0

Based on the Pugh matrix comparison criteria, informed by the concept performance measurements, concepts 2 and 3 proved to be the most promising for the team to move forward with for continued optimization of the SMSS design. The team decided to continue the design progression with both concepts until one displayed a clearer advantage from the FEM analysis.

MECHANICAL ANALYSIS

Once the initial concepts were created, Finite Element Analysis (FEA) was performed on the models to determine how they performed with respect to the specifications provided. NX was used to create a FEM of all the designs and see how the structure performed under the launch and orbital loads. Many obstacles were encountered in the creation of these models due to the complexity of the parts and the many features available in NX's FEA software. The first decision was deciding what mesh type to use, a 2D shell mesh composed of layers of square elements, or a 3D solid mesh composed of ten sided tetrahedral elements. At first, a 2D shell mesh was used, but the software was struggling to analyze a closed shell model correctly as it kept mistaking the box beam for a solid structure and not correctly solving the mesh. Because of this and the simplicity of using a 3D mesh, the CTETRA(10) mesh was chosen as the best option to represent the teams' models. This mesh also worked better for the center hex of the models, where the SM and actuator assembly are mounted, which was kept solid so that the pins and fasteners could be attached appropriately.

Once the mesh was chosen, the next step was to add features to more accurately resemble the environment that the SMSS will be exposed to on the satellite. The first of these was modeling the extra hardware attached to the SMSS during operation. The shade assembly, actuator assembly, and secondary mirror were all modeled using CONM2 0D mesh elements as concentrated masses located at their center of mass, each with an extra 2/3 pounds to account for the 2 pounds of thermal electric hardware smeared across the structure, as shown in Table 4. Then, they were connected to their respective mounting holes using RBE3 1D Connections, which distribute the weight evenly without adding any stiffness to the structure (Appendix B, Fig. 6).

TABLE 4
FEM FEATURES AND LOCATIONS. NOTE: ORIGIN OF XYZ COORDINATE SYSTEM IS AT THE CENTER OF THE TOP PLANE OF THE MODEL

Model Setup			
Assembly	**Mass (lbm)**	**Location (X,Y,Z)**	**RBE3 Connections**
Shade	4.67	(0,0,4)	6
Actuator	6.67	(0,0,2)	8
Secondary Mirror	11.67	(0,0,-5.85)	12

The next step was to then model the boundary conditions of the teams' SMSS at each mount pad. A stiffness cone calculation was performed using Shigley's Mechanical Design as a resource to find the diameter of pressure, d^*, exerted by the specific fasteners that would be used in the mount pad [1].

$$d^* = d_H + 2\left(\frac{l}{2} + w_t\right)\tan(\alpha) \qquad (1)$$

Where d_h is the diameter of the head of the pin, 0.313 inches, l is the length of the pin, 0.2 inches, w_t is the thickness of the washer, 0 inches in this case, and α is the angle chosen for the cone, 30 degrees for metal pressed pins. A 0.1875-inch diameter pressed pin was used for this equation, which found a maximum diameter of 0.428 inches of stiffness. This pin was used because the other fastener on the mount pad, a #10-32 screw, had a 0.5-inch diameter stiffness cone, which meant the cones contacted each other and created inaccurate stress peaks in modeling simulations. Because of this, the pressed pin area was used to create circles with fixed constraints around each of the mounting holes as the boundary conditions for the model. This also created unnecessary stress peaking around the bolt, which interfered with the rest of the analysis. Instead, the team decided to fix the entire face of the mount pad as a fixed boundary condition. Although fixing the entire face added more stiffness, the stress peaking at these mount pads was reduced, and the motion of the SMSS was still accurately restricted.

Once the model environment was finalized, the next step was to model all the states required in the specifications. The first steps involved measurements of the total mass of the structure and using a bounded plane to calculate the obstruction area of the SMSS (Appendix B, Fig. 7). Then, a gravitational load of 18 times the Earth's gravity (18G) was applied axially along the negative Z-axis. 12G lateral loads were applied in the XY plane every 15° and were modeled as separate load cases, including the 18G load. The other load cases were two temperature loads, one from 20°C to 35°C and one from 20°C to 5°C. These loads were then combined into load cases including axial, lateral, and either the high or low temperature load to perform margin of safety analysis on the yield and ultimate stress of the model using Solution 101 Linear Statics in NASTRAN (Appendix B, Fig. 8,9). This was done finding the worst case loading for von Mises and Worst Principal stresses. These stresses were chosen because the industry standard for yielding is found from von Mises stress criterion due to the scientific evidence that ductile metals will not yield if their von Mises stress is below the material's yield stress [2]. Worst Principal was chosen for ultimate stress margins because of Mohr's circle which demonstrates that principal stress is the maximum stress a metal experiences in complex loading. Worst Principal stress is ideal for calculating the ultimate stress margin of safety. Stress analysis was also done for buckling by using Solution 105 Linear Buckling in Nastran, again using these load combinations from the margin of safety calculations (Appendix B, Fig. 10). Next, the temperature loads were used to measure the thermal deformation of the secondary mirror to see if the thermal deformation specification was met (Appendix B, Fig. 11). Finally, a modal vibration analysis was performed using Solution 103 Modal Analysis in NASTRAN. This analysis was done with no loads, only fixed constraints, to ensure the model's first mode was above 120 Hz while in use (Appendix B, Fig. 12).

During this analysis, simplifications were able to be made due to a fundamental understanding of stress states and material properties. More importantly, both the buckling and thermal deformation analysis were simplified because of how the Coefficient of Thermal Expansion (CTE) affects structures.

Buckling only occurs in members that are in compression, so during the search to find the worst-case subcase, a simplification was made to only use the high temperature load. The simplification was able to be implemented because of the constraints of the model and how the SMSS deforms with a change in temperature. When the temperature lowers, the metal shrinks, pulling the model into tension and reducing the potential for buckling. On the other hand, high temperatures cause the metal to expand, and with its fixed constraints at each end, the members are put in compression, making them much more susceptible to buckling. CTE is also a linear property, so when trying to find the average motion of the secondary mirror, only the high or low temperature load was needed, as the magnitude of the deformation is the same for both.

All this analysis provided great insight into the strengths of each of the designs. The circular models were much better at meeting the thermal and stress specifications because the thermal expansion or contraction of these models was a rotation about the Z-axis, as shown in Appendix B, Figure 11. This characteristic pushed the design towards geometries similar to concepts 3 and 5.

At this point in the design progression, it became clear that in order to meet the thermal specifications, the circular models were the most viable options. The initial analysis was done using Aluminum-6061 to make it consistent across all the models. As analysis continued, the team determined Aluminum was not going to meet specifications due to its low yield stress and issues with fatigue life. The temperature loads previously mentioned will be repeatedly experienced in orbit. Because of this, the thermal instability of Aluminum became an issue in terms of the lifetime of the part. This complication pushed a change to Invar-36 in the models due to its thermal stability and fatigue strength [3]. With Invar-36, the circular models were within the thermal specification. Consequently, Invar-36's high density led to a drastic increase in the weight of the models.

During the initial analyses, the shell thicknesses varied across each model. After discussion of the printing limitations of powder bed fusion with L3Harris, 0.1 inches was determined to be the minimum allowable thickness. Due to the weight continually being an obstacle, the minimum 0.1-inch shell thickness was determined to be the optimal value for the structure. While the shell helped with many characteristics of the model, including the weight, shelling posed challenges for manufacturing the model, which will be discussed in the manufacturing section.

The shelled model was successful in meeting a majority of the specifications. First, the stiffness of the hollow geometry made it resistant to buckling, so that requirement was met easily as seen in the worst buckling case in Appendix B, Figure 10. These hollow beams also assisted in boosting the frequency of the first mode of vibration due to the equation for natural frequency, as seen in Eqn. 2.

$$\omega_n = \sqrt{\frac{k}{m}} \tag{2}$$

The stiffness of the model, k, is determined by the overall geometry of the shape in reference to its boundary conditions. The mass of the body, m, is in the denominator of this equation so the hollow beams reduce mass, and in turn raise ω_n, the natural frequency.

The manufacturing constraints of the shelled model included steep overhang angles and bridges between walls without internal supports. Neither of those features are printable using blown powder printing, so the team ensured no supports were required with the NX maximum overhang angle tool (Appendix B, Fig. 13). The tool will display any surface that is over a certain degree overhang angle as red. This tool does not distinguish the print bed, so as seen in Appendix B Fig. 13, the bottom of the part is entirely red. This does not demonstrate manufacturing issues, as this surface will be printed directly onto the print bed as the base layer. L3Harris advised that a minimum 45-degree overhang angle or more from the horizontal would be printable for blown powder printing. This constraint pushed the design away from a simple constant cross section box beam. Instead, the side of the SMSS printed on top was turned into a vaulted roof with a 45-degree minimum draft angle off the horizontal axis (Appendix B Fig 14). This change added mass and decreased stiffness, but it was required for printability and verified using NX.

With Invar-36 as the material, the circular model still weighed almost 70 lbs., meaning that another material change had to be made in order to meet the weight requirement. This is when Titanium Ti-6Al-4V, as defined by the NX material library, was chosen. This is a popular titanium alloy within the aerospace industry, and it has many of the properties that were necessary for the design, such as thermal stability, high strengths, and relatively light density. This material fit the needs of the project and was the final choice that was pushed forward with for the final model.

One final check to ensure that Ti-6Al-4V was a valid material choice was a fatigue life study based on the thermal loads. The max stress the model will experience in its worst-case condition is 26,200 psi. This maximum stress is well within the fatigue strength of this material, which is approximately 60,000 psi, so the fatigue limit is not crossed (Appendix B, Fig. 15) [4]. This guarantees that the lifetime of the part will not be limited by fatigue strength.

Once the final material decision was made, optimization began on the design to push its performance to the maximum. This optimization, as discussed in the next section, brought the team to a final design that then required a convergence study to ensure the FEA results were accurate. In order to converge the model, the mesh size was iteratively reduced, starting at 0.5 inches. The stress analysis was then performed to find the maximum yield stress value. The goal of this study was to find the mesh size where the max von Mises stress converges and stops varying from iteration to iteration.

Initially the plan was to make the entire mesh iteratively smaller until it converged, but that was unsuccessful, as the stress continued to rise until the mesh was so small the computers on campus could not solve the model due to memory allocation errors. After these issues arose, mesh controls were used to try and manipulate the element size around the peak stress areas. To do this, first the mesh was reduced on the faces around the peak stress areas – the valleys along the blend on the angled extrusion of the model. This was unsuccessful as well, so other strategies were used such as manipulating the size on the edges of the blend and using biasing to gradually change the element size as the peak area was approached. Again and again this failed, so as a final attempt the team used point mesh controls to make a 0.05-inch mesh around the peak stress area on the exterior and interior of the shell. These points have 0.05-inch elements at their center and then gradually adjust to the larger mesh size over their radius of influence, for these 1.5 inches was chosen. This result did not converge as was outlined by L3Harris, two consecutive iterations within 1% of each other, but it gave us enough information to use for the final results (Appendix B, Fig. 16).

The oscillation seen in this study was consistent for all the studies performed and made the team confident about the results that were seen. Iteration 3 was chosen because of its relative location in the middle of the oscillation and for ease of analysis due to its mesh size. The team is confident in using this as a convergence study because every other result was consistent between iterations, and only maximum stress varied. Normally, maximum stress variation may pose concerns, however, the maximum von Mises stress was 26,200 psi out of all the SMSS studies. With this stress value, the margin of safety was 1.22 using an allowable stress of 58,377 psi, derived from a factor of safety of 2 for yield stress. Therefore, there is a considerable margin for the stresses. The convergence study provided sufficient information instilling confidence that the model's maximum stress would not exceed the allowable yield stress. With this convergence study performed, the final analysis could be done to ensure the model met all the specifications.

A fastener torque calculation was performed on the SMSS connection to the FMS to determine the torque required to connect the assembly safely. The bolt used for the calculation is a grade 8 #10-32 with a non-plated black finish bolt condition. The tensile stress area, A_t, for a #10-32 bolt is 0.0200 in^2 and the nominal diameter, d, is 0.19 inches [5]. The proof strength, S_P, for a Society of Automotive Engineers (SAE) grade 8 bolt is 120,000 psi [6]. Using Equation 3,

$$F_P = A_t \cdot S_P \tag{3}$$

F_P, the force on the bolt under proof stress, is 2,400 lbf. Given that it is a permanent connection, Equation 4 is used to find the preload, F_i.

$$F_i = 0.90 \cdot F_P \tag{4}$$

Equation 4 calculates a required preload of 2,160 lb. Equation 5 calculates the required torque, T [7].

$$\mathrm{T} = \mathrm{K} \cdot \mathrm{d} \cdot F_i \tag{5}$$

K is the bolt condition, d is the bolt diameter, and F_i is the preload. Under these circumstances, the bolt condition is equal to 0.3. This equation finds the torque required for one of the permanent fasteners that connects the secondary mirror to the SMSS. The torque required is 123.12 lbf-in.

One tolerance issue that was encountered during the design was the tolerance of the hole diameters for the mount pads and assembly mounting locations. This tolerance issue arose from the inaccuracy of additive manufacturing in terms of hole diameter. Testing was performed by printing Polylactic Acid (PLA) cubes with 4 different diameter holes, ranging from 0.045 inches to 0.06 inches varying by 0.005 inches for each (Appendix B, Fig. 17). Three of these cubes were printed, and then a 0.04-inch diameter pin was pressed into each hole to see which hole fit the best for a pressed pin type connection. The issue was that each of the three cubes posed different results. For one, the 0.055-inch hole was best, another was the 0.06-inch hole, and for the third none of the holes fit well. This proved the inaccuracy of these holes when they are printed. Given the lack of accuracy in printing and advisement from L3Harris, the team decided that all mounting holes would be post processed in order to ensure the assemblies can mount accurately and safely.

MODEL OPTIMIZATION

Even with the adjustments outlined, the model was far from complete and required optimization to meet the requirements and specifications. The two methods of optimization employed were topology and shape optimization. To obtain a greater understanding of the structural behavior of the FEM, topology optimization was performed on a larger design space. By solving the solution for a larger, solid design space, the results highlighted the critical load path through the SMSS in red while also highlighting regions in the design where elements contained little to no stress in blue (Appendix B, Fig. 18). This approach not only helped refine the overall geometry of the SMSS but also provided valuable insights into areas of stress concentration, aiding in subsequent design adjustments. With this information, it became apparent which design features within the model were most important for maximizing stiffness and where unimportant elements of excess mass existed in the model, such as the cross sections of the legs where they interface to the center of the SMSS. Having gained a more refined understanding of the SMSS loading response through topology optimization, the team proceeded to further refine the design through shape and sizing adjustments.

With the knowledge that the optimization solutions available had multiple ways to approach set up and execution of the optimization, concept 1, a triangular design, was used first to better understand the most effective approach to shape optimization. The first set up utilized the design objective of minimizing the maximum von Mises stress within the SMSS across all potential launch load cases. The design constraint was set to be the upper limit of the weight for the SMSS at 18 lbf. Lastly, the design variable that would be optimized was the length of the legs spanning from the mount pad to the interface where the leg began to curve. The design variable was set at 9.5 inches and was given a lower limit of 0.1 inches, and an upper limit of 11 inches. The lower limit was set to allow for the optimizing tool to shorten the leg as much as necessary to reduce the von Mises stress, although it was not anticipated to reach the limit due to an increased weight. The upper limit was set to prevent the remaining geometry from conflicting with one another. After the shape optimization parameters were set, the optimization was run with the initial leg length of 9.5 inches, the SMSS at a maximum von Mises stress of 15,740 psi, and a SMSS weight of 20.806 lbf. Since the objective was to minimize von Mises stress, each optimization iteration took several minutes to complete. The maximum von Mises stress was to be identified across all possible launch load cases with the highest identified stress being the value recorded. The initial shape optimization required fourteen iterations which ran for a total of approximately 1 hour and 15 minutes. The resulting leg length was 10.805 inches, with the SMSS at a maximum von Mises stress of 20,765 psi and a weight of 18.003 lbf (Appendix B, Fig. 19). With the stress-based approach, the weight constraint proved to be the driving force since the model had yet to achieve a weight below 18 lbf, which therefore did not allow the maximum von Mises stress to be reduced. After learning how long the shape optimization approach lasted with the minimizing stress objective, the team explored another approach.

The next approach was to use a design objective of minimizing the weight of the SMSS. The design constraint was set to be the lower limit of the first mode of frequency at 120 Hz. The same design variable of the leg length was used to understand how the two different approaches compared. The design variable was set at 9.5 inches and was given the same lower and upper limits. The initial weight of the SMSS was 20.806 lbf and the initial first mode of vibration was 154.29 Hz. Shape optimization was run and lasted approximately 5 minutes with a total of three iterations. The resulting leg length was 10.999 inches, with a total SMSS weight of 16.827 lbf and a first mode of vibration at 134.79 Hz (Appendix B, Fig. 20). The minimizing weight approach trended towards the upper limit of the design variable similar to the minimizing stress approach. Additionally, the weight of the SMSS was reduced below 18 lbf with the minimizing weight approach, which could not be achieved with the other approach. Lastly, the minimizing weight approach reduced optimization time significantly. These three conclusions led to the team utilizing the above shape optimization approach for any geometry related optimization needed throughout the remainder of the optimization process.

These shape optimization findings were then applied to an updated Ti-6Al-4V circular design. The unoptimized model had a 0.1-inch-thick shell, weighed 21.789 lbf, had a first mode of vibration of 130.42 Hz, contained a positive margin of safety in yield for the worst-case launch load environment, and satisfied the SM translation specification but not the SM rotation specification (Appendix B, Fig. 21-25). The first two optimization setups used the design objective of minimizing weight and a design constraint of the lower limit of the first mode at 120 Hz. Each setup only optimized one design variable at a time and the second setup used the optimized model from the first setup. The first setup design variable was the inner radius of curvature for each leg and the second setup design variable was the leg length on the outer side of each leg from the mount pad to the curved section of the leg. Both design variables are noted in Appendix B, Figure 20. After both shape optimizations were run, the SMSS weight was reduced to 19.455 lbf and the first mode reached 126.32 Hz (Appendix B, Fig. 26 & 27). The SMSS maintained a positive margin of safety in yield for the worst-case launch load environment and satisfied both the SM translation and rotation specifications under a 1°C isothermal load (Appendix B, Fig. 28-31).

Several other shape optimization solutions with the same design objective and design constraint were applied as the circular concept continued to advance. One of the final findings from shape optimization was how to dimension the opening of the SMSS for the SM to mount within, avoiding violation of the keep out zone specified by L3Harris. At the time of the optimization process the team had moved away from the hexagonal opening and began exploring a circular opening with a metal 3D printable model. The opening had a diameter of 11 inches and was set to be optimized within a range of 10.8 inches and 12 inches. Once the shape optimization was run, the circular opening was driven to the lower limit of 10.8 inches (Appendix B, Fig. 32). The result indicated a smaller sized opening benefited both the stiffness and weight of the structure. When comparing the circular opening to the hexagonal opening, the circular first mode was lower. The team eventually returned to a hexagonal opening to increase the structure's stiffness; however, the optimized finding was still applied, and the hexagon flat-to-flat distance was changed to 9.35 inches.

MANUFACTURING

For this project the goal was to design a SMSS that could be made using additive manufacturing. Specifically, the team focused on using blown powder Directed Energy Deposition (DED). While DED is more accurate and faster than plastic Fused Deposition Modeling (FDM) printing, it introduces more challenges in the realm of overhang angles and printability. When designing the final model, much consideration was put into making the overhang angle, or floating slope, more than 45 degrees from the horizontal to ensure that it could be printed using DED.

Metal 3D printing, having only recently been adopted for the aerospace industry, has many unknowns with regards to tolerances and strengths. As a result, the team felt it important to order metal 3D printed coupons to run material and quality tests.

Many vendors offered metal 3D printing services, but for most, their prices were unreasonable given the project's budget. For this reason, the company CraftCloud was chosen. Twenty-four samples were ordered in total with half being printed out of 316L Stainless Steel and the other half out of an aluminum alloy (AlSi10Mg). For each material the team requested that six be printed horizontally and the other six printed vertically to try and determine if there would be a substantial difference between the print directions due to anisotropic material properties (Appendix C, Fig. 1, 2). When the coupons arrived, there was no indication of which orientation they had been printed and when compared using results from 3-point bend tests, tensile gripper tests, and Rockwell hardness tests there was no determinable difference in their mechanical properties. After viewing the samples under a binocular microscope, and then after polishing and etching under the same microscope, there was no success in finding out if the samples had been printed in different orientations. Additionally, the flatness of each sample had high variability due to warping of the parts. Dimensions of the parts were quite consistent, along with weight, but this warping did affect the overall strength of the dog bones.

L3Harris is currently exploring using a proprietary blend of Invar for their production run SMSS. Invar is chosen for its low CTE making it ideal for holding optics that are sensitive to movement. A full scale SMSS made using metal would be greatly outside the budget given for the project. Additionally, the properties for the specific Invar being used were unknown. Instead, Ti-6AL-4V, a popular material choice for the aerospace industry due to its desired material properties, was chosen as a substitute to design around. While less expensive than Invar, a model printed using Ti-6AL-4V would still be well outside the budget for this project, making the acquisition of a full-scale metal model unfeasible. Even though ordering a metal model was not possible, the team still needed a physical model to correlate the FEM. It was then decided that a model made from plastic using FDM fabrication would be used.

With the cost of the coupons already using half of the budget, time was put into trying to manufacture a model using campus printers. All the team's designs were shelled or hollow on the inside which is a challenge for 3D printing. 3D printers, both FDM and DED, build in layers and need material under each layer to build off. For this reason, printers struggle with printing sharp overhang angles and the team went through many design iterations to make a shelled model suitable for printing.

A 20% scale model of concept 5 was printed out of Acrylonitrile Butadiene Styrene (ABS) on a Stratasys F270 printer to test how the I-beam design would print and if a model of that size could be used for testing correlation (Appendix C, Figure 3). The model was printed solid because the printer was not able to print overhangs and the slicer defaulted to a solid model. The flanges of the I-beams required dissolvable supports printed underneath which were later dissolved in sodium hydroxide. The model was successfully printed, but after communication with Professor Muir, it was decided that a model of that size would not be sufficient for testing. It was determined that a 50% scale model or higher would be desirable.

The next model printed was concept 3 in ABS at a 5% scale on the Stratasys F270 (Appendix C, Figure 4). This was done to explore if a model could be printed in halves and then glued together. While the model printed and fit together well, this was likely because of the small scale. After discussion with L3Harris, it was decided that this would not be a viable option for a full-scale model as it would induce errors with alignment, structural integrity, and post-processing. Additionally, this manufacturing method was deemed inefficient as it would require a substantial amount of time and deviates from the original intent of the project.

The next concept explored was printing a model in sections and gluing the sections together. This model was intended solely to test printing capabilities in house. Concept 3 was split up into 8 sections in NX and then sliced in PrusaSlicer at a 55% scale (Appendix C, Figure 5). The pieces were printed on Prusa i3 MK3S printers using Polymaker Polylactic Acid Plus (PLA+) for the filament. The sections were then glued together using J-B Weld to get a complete model. This was done using C clamps to ensure the seal was strong and had good surface area over the entire section that was being glued. Despite being an appropriate size for testing, the model lacked reliability and would have likely caused discrepancies with the FEM results. The printers used did not have covers causing inconsistent warping and misalignment, indicating the need for the model to be printed in one piece.

When investigating ways to print a model as a single print, it was discovered that adding an edge blend to the inside of the shell could make models printable for FDM. Figure 6 in Appendix C was printed on a Stratasys F270 in ABS as a proof of concept that a shelled model was printable. Figures 6 and 7 in Appendix C show the slice of a model using this edge blend and then the top part of the model showing the edge blends. This model was a 10% scale, printed on Prusa i3 MK3S printer out of Polymaker PLA+, and was the first model to be successfully printed shelled in a single piece.

To manufacture a model for testing and correlation, research was done into third party vendors that could print a plastic model using FDM fabrication. While some vendors had the capabilities to print a full-scale plastic model, price and lead time were bigger factors and ultimately Xometry was chosen to print a 60% scaled model out of Acrylonitrile Styrene Acrylate (ASA) (Appendix C, Fig. 8 and 9). Xometry was used to manufacture the previous year's model, was reliable in the past, and had the best mix of price to lead time of the vendors considered. The final cost of the model was $684.43 and was ordered on Friday, March 29th and arrived Tuesday, April 9th for a lead time of 12 days. This model used a similar design concept to the previous for a shelled model using edges to overcome steep overhang angles. This model was able to use a small radius for the blends to keep the weight down but had large bridge lengths, or sections that gap between supports. While this was able to be printed using FDM and was verified in Prusa Slicer, it was later discovered to be unsuitable for DED printing.

After talking with L3Harris, it was discovered that for DED printing the overhang angles had to be at least 45-degrees from the horizontal axis and could not have bridge lengths. This rendered the previous model unsuitable as a final design and led to further exploration of printable modeling.

Through further design iterations and experimentation, the team designed a shelled model that met all the specifications given and was fully printable using DED printing. The model has a 38-degree draft extrusion on the bottom face of the SMSS to meet the 45-degree overhang angle requirement for DED printing. Additionally, the model doesn't have any bridge lengths and has a minimum wall thickness of 0.1 inches to meet the recommended thickness for DED printing.

After adjustments to the design to ensure printability in DED, a final model was achieved and sent to RPM Innovations Inc. for an estimated quote of the price of a full-scale metal Ti-6Al-4V model. This price came out to be $72,496. This cost is an estimation as not all the manufacturing details were established due to a time constraint and lack of budget. Additionally, this cost does not include post processing procedures which would increase the cost further. Along with this, a final drawing package was created for our final design (Appendix C, Fig. 10-18).

The total cost of the parts ordered for this project, the coupons and 60% scaled model, are shown below in Table 5 totaling $1207.27. The total cost for the team $97,075 show in table 6, represents the time taken to design the model, iterate designs, and to conduct testing. This amount added with the parts ordered comes out to $98,282.27 and is the total cost for the project.

If the SMSS production were to increase to one thousand systems, improvements would need to be made to reduce the amount of material used. While the final model met all the requirements, specifications, and was printable, the team believes that additional material could be removed with further optimization. Consequently, additive manufacturing costs and printing time would be reduced.

TABLE 5
PROJECT BUDGET USAGE

Items	Cost
24 Metal 3D Printed Coupons	$522.84
60% Scaled Model	$684.43
Total Cost	$1,207.27

TABLE 6
TEAM COST BREAKDOWN

Team Member	Hours	Cost
Alex Nagy	221.75	$22175
Calvin Tourangeau	215.5	$21550
Declan Bhagwat	199.5	$19950
Noah Schloff	182	$18200
Shelinee Hernandez Espino	152	$15200
Team Total	970.75	$97,075

TEST PLAN AND RESULTS

Coupon Testing Plan & Results

The 3D printed metal coupons of Aluminum (AlSi10Mg) and 316L Stainless Steel were measured to understand the variability of metal 3D printing and tested to gather information on the material properties. First, the coupons were observed under a microscope to determine print direction because the vendor did not specify the coupons' print directions. Each coupon was grouped as they were received in shipping and analyzed under the microscope (Appendix C, Fig. 19-24). Unfortunately, the print direction could not be determined with the microscope inspection and only lines due to the sandblasting finish could be seen. Next, the gage width and gage thickness of the coupon at the midpoint of the gage length was measured using a micrometer (Appendix C, Fig. 25 & 26). As designed, the coupon had a nominal gage width of 0.5 inches and a nominal gage thickness of 0.125 inches. After recording these measurements, the cross-sectional area, A, of each coupon was calculated using Eqn. 6,

$$A = wt \tag{6}$$

where w is the gage width of the coupon and t is the gage thickness of the coupon. The flatness of each coupon from peak to valley was then measured using a depth gauge while sliding the coupon across a granite surface plate (Appendix C, Fig. 27). To ensure accurate flatness measurements, the coupons were laid flat on both sides. One orientation would cause the coupon to rock back and forth while the other orientation would have two clear contact areas at each end of the coupon shoulder. The contact areas prevented any instability and rocking. The coupon was placed on the two sloid contact points so the arch height could be measured without rocking inaccuracies. Next, the mass was measured using a digital scale and the volume was measured using water displacement in a graduated cylinder for each coupon. Using the mass, m, and volume, V, of each coupon, the density, ρ, was calculated using Eqn. 7.

$$\rho = \frac{m}{V} \tag{7}$$

The measurements of the 3D printed metal coupons and the density values can be seen in Appendix C, Tables 1 and 2.

After all measurements were taken, the coupons were thermally cycled from 20°C to 45°C for eight total cycles. The coupons were placed in the VWR oven at 45°C for 15 minutes and then transferred to the lab room temperature to remain at 20°C for 15 minutes (Appendix C, Fig. 28) [8]. This thermal cycle was performed to mimic the space conditions the structure will be placed in, based on the thermal loads providing in the specifications and requirements. It also ensured consistent moisture for all of the samples.

Immediately after the thermal cycle procedure, the Rockwell hardness number was calculated by averaging the five hardness measurements taken on an Instron Wilson 2000 Digital Rockwell Hardness tester. These measurements were taken at the shoulder of the coupons with a Scale B 1/16-inch steel ball indenter and an applied force of 100 kg, as according to ASTM E18 - 11 specifications. (Appendix C, Fig. 29 & 30). The average hardness of the 3D printed aluminum coupons was 69.310, with a standard deviation of 0.839 and a coefficient of variation of 1.21% (Appendix C, Table 3). The average hardness of the 3D printed steel coupons was 95.088, with a standard deviation of 2.430 and a coefficient of variation of 2.56% (Appendix C, Table 4).

The next test was a 3-point bend test, completed on an MTS Alliance RT/50 (Appendix C, Fig. 31). The values chosen for this test were based off Chris Pratt's guidance and ASTM specification E290 – 09. Each coupon was placed on the supports set at a 1.75-inch spacing. An extension rate of 0.05 in/min was applied and each aluminum coupon was loaded until the MTS machine applied 80 lbf while each steel coupon was loaded until the MTS machine applied 70 lbf. These final load values allowed for enough data points to be recorded, once the data acquisition rate was doubled. The flexural modulus could then be calculated, as seen in Equation 8, and the coupons were a factor of safety of about 1.5 below the yield stress.

$$E_{Flex} = \frac{L^3 F}{4wt^3 d} \tag{8}$$

In this equation, L is the spacing of the supports, 1.75 inches, F is the force applied, w is the width of the sample, t is the thickness, and d is the vertical displacement. During the first 3-point bend test, a steel coupon was taken past yield so it could not be used in the following test and was not included in the 3-point bend or tensile test data and calculations. The average flexural modulus of the aluminum coupons was 2.746E+6 psi, with a standard deviation of 2.232E+5 psi and a coefficient of variation of 8.13% (Table 7). The average flexural modulus of the steel coupons was 4.616E+6 psi, with a standard deviation of 4.616E+6 and a coefficient of variation of 10.42% (Table 8).

After the 3-point bend test, the coupons were tested on the MTS Alliance RT/50 in a tensile test (Appendix C, Fig. 32). This test was designed off of ASTM E8/E8M – 11 specifications. The coupons were secured into the tensile grippers and an extensometer was attached to the coupon with a 2-inch gage length. An extension rate of 0.1 in/min was applied and the extensometer was removed from the coupon once a displacement of 0.02 inches was measured. The loading continued until each coupon fractured. Once the tensile test data was collected, the yield strength, ultimate strength, and Young's modulus of each coupon was calculated. The overview of these material properties for the aluminum and steel 3D printed coupons are shown in Table 8 and 9 below. The vendor reported a range for the Young's modulus and ultimate stress for both materials, so the measured values were compared to those reported values. For the aluminum coupons, the average Young's modulus of the twelve samples was less than the minimum reported value by about 6.79%, however, the average ultimate stress was within the reported range. The average Young's modulus of the eleven steel samples was less than the minimum reported value by about 4.47%, however, the average ultimate stress was within the reported range. The complete data set for the aluminum and steel coupons from the 3-point bend and tensile tests can be seen in Appendix C, Tables 5 and 6. In addition, the plots for bending stress versus bending strain and applied load versus deflection from the 3-point bend test can be seen in Appendix C, Figures 33 and 34. Lastly, the plots for stress versus strain and applied load versus data iteration from the tensile test can be seen in Appendix C, Figures 35 and 36.

TABLE 7
TENSILE AND 3-POINT BENDING TEST STATISTICS FOR THE MEASURED VALUES OF THE ALUMINUM 3D PRINTED COUPONS

3D Printed Aluminum Coupons (AlSi10Mg)				
	E (psi)	σ_{yield} (psi)	σ_{ult} (psi)	E_{flex} (psi)
Average	9.461E+6	3.764E+4	5.534E+4	2.746E+6
Standard Deviation	7.581E+5	7.087E+2	9.889E+2	2.232E+5
Coefficient of Variation	0.0801	0.0188	0.0179	0.0813
Minimum	8.066E+6	3.660E+4	5.375E+4	2.516E+6
Maximum	1.014E+7	3.894E+4	5.569E+4	3.105E+6
Expected Minimum	1.015E+7	-	4.815E+4	-
Expected Maximum	1.102E+7	-	6.962E+4	-

TABLE 8
TENSILE AND 3-POINT BENDING TEST STATISTICS FOR THE MEASURED VALUES OF THE STEEL 3D PRINTED COUPONS

3D Printed Steel Coupons (316L Stainless Steel)				
	E (psi)	σ_{yield} (psi)	σ_{ult} (psi)	E_{flex} (psi)
Average	2.542E+7	7.523E+4	9.401E+4	4.616E+6
Standard Deviation	1.472E+6	2.964+3	3.111E+3	4.812E+5
Coefficient of Variation	0.0579	0.0394	0.0331	0.1042
Minimum	2.365E+7	6.814E+4	8.688E+4	3.867E+6
Maximum	2.848E+7	7.921E+4	9.861E+4	5.415E+6
Expected Minimum	2.661E+7	-	8.557E+4	-
Expected Maximum	2.683E+7	-	1.015E+5	-

The next test conducted was the polishing and etching of a steel and aluminum coupon to try and determine the print direction of the coupons. The coupons were cut with a hacksaw and positioned in a vertical and flat horizontal orientation. They were then pressed into a solid die mold using the Bakelite Press (Appendix C, Fig. 37). This allowed for the samples to be polished and etched without contaminating the samples. The polishing was done in two parts, the samples were first polished using increasingly fine grits of sandpaper, which was done to remove scratches from sawing. After the sandpaper the samples were polished further using polishing wheels and first a 1.0-micron alumina slurry and then a 0.05-micron alumina slurry. After the polishing was concluded the steel sample was etched using Kalling's Reagent for a few seconds and then examined under a VHX UHX-900F digital microscope (Appendix C Figs. 38-41). There was nothing of note observed from the first etching, so it was recommended that the sample be etched further. This was done a few more times, etching the sample further and looking at it under the microscope, and no additional information was found from this. Because of the lack of results from the steel sample the aluminum sample was not etched or examined under the microscope. The intent of polishing and etching the coupons was to potentially determine the print direction of the coupons. Unfortunately, the polishing and etching could not help in determining the print direction of the coupons.

Finally, X-Ray Crystallography (XRD) was completed on an aluminum and steel sample to better understand the composition of each 3D-printed coupon. The XRD was done on a Rigaku XtaLAB Synergy-S diffraction system and two samples were examined, one for each material the coupons were printed in. For each coupon used, some flakes were scraped off using a pocketknife and one flake was placed on a sample holder to be loaded into the XRD machine. For the aluminum sample copper radiation was used and for the steel sample copper radiation was first used and then molybdenum radiation was used as the copper did not give a clear plot due to inconclusive intensity peaks (Appendix C, Fig. 42-44). From the molybdenum tests intensity plots for the rotation of the samples were generated and showed peaks where high amounts of certain elements were found. Using HighScore, a program for XRD analysis, the peaks from the aluminum sample was analyzed and compared to a material library to find matching materials (Appendix C, Figs. 45). From the analysis three primary compounds were found in the sample. The first, aluminum with a score of 98, the score being the software's certainty that a compound is present in the sample and measured on a scale of 0 to 100, was to be expected as the sample should be a majority aluminum. The next highest score was Aluminum Iron also with a score of 98. This was unexpected as while Iron is sometimes used in AlSi10Mg the amounts used are mostly in the realm of 0.55 weight percent [9]. This inconsistency was explained when it was found out that the pocketknife used to scrape the samples was made of steel, so it was concluded the contamination was a result of that. The final compound found was aluminum silicon with a score of 82. This again was expected to be found albeit with a higher score considering how silicon usually makes up around 9 to 11 weight percent of the alloy [9]. Magnesium was not detected in the sample, which was unexpected but after discussion the team believes that this is a result of the element only being 0.25 to 0.45 weight percent of the alloy on average [9]. Another reason for the magnesium's absence was because of the strong presence of other elements. While the XRD was primarily done to try and find the element composition of the samples, the software used did not have the capability to do so and unfortunately it was not completed for this project. For the 316L steel sample, the program was unable to be switched to analyze samples that used molybdenum radiation, so the analysis was unable to be completed as well. Through the XRD testing results, no meaningful data was obtained.

Model Testing Plan & Results

To check the validity of the simulation results obtained after optimization, the team outsourced a 60% scaled ASA version of the prototype model (Appendix C, Fig 8 and 9) through Xometry. Initially, the ASA model was placed on a digital Adam scale to measure its overall weight, resulting in a total weight of 1.08 lbm. The first test performed was the modal strike test. As shown in Appendix C, Figure 46, the model was placed on a flat Newport table, and mounted on top of a foam cushion to decrease the stiffness being added to the model from the contact to surrounding materials. Triaxial accelerometers were then attached to the top of each mounting pad and to the inner circle of the structure using wax and secured using tape for strain relief (Appendix C, Figure 46). If the model were placed on a flat table directly, the model's vibration data results would be less clear since the response would include both the response from the table's stiffness and the model due to their direct contact. The cushion was supposed to avoid this damping but failed to do so. Instead, this test was treated as a practice run to get familiar with the procedures.

The setup of the test was changed though, as the model was hung from bungee supports (Appendix C, Fig. 47). The bungees were attached at locations where the model's modal frequency analysis indicated deflection would be at a minimum. These locations would minimize damping during testing. Then, the four accelerometers were attached to the model as they had been attached previously. The hammer used for the test incorporated a force sensor at its tip and its mass was known. It's important to note that each accelerometer was placed at locations where greater vertical (-Z direction) displacement was predicted to happen based on mechanical analysis of the model.

Professors Muir and Gracewski helped the team with the setup of Simcenter Testlab, the software needed to collect data through the LMS data acquisition instrument that the hammer and accelerometers were connected to. Twelve channels were used to obtain data, one channel set up for the hammer to record data in the negative Z direction, one for the accelerometer located at the center to record data in the positive Y and Z directions, and the remaining channels were set to record the motion at each leg in the X, Y, and Z directions.

The hammer force, frequency range of interest, voltage sensitivities, and bandwidth were set before recording data samples. Each of these channels recorded the voltage obtained from the accelerometers after each hammer strike. Once the software was ready to collect data, the model was struck five times at similar points located along the hexagonal edge across from the inner accelerometer while simultaneously recording the frequency response of the structure (Appendix C, Fig. 48). The software related the frequency response of the accelerometers with respect to the frequency response of the hammer by creating a transfer function that incorporated the ratio of the Fast Fourier Transform (FFT) of the accelerometers to the FFT of the hammer. Through this transfer function, the peaks of each frequency were obtained (Appendix C, Fig. 49). These were the stable frequencies which indicated the modal deformation and corresponding mode shape. The first stable result was identified as 105.276 Hz as seen in Appendix C, Figure 49.

To have a better representation of the model's mode shape, Professor Muir assisted the team in the creation of an ideas universal model in NX with the purpose of uploading this file to the Simcenter Testlab software. In this model simulation, a 2D mesh was employed and specific nodes were created to represent the approximate location of the accelerometers on the physical model. Once the file was uploaded to the software, each of these nodes were matched with their respective accelerometer data (Appendix C, Fig. 50). The accelerometer data was mapped to the universal model geometry and an animation of the measured piston mode shape was created with the universal model overlaid (Appendix C, Fig. 51).

To further validate the FEM, a displacement test was performed by placing the model on a flat table to avoid vertical or horizontal motion. The model was mounted on three cylinders to simulate zero stiffness roller constraints (Appendix C, Fig. 52). Using the flat table as a reference, the FARO Quantum Max ScanArm was used to take three reference points by touching the table in three different locations around the model. From these points an initial plane was created, which was used as a reference for future measurements.

To perform the displacement test, the team used two 1-2-3 blocks along with some laboratory weights to place a total mass of 2,122.5 grams at the center of the structure and marked the points whose location would be measured with respect to the reference plane (Appendix C, Fig 52). Using the Faro Arm, the team took the location of each of the three points before and after placing the weight on the model. This digital method again had very high percent difference, presumably due to inaccuracies in measurement using the Faro Arm. To avoid this, the team performed the test again using an analog measurement method.

Next, a displacement test was set up once more. The model leg ends were placed on 1-2-3 blocks and two weights one with a total of 2076.9 grams and the other 1,357.3 grams for a total mass of 3,434.2 were placed at the center of the structure, distributed on the two beams with the actuator assembly mount holes (Appendix C, Fig. 53). A depth dial gage was set up at a point on the side of the rectangular cut out without any mount holes to measure the displacement of the model as the mass was removed. From the first measurement location, the total displacement was 0.031 inches for the lighter weight and 0.0515 inches for the total weight. Next, a second measurement was taken from a point centered between the mount holes for the SM and the shade assembly (Appendix C, Fig. 54). The total displacement from the second location was 0.0305 inches for the lighter weight and 0.051 inches for the total weight.

Once the displacement and vibration test data were obtained from the physical model, the team created a model in NX to be used for correlation. A FEM file was made and the model was meshed using CTETRA(10) elements at a 0.25 inch element size. A custom material was created in the NX materials library to simulate the material properties of ASA with an approximate of 0.3 Poisson's ratio, a Young's modulus of 245 ksi, and a density of 0.0392 lbm/in^3. A simulation file was then created with two solutions to represent the tests conducted. The first, Solution 101 Linear Statics was made to correlate the displacement test results. Two subcases were created for the solution to model the different weights put on during testing, one with a mass of 2076.9 grams and the other with a mass of 3434.2 grams. They both were created as a distributed force along the actuator mounting supports located inside the center hexagon of the model representing the area of the bottom weight. The legs were fixed in 3-2-1 constraint approach on the bottom polygon edge of the mounting pads. The other solution, Solution 103 Real Eigenvalues, was used to correlate the vibration test results. All legs were unconstrained, and no additional loads were applied for this solution.

Both measurement locations were inspected in the displacement plot on NX with resulting displacements in inches (Appendix C, Fig. 55-58). The modulus for the FEM was adjusted from the values given in the Stratasys specification sheet to better match the displacements measured. This was acceptable because the testing was reliable and FEM model was a sufficient representation that the values should match. It is likely that the modulus given in the specification sheet is an average of many tests and because the material is anisotropic, it may not match for every test done. As shown in Table 9, the analog based approach for the displacement test with 1-2-3-inch block supports differed from the simulated results by 0.257% and 0.845% for the 2076.9-gram weight for locations 1 and 2 respectfully and by 0.292% and 0.137% for the 3434.2-gram weight for the same respective locations.

The FEM in NX was solved once more with Solution 103 and the Young's modulus was adjusted again for correlation to get the lowest percent errors for the displacement and modal testing. From the NX modal solution, the first nonzero piston mode had a natural frequency of 114.21 Hz (Appendix C, Fig. 59). While comparing the modal strike test with the hanging set up and the FEM, the resulting percent error was 7.822%.

TABLE 9
CORRELATION RESULTS FROM TESTING AND SIMULATION

	Testing	**FEM**	**% Difference**
2076.9g Weight Location 1	0.031 in	0.03106 in	0.257
2076.9g Weight location 2	0.0305 in	0.03072 in	0.845
3434.2g Weight Location 1	0.0515 in	0.05165 in	0.292
3434.2g Weight Location 1	0.051 in	0.05093 in	0.137
Mode	105.276 Hz	114.21 Hz	7.822

The Faro Arm then helped to create a point cloud scan of the entire outer layers of the structure, and this data was then uploaded to NX to measure the angle between each of the legs to ensure a symmetry of 120 degrees (Appendix C, Fig. 60). From this testing the team found that the leg with the most deviation had an angle of 118.07 degrees. When scanned using the Faro arm, so many points were created that to get the model to load in NX only 2.24% of the points were loaded, representing an incomplete version of the geometry.

Final Model Results

After implementing all successful optimization techniques concurrently, a final titanium model was developed that met all the outlined requirements and specifications from L3Harris. A circular sketch with a diameter of 48 inches was included to verify the model satisfied the outer diameter specification (Appendix C, Fig. 61). The point cloud scan taken using the faro arm was used to verify that the interface locations were 120 degrees apart (Appendix C, Fig. 60). Then, the mass of the model was measured to be 17.7071 lbm which is less than 18 lbm and therefore satisfies the mass specification (Appendix C, Fig. 62). Next, a bounded plane was created to verify the obstruction area of the SMSS projected onto the PM and was measured to be 206.22 in^2 which is 13.993% of the PM area which satisfies the obstruction area specification (Appendix C, Fig. 63). Solution 103 Real Eigenvalues was solved, resulting in a first mode natural frequency of 123.38 Hz which is greater than 120 Hz and satisfies the modal specification (Appendix C, Fig. 64). Next, Solution 101 Linear Statics was solved and resulted in a worst-case margin of safety of 1.5383 for yield and 0.9384 for ultimate, which satisfies the specification for positive margins of safety for yield and ultimate stress (Appendix C, Figs. 65 and 66). After these NASTRAN solutions were executed, the temperature subcase within Solution 101 was inspected for verification of the secondary mirror thermal translation specification. The temperature subcase contained only a temperature load of a 15°C, so the simulated displacement of the SM was divided by 15 to determine the 1°C isothermal load. The team was able to divide the simulated displacement since Ti-6Al-4V is linearly affected by temperature changes. After inspection, the SM translated 0.27 micro-inches and rotated 0.031 micro-radians under the 1°C isothermal load (Appendix C, Fig. 67). Therefore, all specifications were verified and satisfied. The requirement that the structure be printable with additive manufacturing was also verified using NX's maximum overhang angle tool and was satisfied by the design (Appendix C, Fig. 68). The margin of safety requirement was verified when the factors of safety were applied to the yield and ultimate failure. Additionally, Solution 105 Linear Buckling was solved so the buckling factor of safety could be verified for the design. The lowest buckling eigenvalue was 90.19, which meant the buckling factor of safety of 4.0 was applied and verified (Appendix C, Fig. 69). Finally, the no trapped cavities requirement was satisfied with of the vent holes placed radially along the legs of the design. All specifications and requirements with their verification are shown below in Table 9.

With the unpredictability and inconsistency of metal DED printing as shown with the coupon testing, the team decided to run a Monte Carlo simulation of 350 samples on the final model. The first mode was analyzed using Ti-6AL-4V the material properties of which were found on the EOS website and are intended for use on EOSINT M printers [10]. The variances in the modulus were given and put into a script in MATLAB that used the randomize command to generate values in between the range. The .dat file from Solution 103 Real Eigenvalues was read through MATLAB and the material properties were replaced for each trail. The .dat file was then ran through nastran.exe and the first mode was taken from the F06 and saved for processing. The results were displayed in a histogram and a red line was plotted at 120 Hz to show where the cutoff for acceptable models were (Appendix C, Fig. 70). The mean was also calculated and came out to 117.57 Hz. From this information the team estimates that on average if a model were to be printed on EOS printers it would not meet the modal specification.

TABLE 9
ANALYSIS VERIFYING ALL REQUIREMENTS AND SPECIFICATIONS

Requirements & Specifications	Verification
1. The outer diameter of the SMSS (interface to the FMS) shall be 48 inches.	All geometry is contained 48-inch diameter circle.
2. The SMSS shall interface to the Forward Metering Structure (FMS) at three locations 120 degrees apart.	The FARO Arm recorded 118.0743 degrees.
3. The first mode of the SMSS shall be 120 Hz or greater when grounded at the FMS interface and supporting all hosted hardware.	The first mode is 123.38 Hz.
4. The mass of the SMSS shall be 18 lbm or less.	The final mass is 17.7071 lbm.
5. The SMSS shall have positive margins of safety against yield failure when exposed to a quasi-static load of 12 G laterally and 18 G axially simultaneously (lateral swept 15° increments) combined with a 5°C to 35°C temperature range (nominal room temp is 20°C) while supporting all hosted hardware.	The lowest margin against yield is 1.5383.
5. The SMSS shall have positive margins of safety against ultimate failure when exposed to a quasi-static load of 12 G laterally and 18 G axially simultaneously (lateral swept 15° increments) combined with a 5°C to 35°C temperature range (nominal room temp is 20°C) while supporting all hosted hardware.	The lowest margin against ultimate is 0.9384.
6. The SMSS and hosted hardware shall not obstruct more than 14% of the Primary Mirror (PM) clear aperture area (assume 1.1 m diameter clear aperture).	The SMSS and hosted hardware obstructs 13.993% of the PM clear aperture area.
7. The SMSS shall provide a stable mounting platform for the Secondary Mirror (SM) in thermal environments. The average motion of the SM interfaces under a 1°C isothermal load should be 0.66 micro-inches translation (RSS of X and Y) or less.	The RSS is 0.27 micro-inches.
7. The SMSS shall provide a stable mounting platform for the Secondary Mirror (SM) in thermal environments. The average motion of the SM interfaces under a 1°C isothermal load should be 0.037 micro-radians rotation (RSS of Rx and Ry) or less.	The RSS is 0.031 micro-radians.
The SMSS shall have positive margins of safety against buckling failure when exposed to a quasi-static load of 12 G laterally and 18 G axially simultaneously (lateral swept 15° increments) combined with a 5°C to 35°C temperature range (nominal room temp is 20°C) while supporting all hosted hardware.	The lowest buckling eigenvalue was 90.19.
Design (CAD model geometry) shall be producible with additive manufacturing methods (3D printing).	The final model is producible with blown powder DED.
There shall be no trapped cavities in the SMSS.	There are no trapped cavities in the SMSS due to radial venting.

INTELLECTUAL PROPERTY

After initial ideation and the completion of optimization, the final geometry of the team's model is unique when compared to previous years' models, as well as other SMSS designs (Appendix D, Figure 1). Some of the main people that worked on these designs are Andrew L. Bullard, Jean Dupuis, and Xu Xigu. The designs owned by companies like Thales and Boeing incorporate rods and cantilever beams in their designs; however, their geometries vary from the team's design due to the circular cross-section and the support of the structure. For instance, the design by the Thales company and the SMSS shown in Appendix D, Figure 3 incorporate vertical supporting legs (Appendix D, Fig. 2 and 3). Additionally, in Appendix D, Figures 4 and 5, the previous years' designs are shown and they differ in their main geometry and overall shape from the team's design. Based on these differences, the team's design can be patented, due to originality obtained through idealization and optimization.

SOCIETAL AND ENVIRONMENTAL IMPLICATIONS

Metal 3D printing has been in an all-time growth in the past 30 years. From companies creating fully 3D printed parts for aerospace, automotive, among many other industries, to creating full rockets using 3D printing methods. Additive manufacturing allows for the creation of more complex geometries that are often lighter and stronger than their traditionally manufactured counterparts. For aerospace applications, this translates into components that can withstand harsh conditions of space, enhancing the safety and reliability of space missions. It enables rapid prototyping and customization of parts, significantly reducing the time from design to testing. This agility can accelerate the development of technologies crucial for monitoring and responding to global health crises, such as satellites used for disease surveillance [11]. Despite the potential, there are concerns about the microstructural defects that can occur in 3D printed metals, potentially leading to failures and the loss of life. Continuous monitoring and rigorous testing are imperative to ensure that these new components do not compromise public safety. These benefits and drawbacks are all demonstrated in the design, optimization, testing, and correlation processes performed to complete this project.

In terms of accessibility, additive manufacturing democratizes the production of complex parts, potentially allowing smaller nations or organizations to participate in the aerospace industry. This can lead to a more globally distributed innovation ecosystem. The technology also presents great educational benefits in the way it fosters a culture of innovation and can significantly impact education in STEM fields by providing hands-on learning opportunities and inspiring the next generation of engineers and scientists [12]. However, the shift towards highly automated manufacturing processes could lead to displacement of workers skilled in traditional manufacturing techniques, raising concerns about employment and re-skilling challenges.

Another big implication of additive manufacturing is that its digital nature raises concerns about data security and the protection of intellectual property. Ensuring the integrity of designs and preventing unauthorized production are critical ethical considerations.

When considering environmental impact and energy use, the drawbacks to metal 3D printing are the resource intensity and the waste of material. Metal 3D printing is often energy-intensive and requires significant amounts of electricity. Furthermore, the production of metal powders can have substantial environmental footprints [13]. While additive manufacturing is touted for reducing waste by using only the necessary material, the reality is more nuanced. Metal powder that is not fused can sometimes be recycled, but there are limitations and inefficiencies associated with this process.

Some improvements and optimizations that can be done to overcome these drawbacks are 1) investing in research to improve the energy efficiency of 3D printers and the recycling efficiency of unused metal powders, 2) developing new, more sustainable materials for use in additive manufacturing with a focus on biodegradable materials and 3) conducting comprehensive lifecycle analysis of 3D printed components starting from material extraction to end-of-life disposal [13].

Overall, additive manufacturing is one of the best options for quick and cheap manufacturing of intricate parts, and it faces little societal and environmental implications when compared to other manufacturing processes. However, there is still a path for improvement and optimization for its advantages and weak points.

RECOMMENDATIONS FOR FUTURE WORK

Several important lessons were learned during the initial design phase, the optimization of the final model, and throughout all testing processes. When ordering the coupons, the team was meticulous in specifying the quantity and printing orientation for each material type, even including images for added clarity. However, a crucial detail was overlooked where the team did not provide explicit packaging instructions to the metal printing manufacturer. This oversight led to all samples being packaged together, making it impossible to distinguish the orientation of each sample group. As a result, the team was unable to determine the print orientation of the samples, even after examining them under a microscope and performing polishing and etching. To avoid such issues, future teams should ensure they provide comprehensive instructions when ordering project materials. Moreover, to minimize errors and mistakes in data analysis while improving the quality of communication documents detailing project stages, the team recommends incorporating at least three layers of review to enhance accuracy before sharing any findings with L3Harris sponsors.

The team would also recommend testing 3D metal printed coupons made of titanium. Since the team's final model met all the requirements and specifications using titanium, material data from titanium samples rather than aluminum or steel would help to improve model correlation and validation in NX simulations for displacement and vibration testing.

For future continuation of the project, the team would recommend additional time allocated to reviewing the requirements and specifications with L3Harris, specifically to confirm the limitations of shelled modeling post-processing procedures. After meeting with L3Harris, additional information was discovered regarding complications with cleanliness and finish for closed shelled parts. Bead blasting is a commonly used method to eliminate surface roughness on newly manufactured parts. For a closed shell SMSS, it may not be feasible to bead blast the interior surfaces. Thus, potential surface cracks can propagate throughout the SMSS and limit the lifespan of the part via fatigue. Also prominent, blown powder metal additive manufacturing will leave behind excess powder within the SMSS. In the possibility that this powder escapes the SMSS through the venting holes, it can dramatically impact the performance of the optical components. L3Harris has indicated that they have mesh materials available to filter out materials 21 micron in diameter, however, metal blown powder can be 15-45 micron in diameter – meaning the mesh would still allow for powder to escape even with a mesh introduced. Another potential solution discussed was chemically finishing the internal surfaces. By utilizing a chemical finishing agent, the internal faces could then be accessed and finished – eliminating the risk of surface damage propagation. While the team's shelled model meets all requirements and specifications, it requires additional research for post-processing work to ensure the structure would be suitable for an approved launch.

Finally, given additional time, the team would also continue with topology, sizing, and shape optimizations to further enhance the performance of the SMSS. The goals of these optimization methods would be to decrease weight and obstruction area while increasing stiffness. An additional improvement that could be made would be how the structure integrates with all of the required hardware. Despite meeting all initial requirements and specifications, the team recognizes there is potential for further optimization.

ACKNOWLEDGMENTS

The 2024 L3Harris Team extends appreciation to Patrick Ellsworth, Patrick Zinter, Steve Sutton, and L3Harris for their generous sponsorship, commitment, and valuable feedback throughout the duration of the engineering project. Special acknowledgment is given to Professor Christopher Muir for providing constant guidance and for teaching the team all the necessary and essential skills associated with the project. The team's gratitude also goes to Christine Pratt and Professor Sheryl Gracewski for their pivotal role in executing testing plans. The team expresses gratitude to Alex Prideaux and Jim Alkins for their support in 3D printing and Bill Mildenberger for his help with manufacturing-related tasks. Additionally, the team appreciates Professor Lambropoulos for his time, guidance, and reference materials in refining 3D-printed internal lattice structures. The team would also like to give thanks to Bill Brennessel for giving us access to an X-ray crystallography machine and to Robert Nowark for helping us process the data. All these contributions were integral to the success of the project, and the team acknowledges the collaborative efforts of all involved.

REFERENCES

[1] Budynas, R., Nisbett, J. and Shigley., 2015. Shigley's Mechanical Engineering Design. 10th ed. New York: McGraw-Hill, p.419.

[2] "What Is Equivalent Stress? | Ansys." *Ansys*, 6 Apr. 2023, www.ansys.com/blog/what-is-equivalent-stress.

[3] Woolger, Colin. "Properties: Invar - Nickel Iron Alloy." *Invar - Nickel Iron Alloy*, Materials World, June 1996, www.azom.com/article.aspx?ArticleID=515.

[4] Ryan J. Morrissey, Theodore Nicholas. Fatigue strength of Ti–6Al–4V at very long lives, International Journal of Fatigue, Volume 27, Issues 10–12, 2005, Pages 1608-1612, ISSN 0142-1123, https://doi.org/10.1016/j.ijfatigue.2005.07.009.

[5] Budynas, R., Nisbett, J. and Shigley., 2015. Shigley's Mechanical Engineering Design. 10th ed. New York: McGraw-Hill, p.404.

[6] Budynas, R., Nisbett, J. and Shigley., 2015. Shigley's Mechanical Engineering Design. 10th ed. New York: McGraw-Hill, p.425.

[7] Budynas, R., Nisbett, J. and Shigley., 2015. Shigley's Mechanical Engineering Design. 10th ed. New York: McGraw-Hill, p.431.

[8] Llis. (n.d.). https://llis.nasa.gov/lesson/810

[9] "MDS EOS Aluminium Alsi10mg." EOS GmbH. Accessed April 28, 2024. https://www.eos.info/en-us/metal-solutions/metal-materials/data-sheets/mds-eos-aluminium-alsi10mg.

[10] "Titanium for Industrial 3D Printing: EOS." EOS GmbH. Accessed April 28, 2024. https://www.eos.info/en-us/metal-solutions/metal-materials/titanium#eos-titanium-ti64.

[11] Gebler, M., Uiterkamp, A. S., & Visser, C. (2014). A global sustainability perspective on 3D printing technologies. Energy Policy,74, 158–167. https://doi.org/10.1016/j.enpol.2014.08.033

[12] Alessandro. (2022, April 6). Come funziona il Ciclo Termico. FDM - Environment Makers. https://www.dellamarca.it/en/how-the-thermal-cycle-works/

[13] Karkun, M., & Dharmalingam, S. (2022). 3D Printing Technology in Aerospace Industry – A Review. International Journal of Aviation, Aeronautics, and Aerospace,9(2).DOI:https://doi.org/10.15394/ijaaa.2022.1708

APPENDIX A

WORK BREAKDOWN STRUCTURE & CRITICAL PATH MANAGEMENT

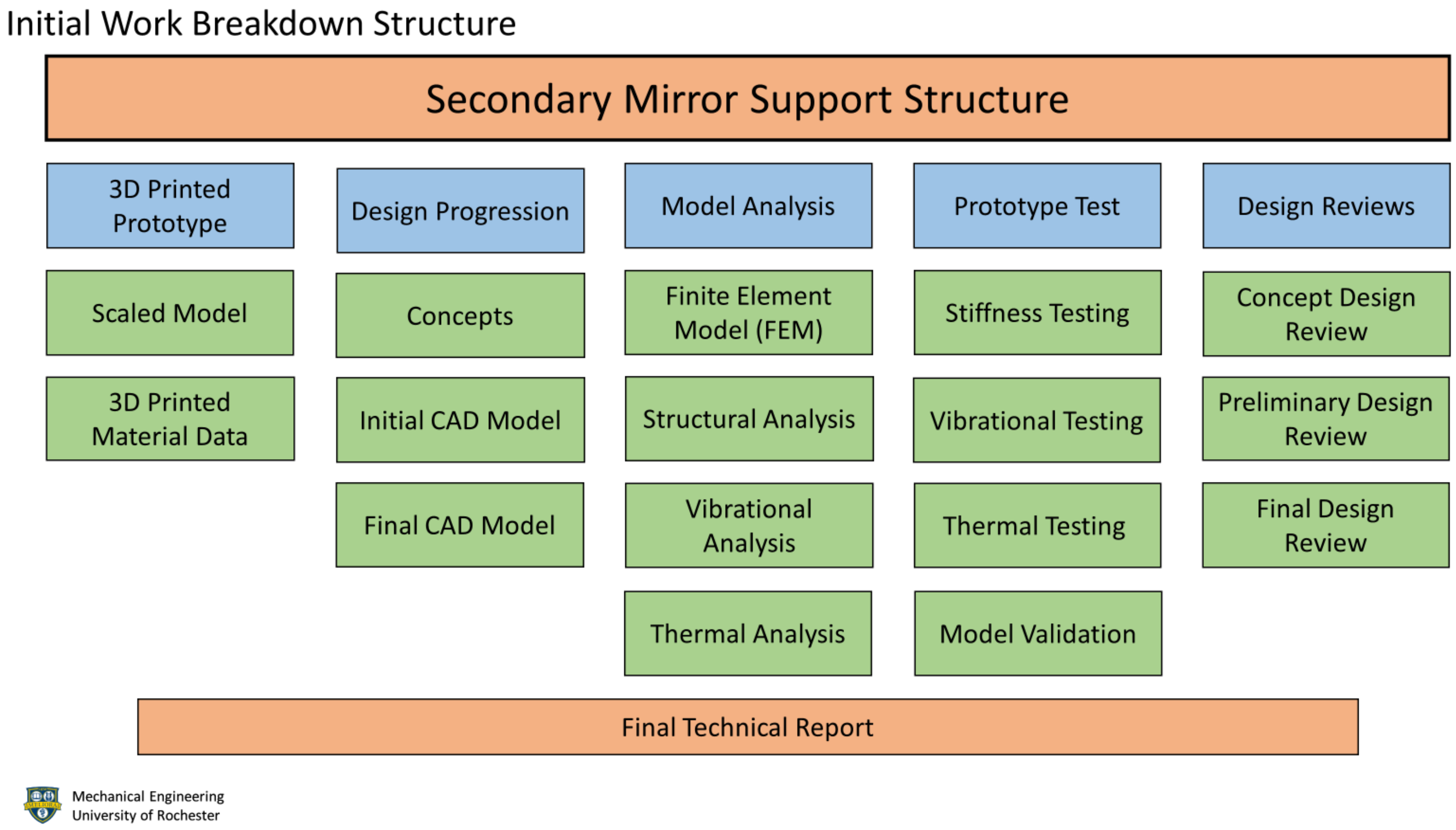

Figure 1. Work Breakdown Structure

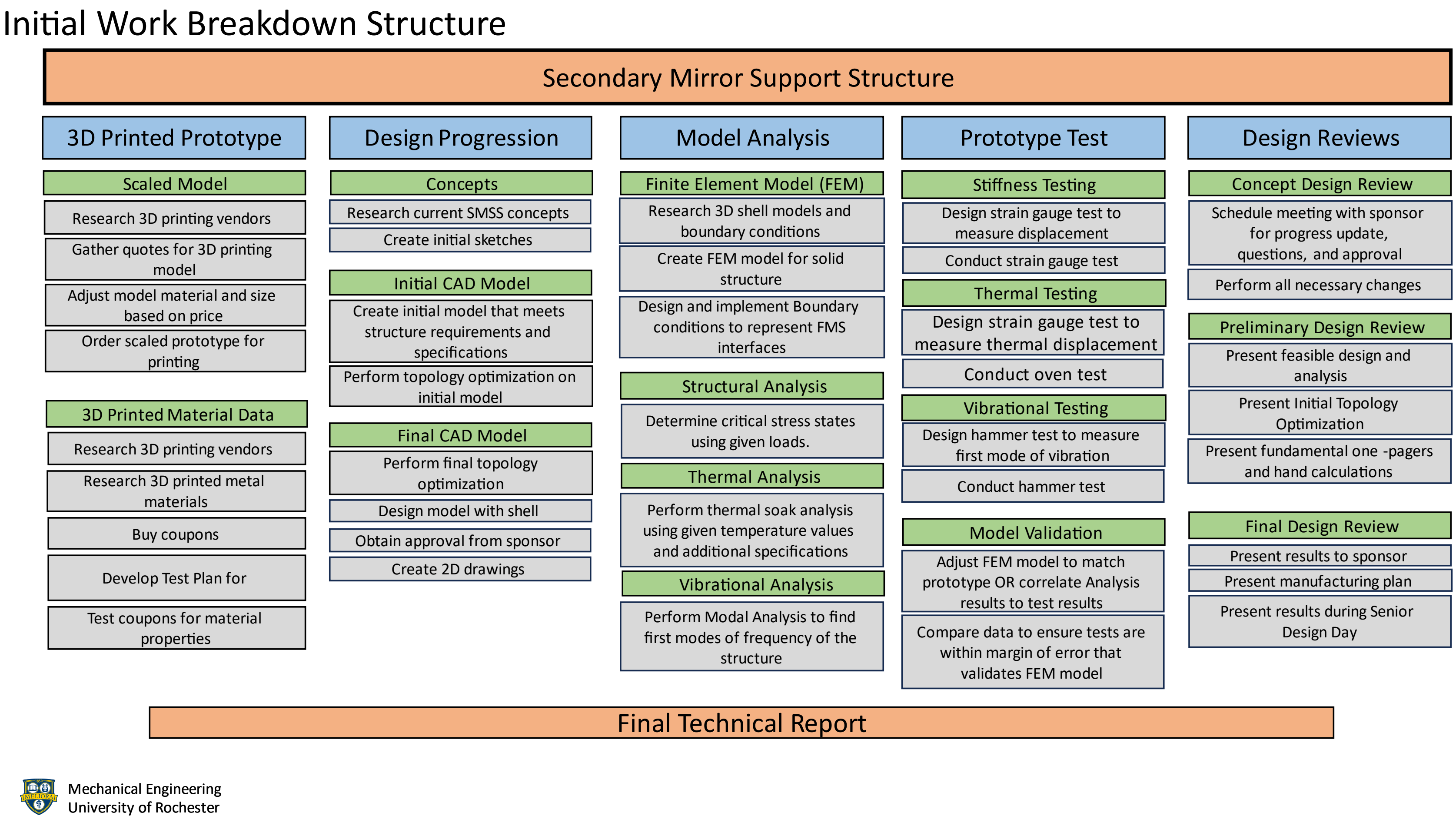

Initial Work Breakdown Structure

Secondary Mirror Support Structure

3D Printed Prototype

- Scaled Model
  - Research 3D printing vendors
  - Gather quotes for 3D printing model
  - Adjust model material and size based on price
  - Order scaled prototype for printing
- 3D Printed Material Data
  - Research 3D printing vendors
  - Research 3D printed metal materials
  - Buy coupons
  - Develop Test Plan for
  - Test coupons for material properties

Design Progression

- Concepts
  - Research current SMSS concepts
  - Create initial sketches
- Initial CAD Model
  - Create initial model that meets structure requirements and specifications
  - Perform topology optimization on initial model
- Final CAD Model
  - Perform final topology optimization
  - Design model with shell
  - Obtain approval from sponsor
  - Create 2D drawings

Model Analysis

- Finite Element Model (FEM)
  - Research 3D shell models and boundary conditions
  - Create FEM model for solid structure
  - Design and implement Boundary conditions to represent FMS interfaces
- Structural Analysis
  - Determine critical stress states using given loads.
- Thermal Analysis
  - Perform thermal soak analysis using given temperature values and additional specifications
- Vibrational Analysis
  - Perform Modal Analysis to find first modes of frequency of the structure

Prototype Test

- Stiffness Testing
  - Design strain gauge test to measure displacement
  - Conduct strain gauge test
- Thermal Testing
  - Design strain gauge test to measure thermal displacement
  - Conduct oven test
- Vibrational Testing
  - Design hammer test to measure first mode of vibration
  - Conduct hammer test
- Model Validation
  - Adjust FEM model to match prototype OR correlate Analysis results to test results
  - Compare data to ensure tests are within margin of error that validates FEM model

Design Reviews

- Concept Design Review
  - Schedule meeting with sponsor for progress update, questions, and approval
  - Perform all necessary changes
- Preliminary Design Review
  - Present feasible design and analysis
  - Present Initial Topology Optimization
  - Present fundamental one -pagers and hand calculations
- Final Design Review
  - Present results to sponsor
  - Present manufacturing plan
  - Present results during Senior Design Day

Final Technical Report

Mechanical Engineering
University of Rochester

Figure 2. Work Breakdown Structure with pertaining tasks.

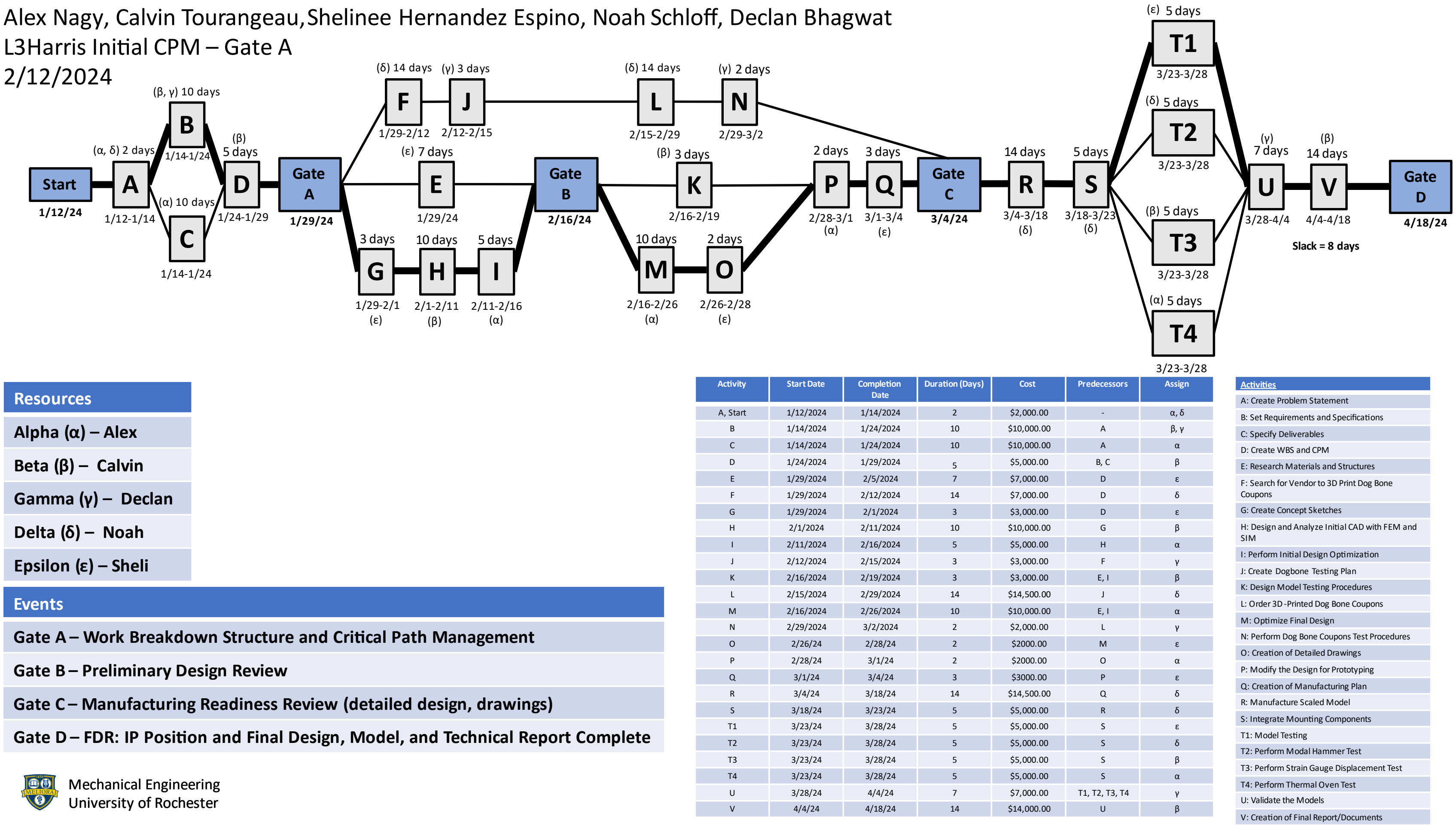

Alex Nagy, Calvin Tourangeau,Shelinee Hernandez Espino, Noah Schloff, Declan Bhagwat
L3Harris Initial CPM – Gate A
2/12/2024

Resources
Alpha (α) – Alex
Beta (β) – Calvin
Gamma (γ) – Declan
Delta (δ) – Noah
Epsilon (ε) – Sheli

Events
Gate A – Work Breakdown Structure and Critical Path Management
Gate B – Preliminary Design Review
Gate C – Manufacturing Readiness Review (detailed design, drawings)
Gate D – FDR: IP Position and Final Design, Model, and Technical Report Complete

Mechanical Engineering
University of Rochester

Activity	Start Date	Completion Date	Duration (Days)	Cost	Predecessors	Assign
A, Start	1/12/2024	1/14/2024	2	$2,000.00	-	α, δ
B	1/14/2024	1/24/2024	10	$10,000.00	A	β, γ
C	1/14/2024	1/24/2024	10	$10,000.00	A	α
D	1/24/2024	1/29/2024	5	$5,000.00	B, C	β
E	1/29/2024	2/5/2024	7	$7,000.00	D	ε
F	1/29/2024	2/12/2024	14	$7,000.00	D	δ
G	1/29/2024	2/1/2024	3	$3,000.00	D	ε
H	2/1/2024	2/11/2024	10	$10,000.00	G	β
I	2/11/2024	2/16/2024	5	$5,000.00	H	α
J	2/12/2024	2/15/2024	3	$3,000.00	F	γ
K	2/16/2024	2/19/2024	3	$3,000.00	E, I	β
L	2/15/2024	2/29/2024	14	$14,500.00	J	δ
M	2/16/2024	2/26/2024	10	$10,000.00	E, I	α
N	2/29/2024	3/2/2024	2	$2,000.00	L	γ
O	2/26/24	2/28/24	2	$2000.00	M	ε
P	2/28/24	3/1/24	2	$2000.00	O	α
Q	3/1/24	3/4/24	3	$3000.00	P	ε
R	3/4/24	3/18/24	14	$14,500.00	Q	δ
S	3/18/24	3/23/24	5	$5,000.00	R	δ
T1	3/23/24	3/28/24	5	$5,000.00	S	ε
T2	3/23/24	3/28/24	5	$5,000.00	S	δ
T3	3/23/24	3/28/24	5	$5,000.00	S	β
T4	3/23/24	3/28/24	5	$5,000.00	S	α
U	3/28/24	4/4/24	7	$7,000.00	T1, T2, T3, T4	γ
V	4/4/24	4/18/24	14	$14,000.00	U	β

Activities
A: Create Problem Statement
B: Set Requirements and Specifications
C: Specify Deliverables
D: Create WBS and CPM
E: Research Materials and Structures
F: Search for Vendor to 3D Print Dog Bone Coupons
G: Create Concept Sketches
H: Design and Analyze Initial CAD with FEM and SIM
I: Perform Initial Design Optimization
J: Create Dogbone Testing Plan
K: Design Model Testing Procedures
L: Order 3D -Printed Dog Bone Coupons
M: Optimize Final Design
N: Perform Dog Bone Coupons Test Procedures
O: Creation of Detailed Drawings
P: Modify the Design for Prototyping
Q: Creation of Manufacturing Plan
R: Manufacture Scaled Model
S: Integrate Mounting Components
T1: Model Testing
T2: Perform Modal Hammer Test
T3: Perform Strain Gauge Displacement Test
T4: Perform Thermal Oven Test
U: Validate the Models
V: Creation of Final Report/Documents

Figure 3. Critical Path Management

APPENDIX B

MECHANICAL ANALYSIS & CONCEPT SELECTION

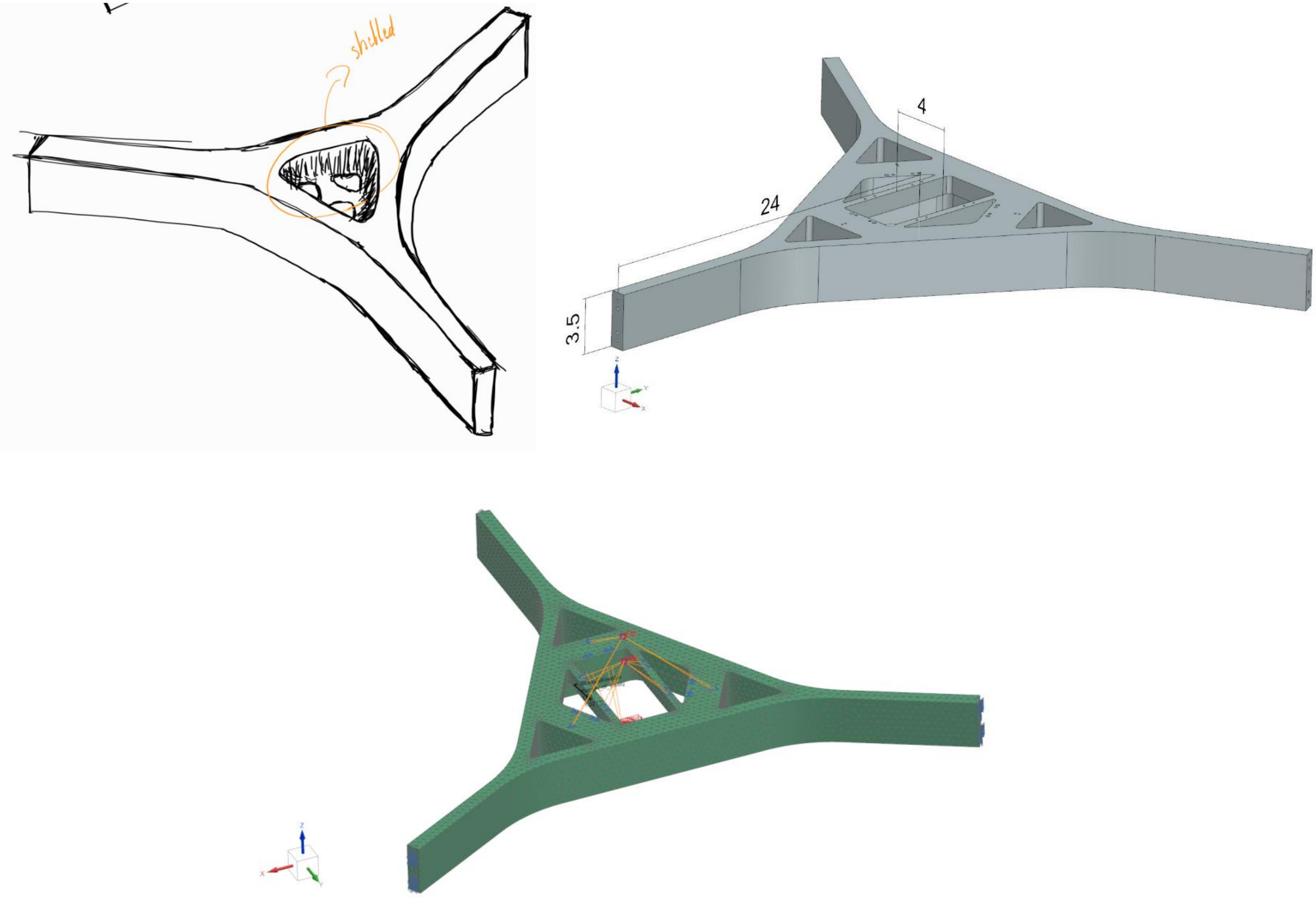

Figure 1. Concept 1 With the Sketch, CAD Model, and FEM.

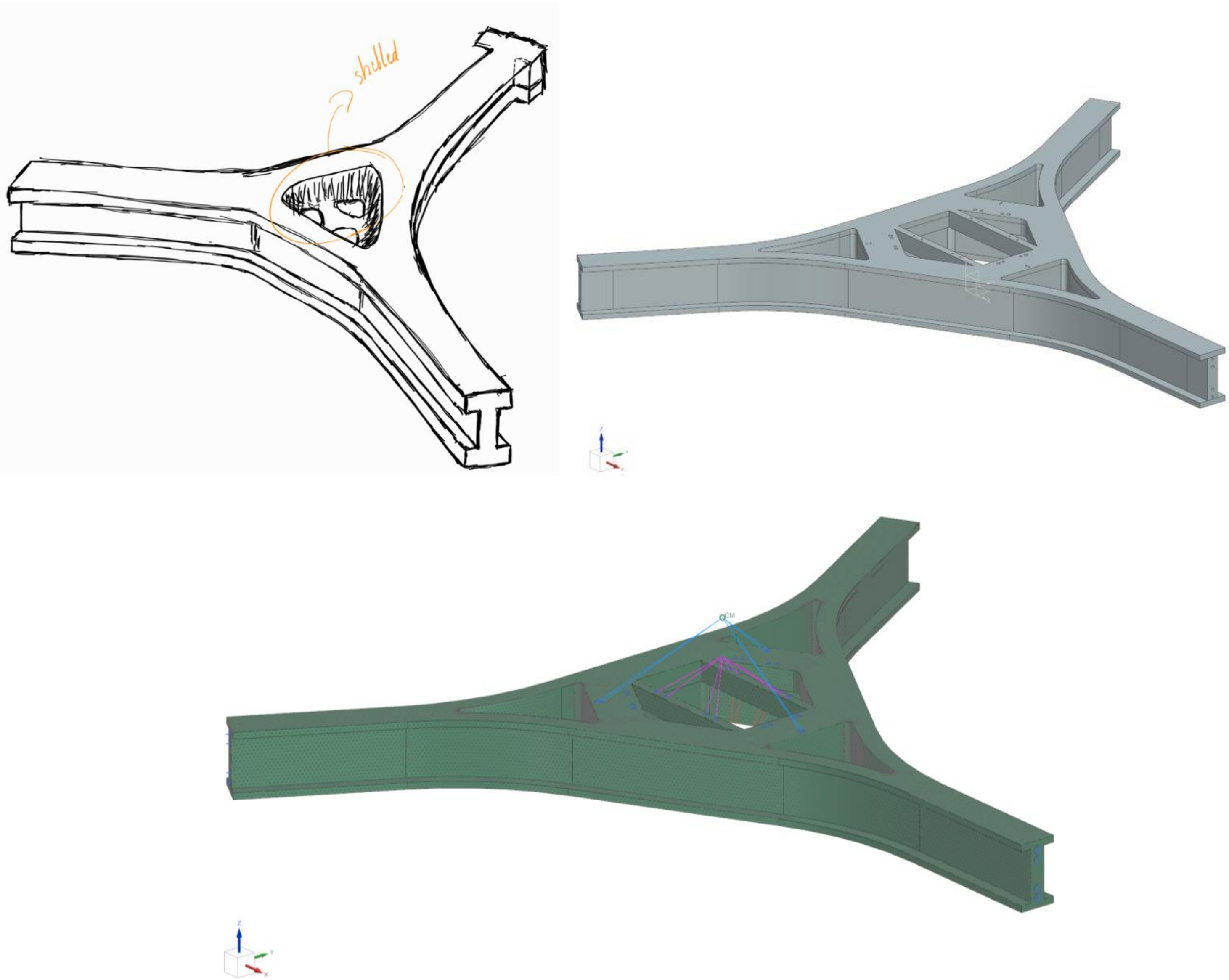

Figure 2. Concept 2 With the Sketch, CAD Model, and FEM.

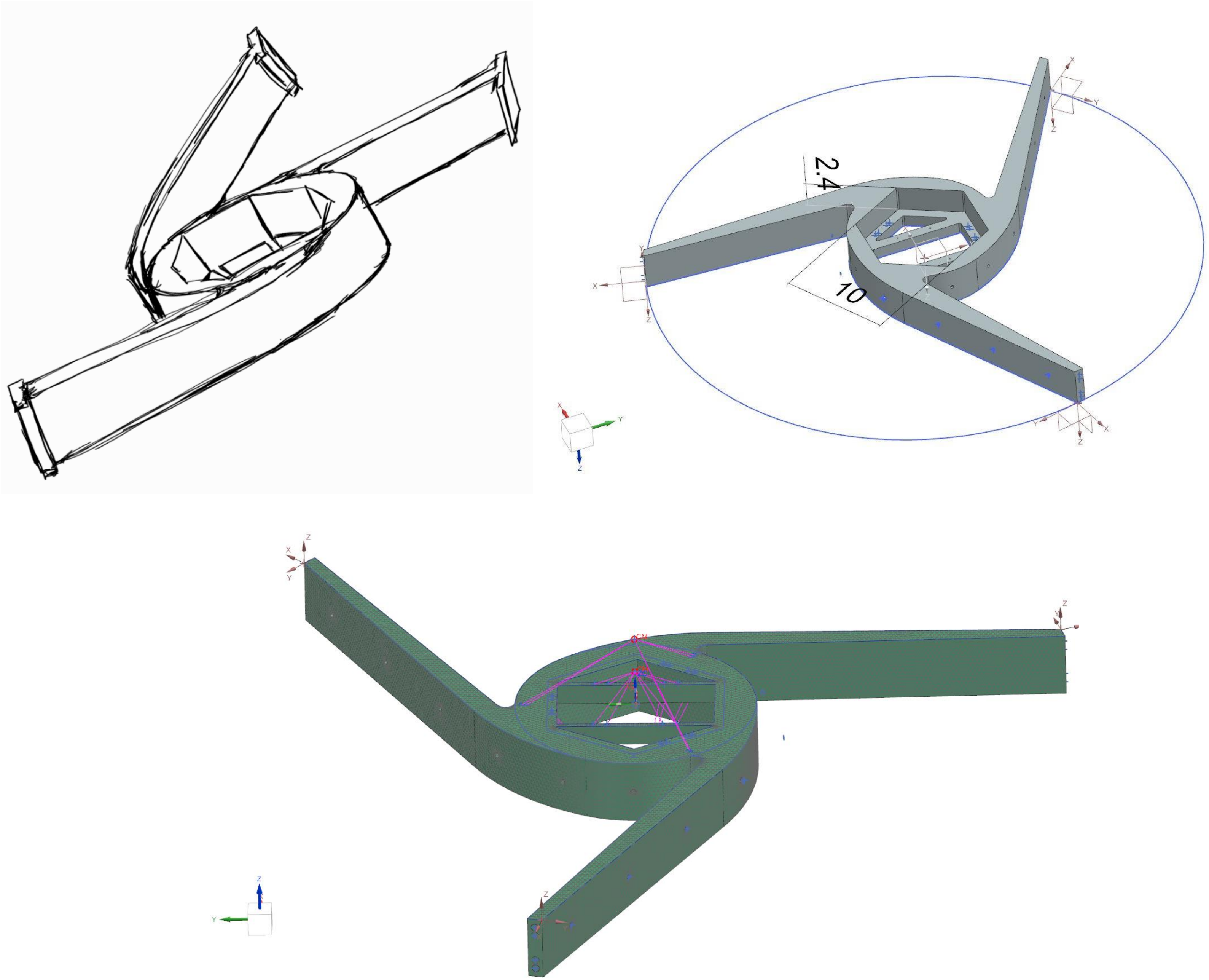

Figure 3. Concept 3 With the Sketch, CAD Model, and FEM.

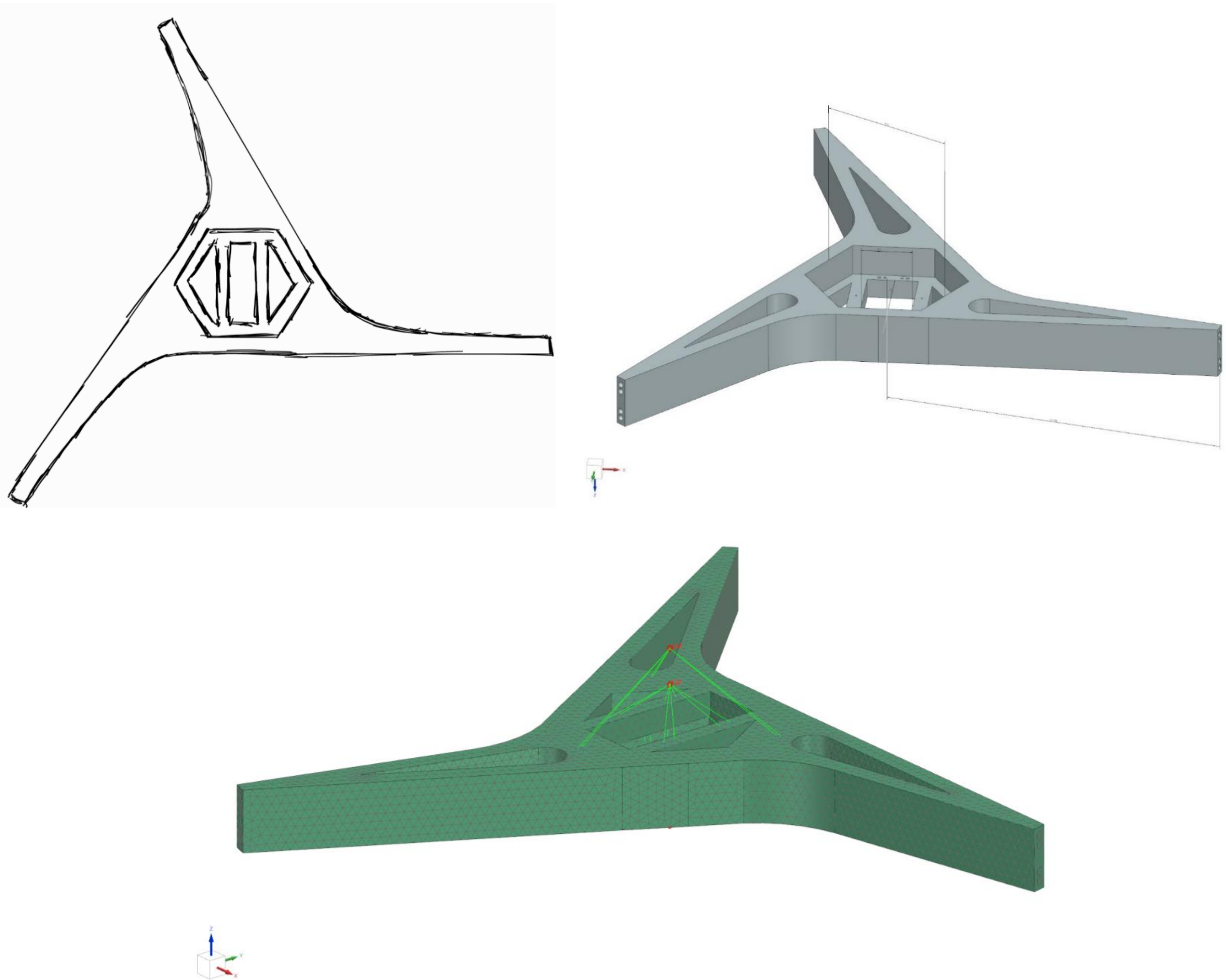

Figure 4. Concept 4 With the Sketch, CAD Model, and FEM.

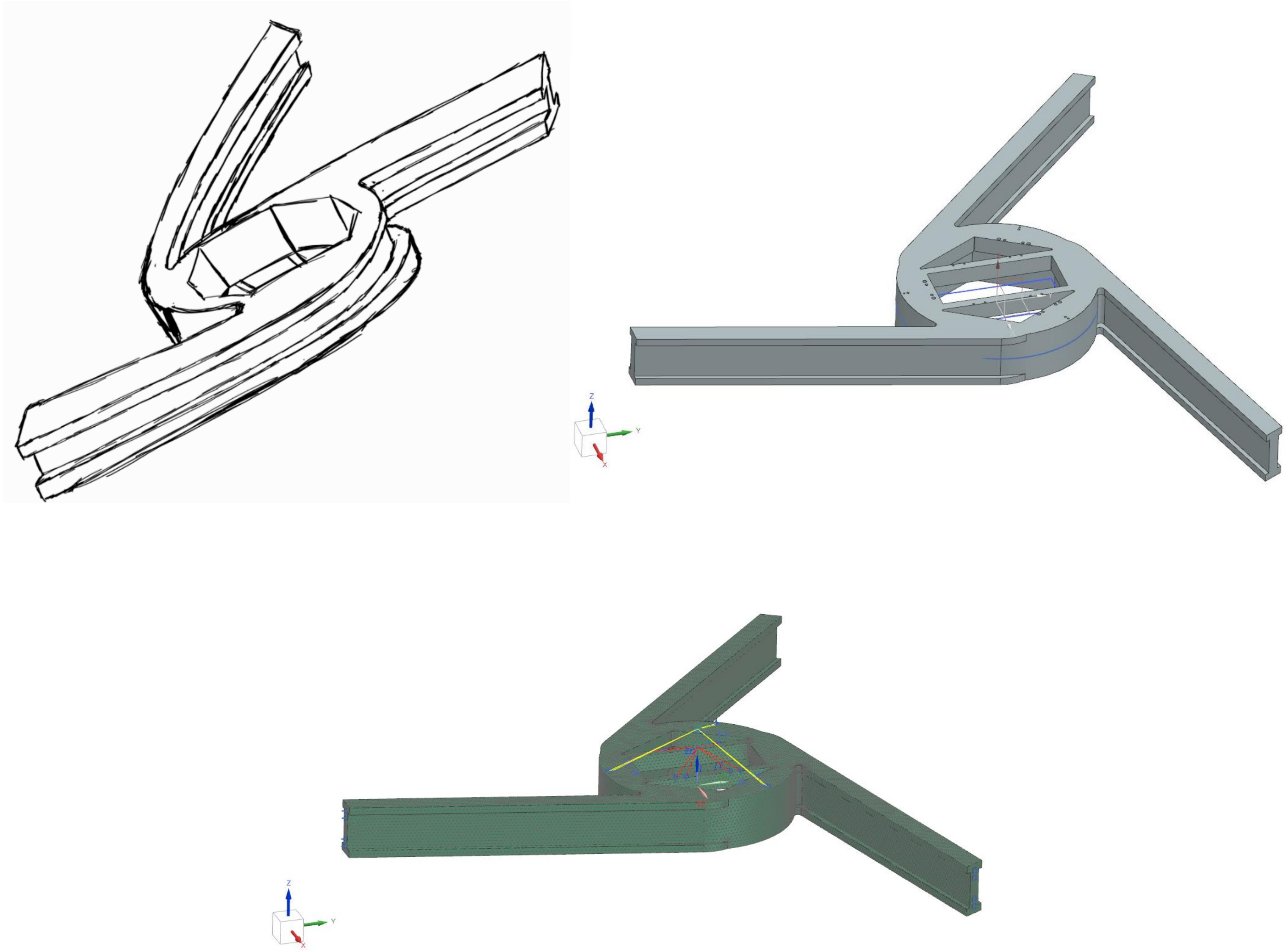

Figure 5. Concept 5 With the Sketch, CAD Model, and FEM.

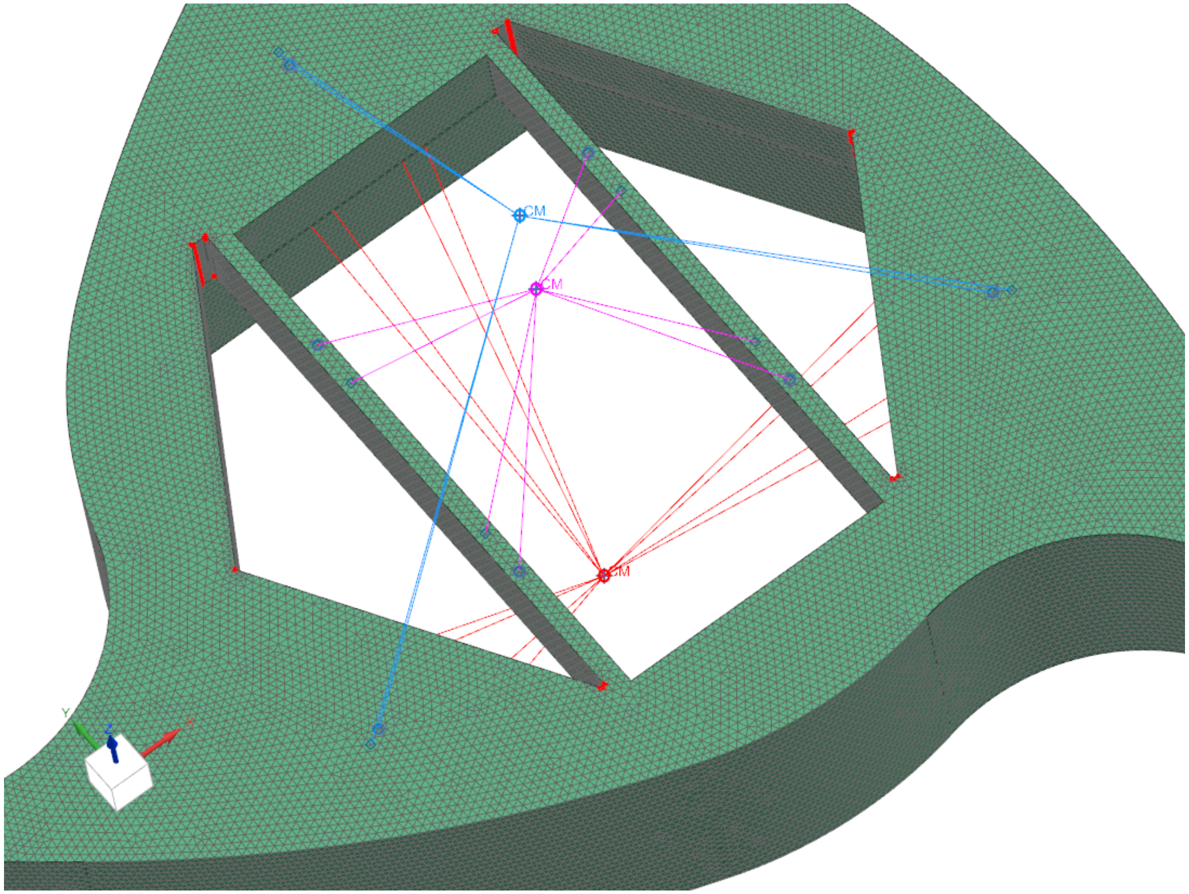

Figure 6. COMN2s Representing Actuator, Shade, and Secondary Mirror Assemblies Attached to the Model Using 0 Stiffness RBE-3 Connectors.

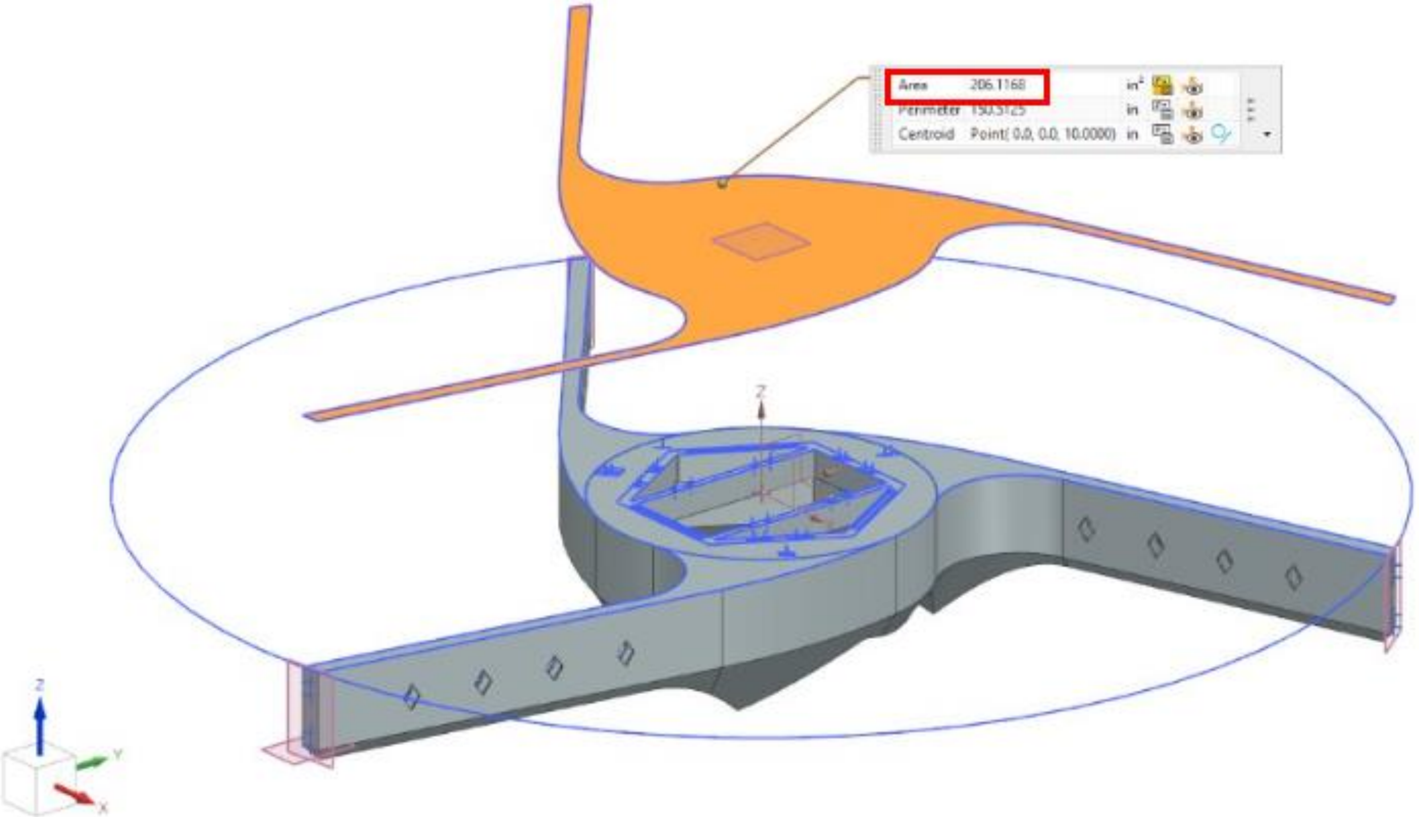

Area 206.1168 in²

Perimeter 150.5125 in

Centroid Point(0.0, 0.0, 10.0000) in

Figure 7. Obstruction Area Measurement of SMSS Using Shadow Plane.

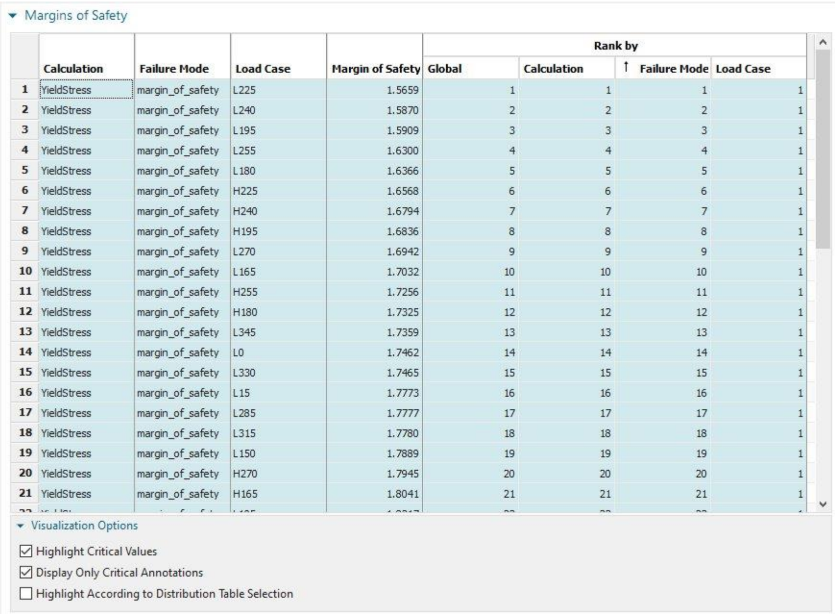

					Rank by			
	Calculation	Failure Mode	Load Case	Margin of Safety	Global	Calculation	↑ Failure Mode	Load Case
1	YieldStress	margin_of_safety	L225	1.5659	1	1	1	1
2	YieldStress	margin_of_safety	L240	1.5870	2	2	2	1
3	YieldStress	margin_of_safety	L195	1.5909	3	3	3	1
4	YieldStress	margin_of_safety	L255	1.6300	4	4	4	1
5	YieldStress	margin_of_safety	L180	1.6366	5	5	5	1
6	YieldStress	margin_of_safety	H225	1.6568	6	6	6	1
7	YieldStress	margin_of_safety	H240	1.6794	7	7	7	1
8	YieldStress	margin_of_safety	H195	1.6836	8	8	8	1
9	YieldStress	margin_of_safety	L270	1.6942	9	9	9	1
10	YieldStress	margin_of_safety	L165	1.7032	10	10	10	1
11	YieldStress	margin_of_safety	H255	1.7256	11	11	11	1
12	YieldStress	margin_of_safety	H180	1.7325	12	12	12	1
13	YieldStress	margin_of_safety	L345	1.7359	13	13	13	1
14	YieldStress	margin_of_safety	L0	1.7462	14	14	14	1
15	YieldStress	margin_of_safety	L330	1.7465	15	15	15	1
16	YieldStress	margin_of_safety	L15	1.7773	16	16	16	1
17	YieldStress	margin_of_safety	L285	1.7777	17	17	17	1
18	YieldStress	margin_of_safety	L315	1.7780	18	18	18	1
19	YieldStress	margin_of_safety	L150	1.7889	19	19	19	1
20	YieldStress	margin_of_safety	H270	1.7945	20	20	20	1
21	YieldStress	margin_of_safety	H165	1.8041	21	21	21	1

☑ Highlight Critical Values

☑ Display Only Critical Annotations

☐ Highlight According to Distribution Table Selection

Figure 8. Margin of Safety Calculation for Yield Stress.

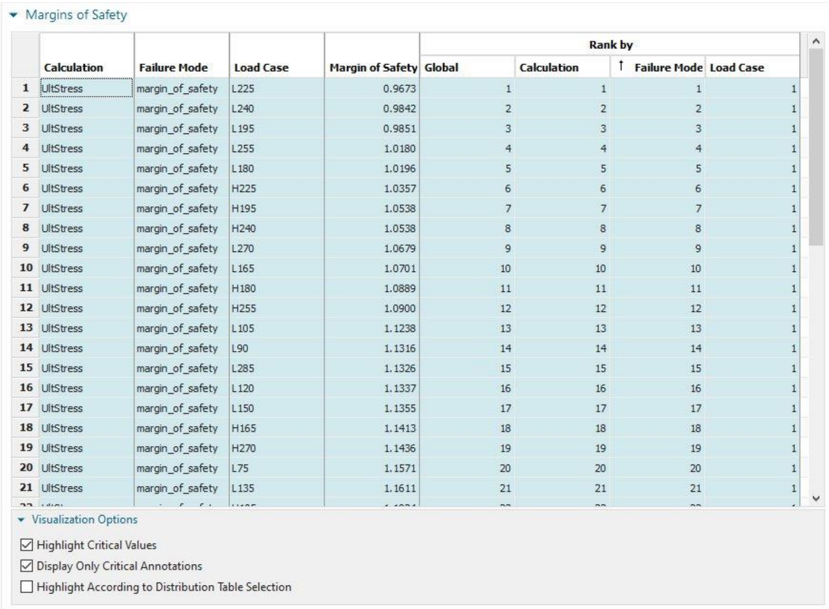

					Rank by			
	Calculation	Failure Mode	Load Case	Margin of Safety	Global	Calculation	↑ Failure Mode	Load Case
1	UltStress	margin_of_safety	L225	0.9673	1	1	1	1
2	UltStress	margin_of_safety	L240	0.9842	2	2	2	1
3	UltStress	margin_of_safety	L195	0.9851	3	3	3	1
4	UltStress	margin_of_safety	L255	1.0180	4	4	4	1
5	UltStress	margin_of_safety	L180	1.0196	5	5	5	1
6	UltStress	margin_of_safety	H225	1.0357	6	6	6	1
7	UltStress	margin_of_safety	H195	1.0538	7	7	7	1
8	UltStress	margin_of_safety	H240	1.0538	8	8	8	1
9	UltStress	margin_of_safety	L270	1.0679	9	9	9	1
10	UltStress	margin_of_safety	L165	1.0701	10	10	10	1
11	UltStress	margin_of_safety	H180	1.0889	11	11	11	1
12	UltStress	margin_of_safety	H255	1.0900	12	12	12	1
13	UltStress	margin_of_safety	L105	1.1238	13	13	13	1
14	UltStress	margin_of_safety	L90	1.1316	14	14	14	1
15	UltStress	margin_of_safety	L285	1.1326	15	15	15	1
16	UltStress	margin_of_safety	L120	1.1337	16	16	16	1
17	UltStress	margin_of_safety	L150	1.1355	17	17	17	1
18	UltStress	margin_of_safety	H165	1.1413	18	18	18	1
19	UltStress	margin_of_safety	H270	1.1436	19	19	19	1
20	UltStress	margin_of_safety	L75	1.1571	20	20	20	1
21	UltStress	margin_of_safety	L135	1.1611	21	21	21	1

☑ Highlight Critical Values

☑ Display Only Critical Annotations

☐ Highlight According to Distribution Table Selection

Figure 9. Margin of Safety Calculation for Ultimate Stress.

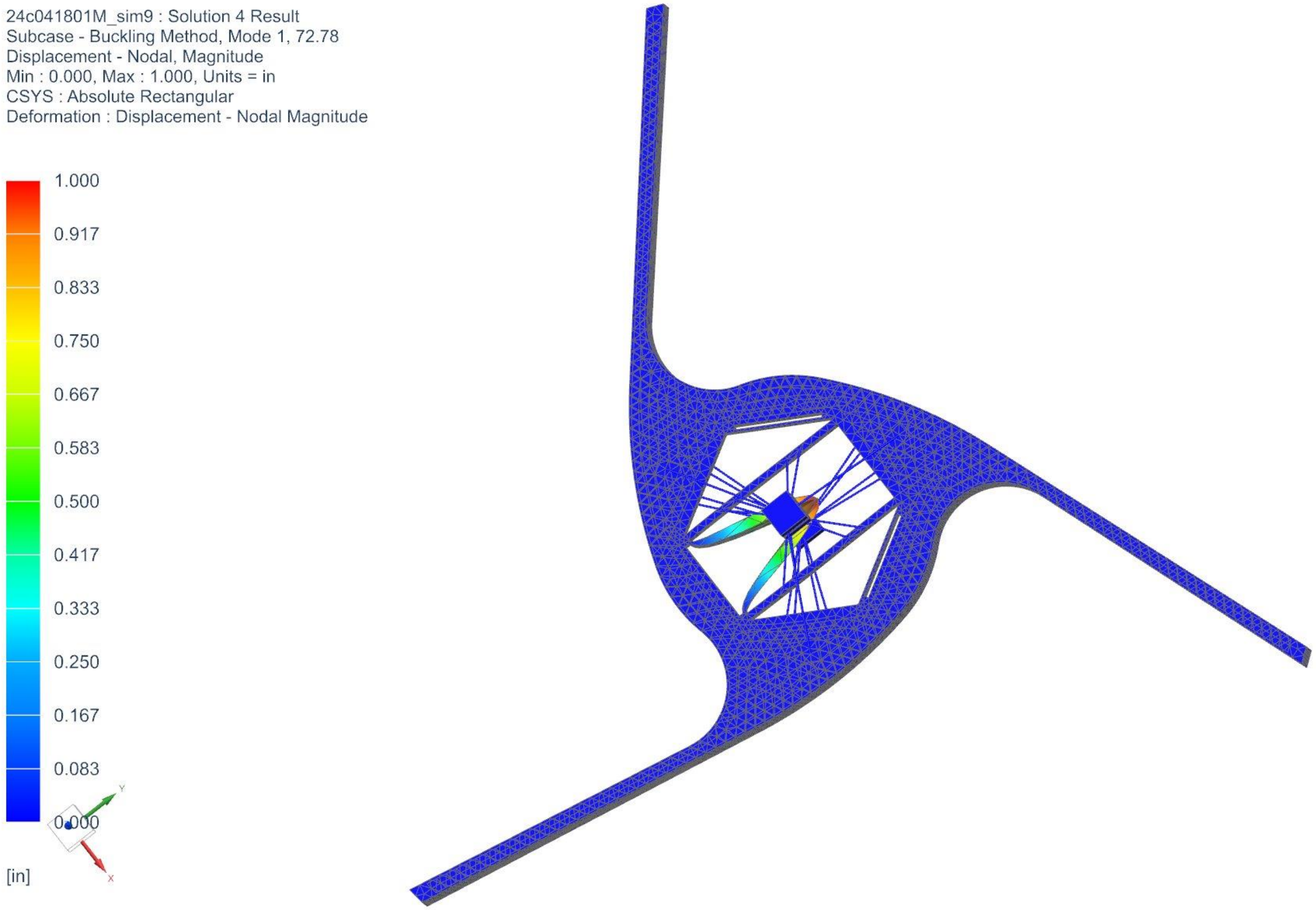

Figure 10. Buckling Analysis of FEA Model.

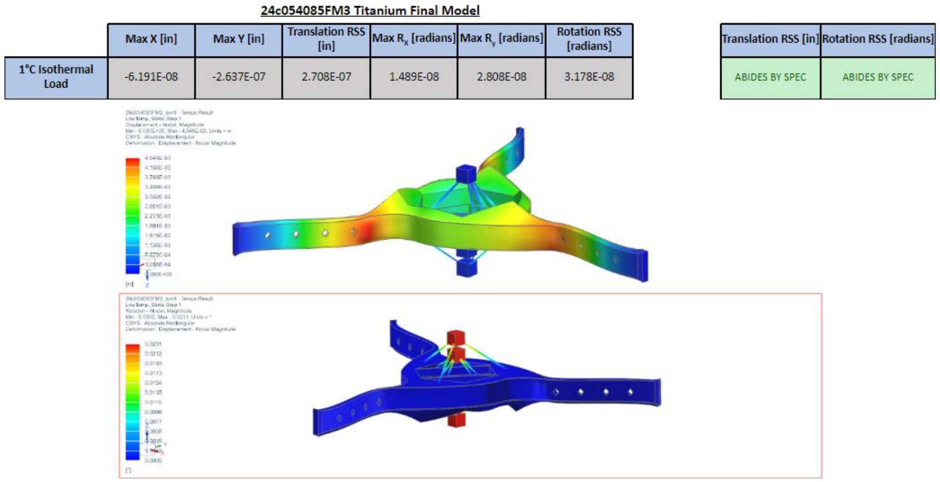

24c054085FM3 Titanium Final Model

	Max X [in]	Max Y [in]	Translation RSS [in]	Max R_x [radians]	Max R_y [radians]	Rotation RSS [radians]
1°C Isothermal Load	-6.191E-08	-2.637E-07	2.708E-07	1.489E-08	2.808E-08	3.178E-08

Translation RSS [in]	Rotation RSS [radians]
ABIDES BY SPEC	ABIDES BY SPEC

Figure 11. Thermal Load Analysis to Determine Secondary Mirror Deformation.

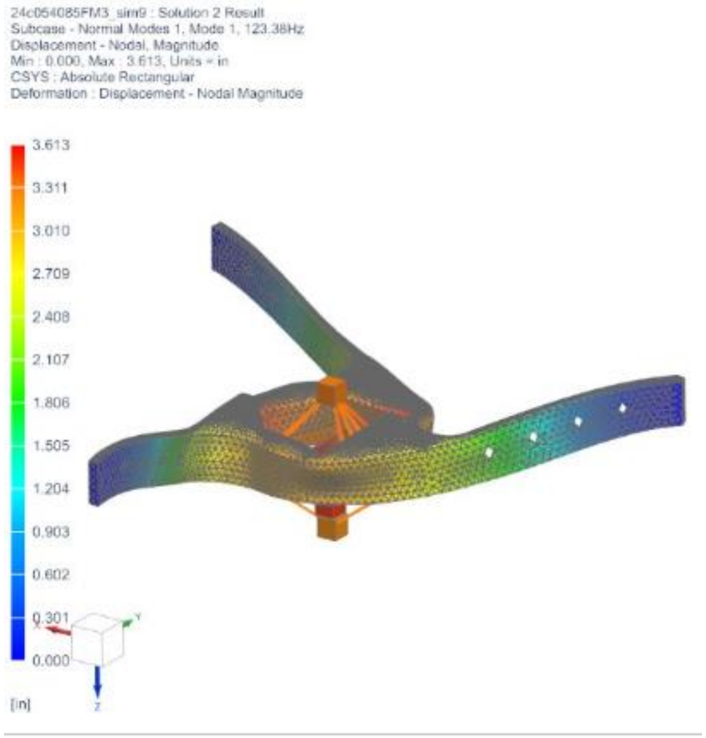

Figure 12. Modal Vibration Analysis of FEA Model.

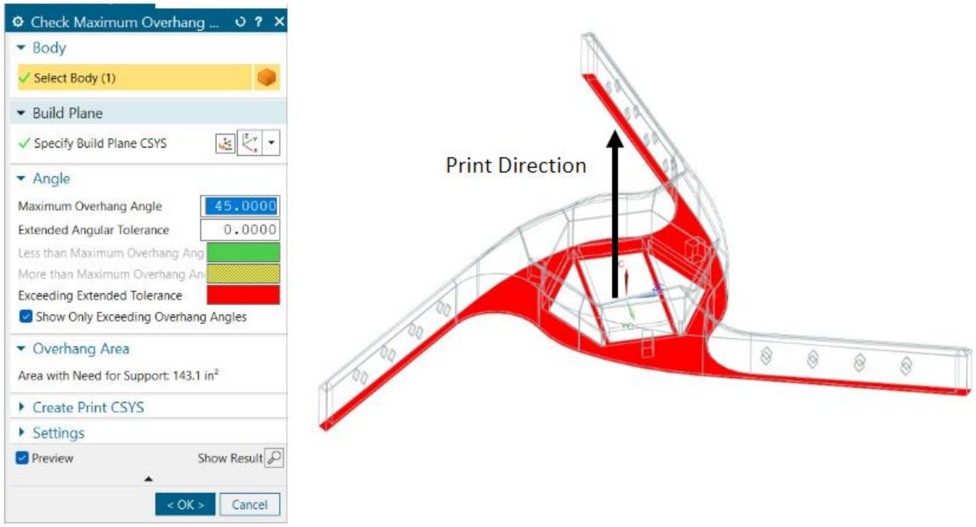

Check Maximum Overhang ...

Body

☑ Select Body (1)

Build Plane

✓ Specify Build Plane CSYS

Angle

Maximum Overhang Angle 45.0000

Extended Angular Tolerance 0.0000

Less than Maximum Overhang Ang 🟩

More than Maximum Overhang An ▨

Exceeding Extended Tolerance 🟥

☑ Show Only Exceeding Overhang Angles

Overhang Area

Area with Need for Support: 143.1 in^2

Create Print CSYS

Settings

☑ Preview

Figure 13. NX Maximum Overhang Angle Tool Used to Determine Model Printability.

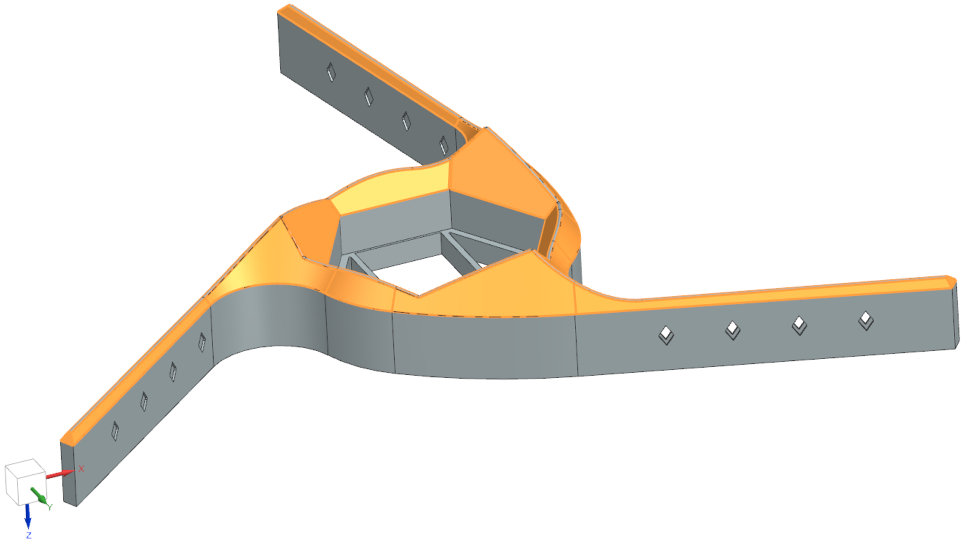

Figure 14. Angled Extrusion Added to Bottom of Model to Make it Printable Using Powder Bed Fusion.

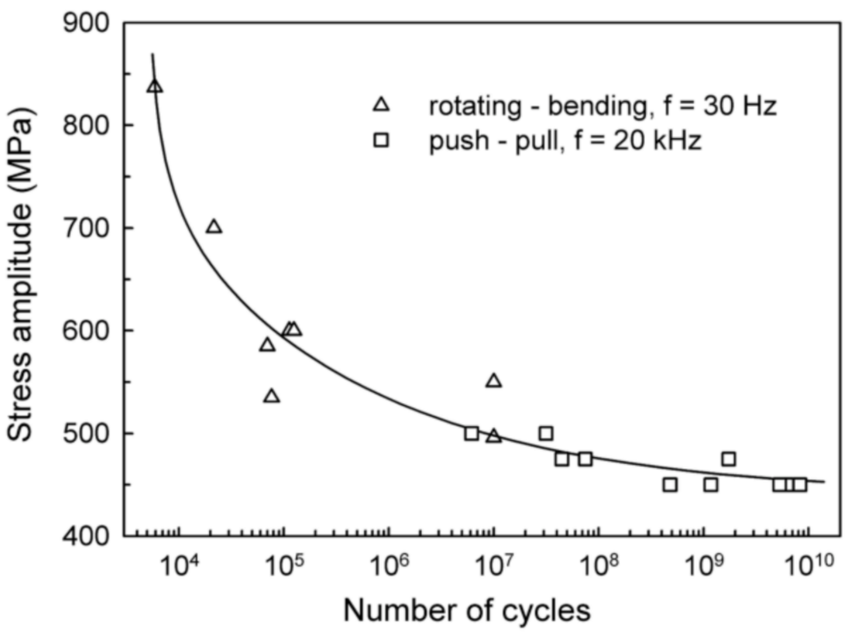

Figure 15. Stress vs. Cycles to Failure Curve of Ti-6AL-4V Alloy [4].

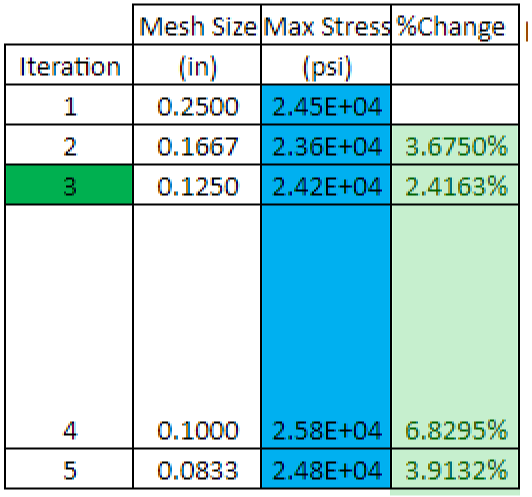

	Mesh Size	Max Stress	%Change
Iteration	(in)	(psi)	
1	0.2500	2.45E+04	
2	0.1667	2.36E+04	3.6750%
3	0.1250	2.42E+04	2.4163%
4	0.1000	2.58E+04	6.8295%
5	0.0833	2.48E+04	3.9132%

Figure 16. Convergence Study Results For Final Study.

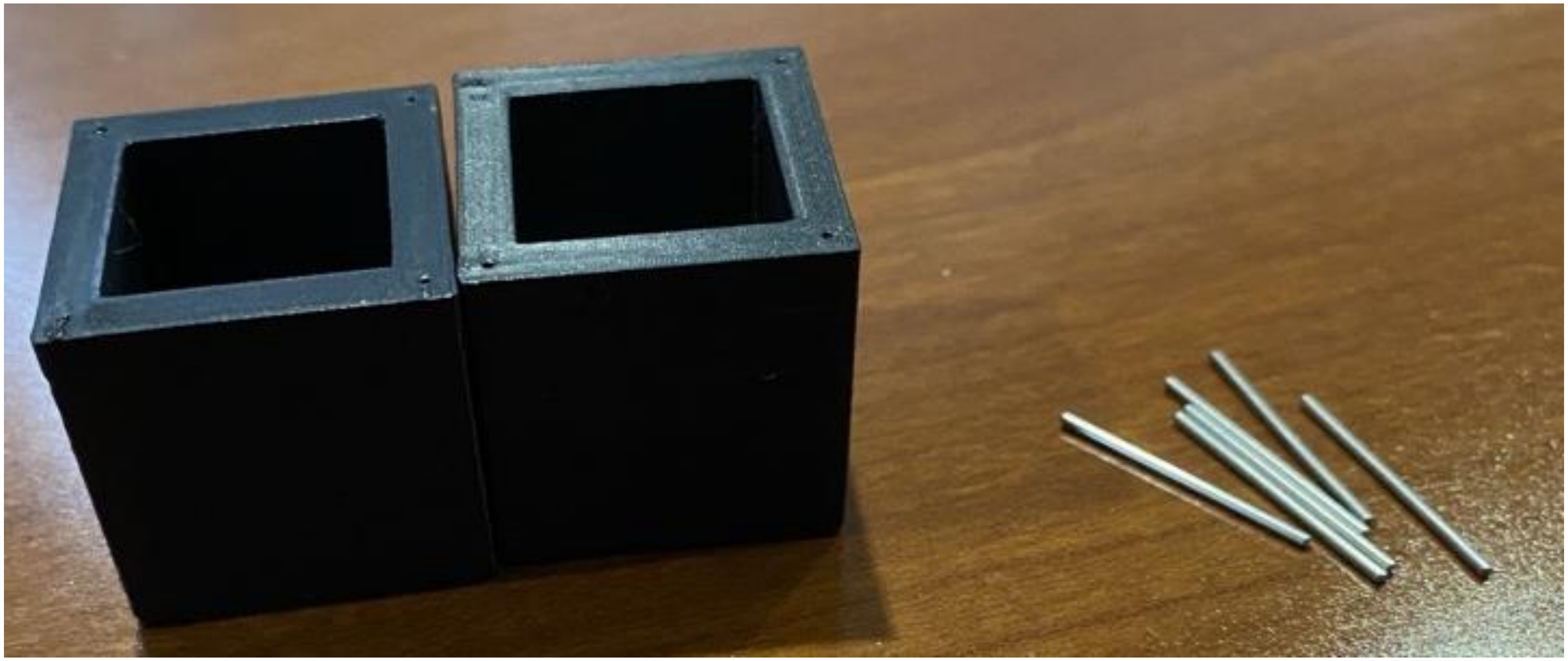

Figure 17. 3D Printed Cubes and Pins to Evaluate Printed Hole Tolerances.

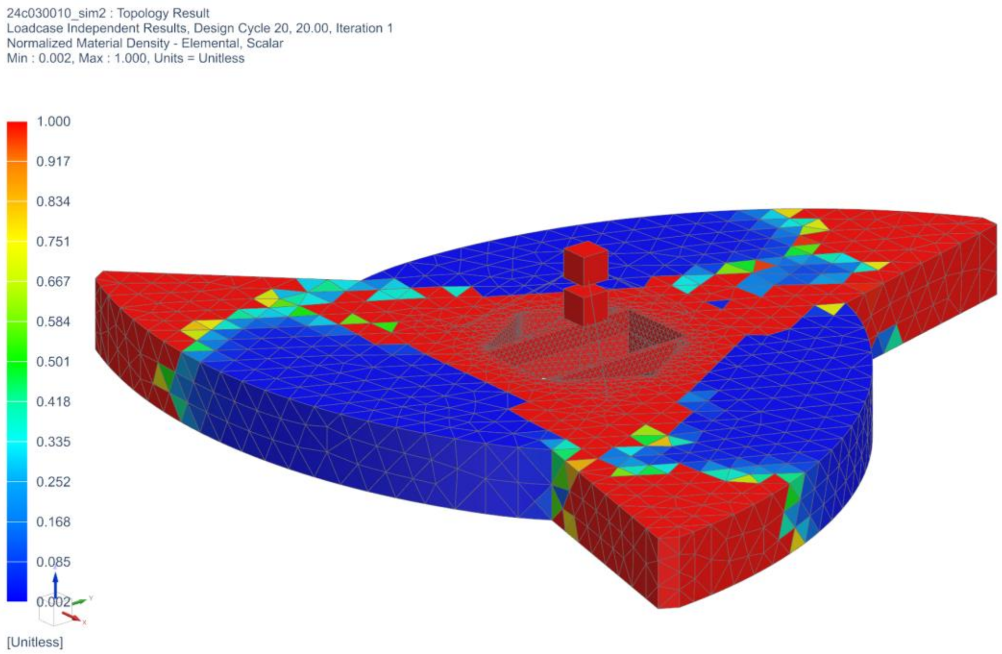

Figure 18. Topology Optimization.

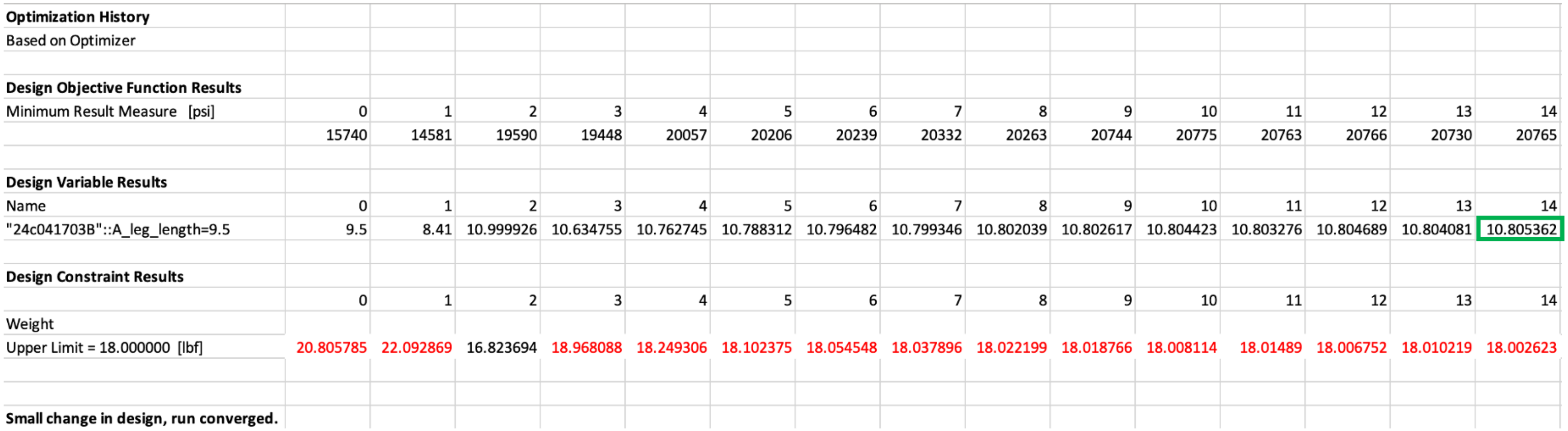

Optimization History															
Based on Optimizer															
Design Objective Function Results															
Minimum Result Measure [psi]	0	1	2	3	4	5	6	7	8	9	10	11	12	13	14
	15740	14581	19590	19448	20057	20206	20239	20332	20263	20744	20775	20763	20766	20730	20765
Design Variable Results															
Name	0	1	2	3	4	5	6	7	8	9	10	11	12	13	14
"24c041703B"::A_leg_length=9.5	9.5	8.41	10.999926	10.634755	10.762745	10.788312	10.796482	10.799346	10.802039	10.802617	10.804423	10.803276	10.804689	10.804081	10.805362
Design Constraint Results															
	0	1	2	3	4	5	6	7	8	9	10	11	12	13	14
Weight															
Upper Limit = 18.000000 [lbf]	20.805785	22.092869	16.823694	18.968088	18.249306	18.102375	18.054548	18.037896	18.022199	18.018766	18.008114	18.01489	18.006752	18.010219	18.002623
Small change in design, run converged.															

Figure 19. Shape Optimization of Concept 1 Using a Design Objective of Minimizing the von Mises Stress.

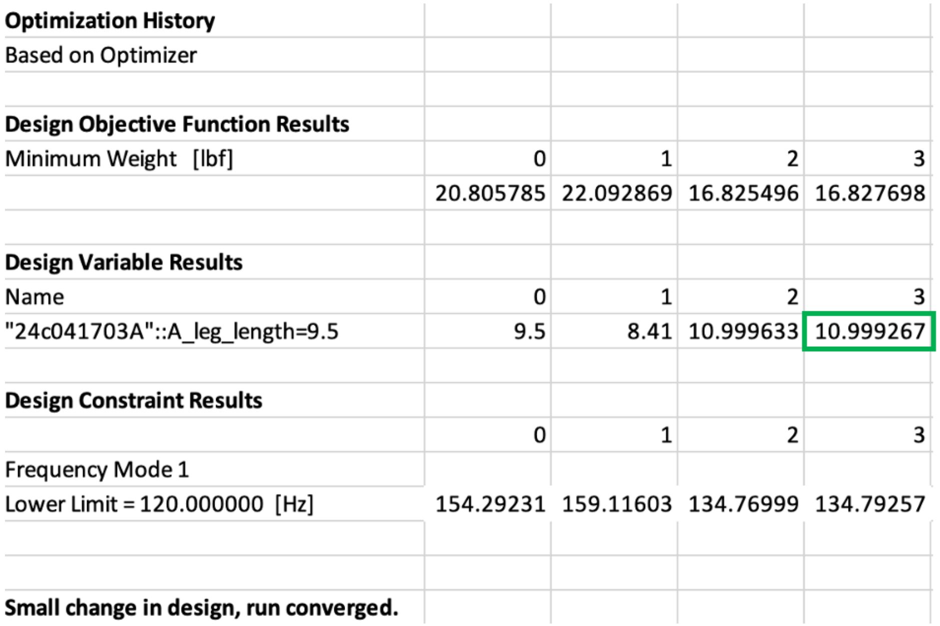

Optimization History				
Based on Optimizer				
Design Objective Function Results				
Minimum Weight [lbf]	0	1	2	3
	20.805785	22.092869	16.825496	16.827698
Design Variable Results				
Name	0	1	2	3
"24c041703A"::A_leg_length=9.5	9.5	8.41	10.999633	10.999267
Design Constraint Results				
	0	1	2	3
Frequency Mode 1				
Lower Limit = 120.000000 [Hz]	154.29231	159.11603	134.76999	134.79257
Small change in design, run converged.				

Figure 20. Shape Optimization of Concept 1 Using a Design Objective of Minimizing the SMSS Weight.

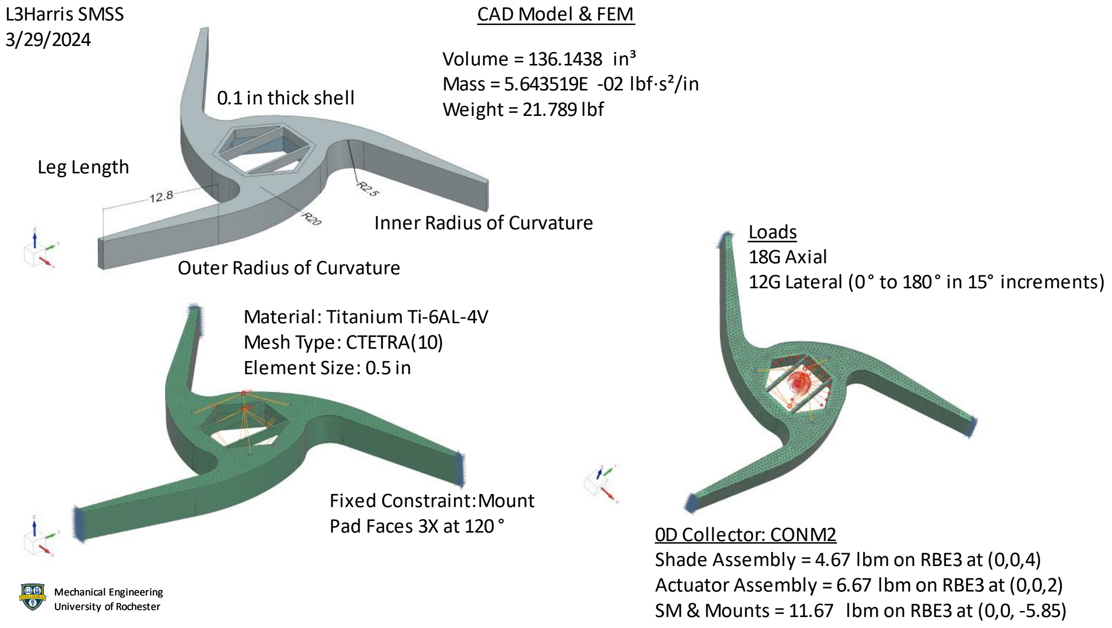

L3Harris SMSS
3/29/2024

CAD Model & FEM

Volume = 136.1438 in^3
Mass = 5.643519E -02 $lbf \cdot s^2/in$
Weight = 21.789 lbf

Material: Titanium Ti-6AL-4V
Mesh Type: CTETRA(10)
Element Size: 0.5 in

Fixed Constraint: Mount Pad Faces 3X at 120°

Loads
18G Axial
12G Lateral (0° to 180° in 15° increments)

0D Collector: CONM2
Shade Assembly = 4.67 lbm on RBE3 at (0,0,4)
Actuator Assembly = 6.67 lbm on RBE3 at (0,0,2)
SM & Mounts = 11.67 lbm on RBE3 at (0,0, -5.85)

Figure 21. CAD and FEM Setup of the Circular Model Before Optimization.

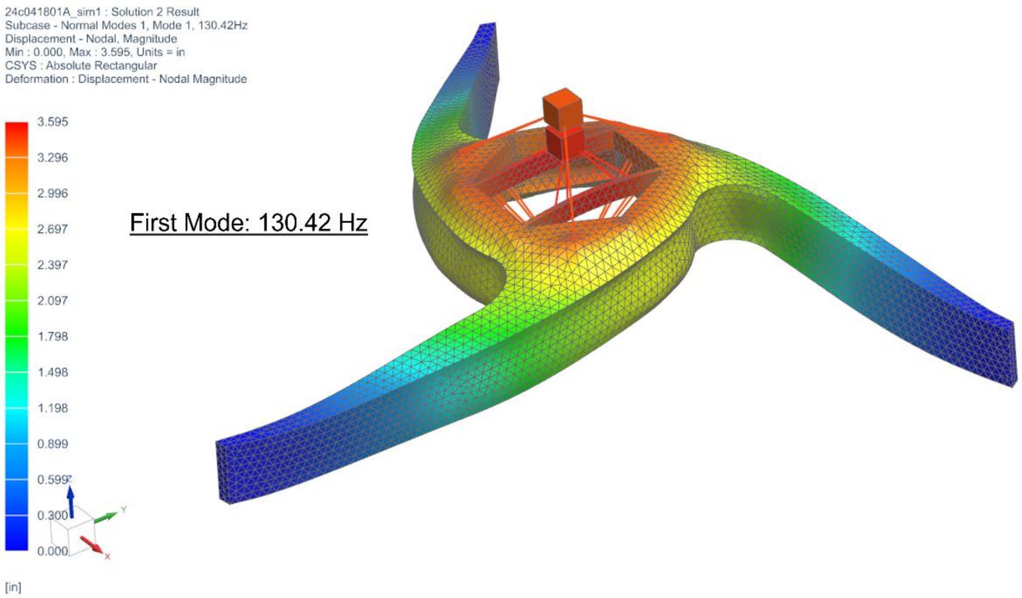

Figure 22. First Mode of Vibration for the Unoptimized Circular Model.

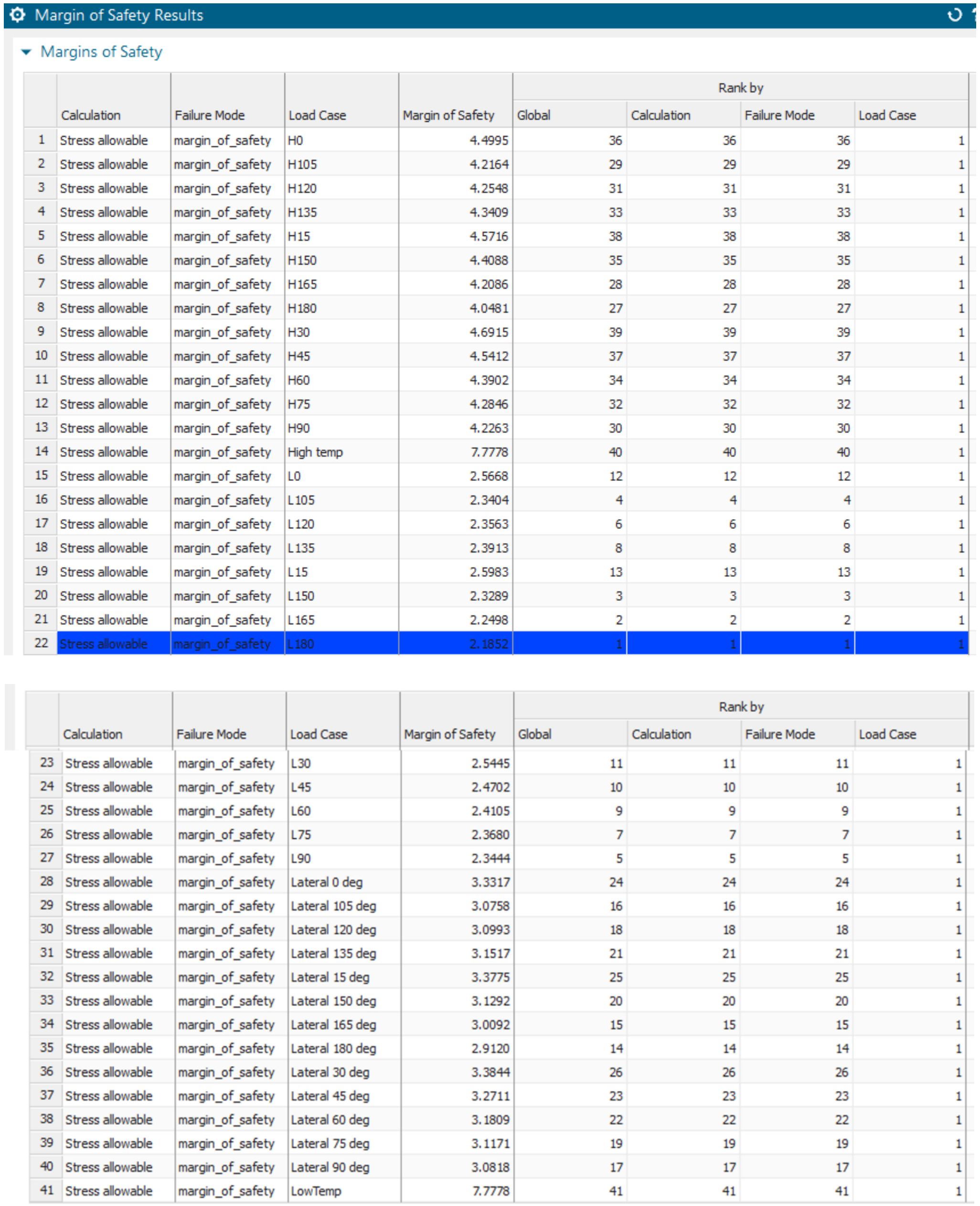

	Calculation	Failure Mode	Load Case	Margin of Safety	Rank by			
					Global	Calculation	Failure Mode	Load Case
1	Stress allowable	margin_of_safety	H0	4.4995	36	36	36	1
2	Stress allowable	margin_of_safety	H105	4.2164	29	29	29	1
3	Stress allowable	margin_of_safety	H120	4.2548	31	31	31	1
4	Stress allowable	margin_of_safety	H135	4.3409	33	33	33	1
5	Stress allowable	margin_of_safety	H15	4.5716	38	38	38	1
6	Stress allowable	margin_of_safety	H150	4.4088	35	35	35	1
7	Stress allowable	margin_of_safety	H165	4.2086	28	28	28	1
8	Stress allowable	margin_of_safety	H180	4.0481	27	27	27	1
9	Stress allowable	margin_of_safety	H30	4.6915	39	39	39	1
10	Stress allowable	margin_of_safety	H45	4.5412	37	37	37	1
11	Stress allowable	margin_of_safety	H60	4.3902	34	34	34	1
12	Stress allowable	margin_of_safety	H75	4.2846	32	32	32	1
13	Stress allowable	margin_of_safety	H90	4.2263	30	30	30	1
14	Stress allowable	margin_of_safety	High temp	7.7778	40	40	40	1
15	Stress allowable	margin_of_safety	L0	2.5668	12	12	12	1
16	Stress allowable	margin_of_safety	L105	2.3404	4	4	4	1
17	Stress allowable	margin_of_safety	L120	2.3563	6	6	6	1
18	Stress allowable	margin_of_safety	L135	2.3913	8	8	8	1
19	Stress allowable	margin_of_safety	L15	2.5983	13	13	13	1
20	Stress allowable	margin_of_safety	L150	2.3289	3	3	3	1
21	Stress allowable	margin_of_safety	L165	2.2498	2	2	2	1
22	Stress allowable	margin_of_safety	L180	2.1852	1	1	1	1
23	Stress allowable	margin_of_safety	L30	2.5445	11	11	11	1
24	Stress allowable	margin_of_safety	L45	2.4702	10	10	10	1
25	Stress allowable	margin_of_safety	L60	2.4105	9	9	9	1
26	Stress allowable	margin_of_safety	L75	2.3680	7	7	7	1
27	Stress allowable	margin_of_safety	L90	2.3444	5	5	5	1
28	Stress allowable	margin_of_safety	Lateral 0 deg	3.3317	24	24	24	1
29	Stress allowable	margin_of_safety	Lateral 105 deg	3.0758	16	16	16	1
30	Stress allowable	margin_of_safety	Lateral 120 deg	3.0993	18	18	18	1
31	Stress allowable	margin_of_safety	Lateral 135 deg	3.1517	21	21	21	1
32	Stress allowable	margin_of_safety	Lateral 15 deg	3.3775	25	25	25	1
33	Stress allowable	margin_of_safety	Lateral 150 deg	3.1292	20	20	20	1
34	Stress allowable	margin_of_safety	Lateral 165 deg	3.0092	15	15	15	1
35	Stress allowable	margin_of_safety	Lateral 180 deg	2.9120	14	14	14	1
36	Stress allowable	margin_of_safety	Lateral 30 deg	3.3844	26	26	26	1
37	Stress allowable	margin_of_safety	Lateral 45 deg	3.2711	23	23	23	1
38	Stress allowable	margin_of_safety	Lateral 60 deg	3.1809	22	22	22	1
39	Stress allowable	margin_of_safety	Lateral 75 deg	3.1171	19	19	19	1
40	Stress allowable	margin_of_safety	Lateral 90 deg	3.0818	17	17	17	1
41	Stress allowable	margin_of_safety	LowTemp	7.7778	41	41	41	1

Figure 23. Margin of Safety Calculations for All Combined Load Cases on the Unoptimized Circular Model. The 18G axial load, 12G Lateral Load at 180°, and the 20°C to 5°C Temperature Change was Calculated to be the Worst-Case Loading While Maintaining a Positive Margin at 2.1852.

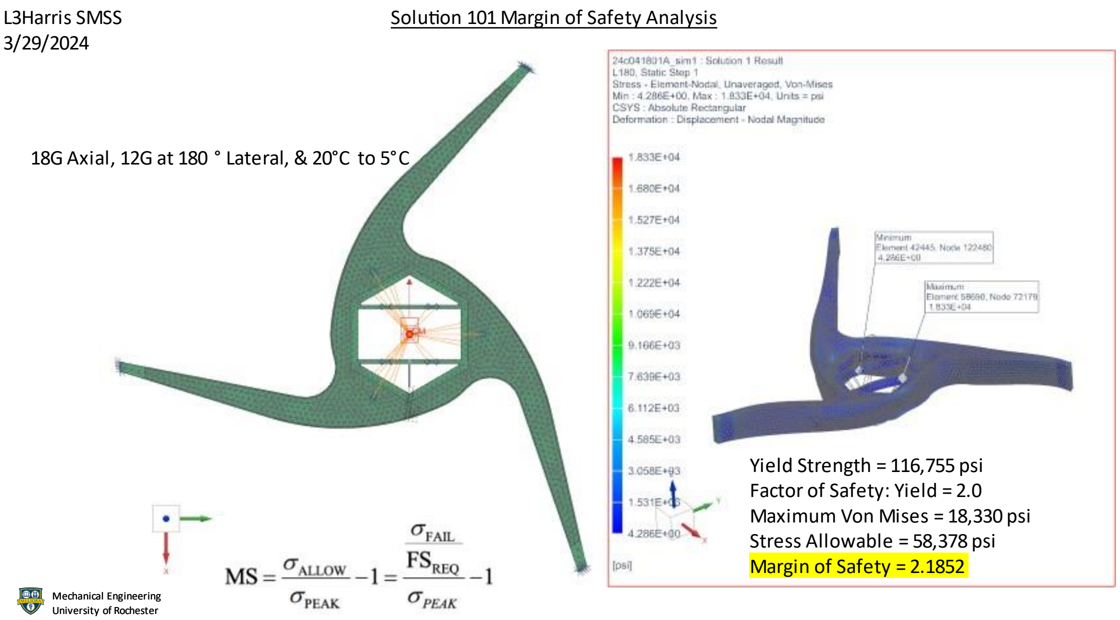

L3Harris SMSS
3/29/2024

Solution 101 Margin of Safety Analysis

18G Axial, 12G at 180 ° Lateral, & 20°C to 5°C

24c041801A_sim1 : Solution 1 Result
L180, Static Step 1
Stress - Element-Nodal, Unaveraged, Von-Mises
Min : 4.286E+00, Max : 1.833E+04, Units = psi
CSYS : Absolute Rectangular
Deformation : Displacement - Nodal Magnitude

$$MS = \frac{\sigma_{\text{ALLOW}}}{\sigma_{\text{PEAK}}} - 1 = \frac{\frac{\sigma_{\text{FAIL}}}{\text{FS}_{\text{REQ}}}}{\sigma_{PEAK}} - 1$$

Yield Strength = 116,755 psi
Factor of Safety: Yield = 2.0
Maximum Von Mises = 18,330 psi
Stress Allowable = 58,378 psi
Margin of Safety = 2.1852

Mechanical Engineering
University of Rochester

Figure 24. The Stress Plot for the Worst-Case Load on the Unoptimized Circular Model with a Margin Calculation Confirming the NX Calculation.

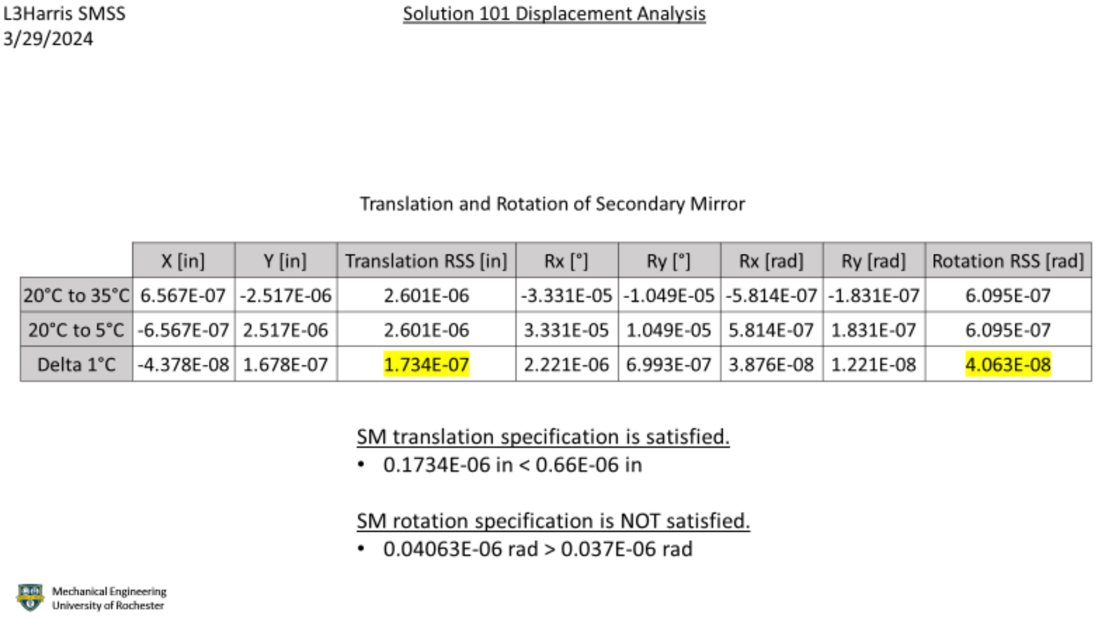

L3Harris SMSS
3/29/2024

Solution 101 Displacement Analysis

Translation and Rotation of Secondary Mirror

	X [in]	Y [in]	Translation RSS [in]	Rx [°]	Ry [°]	Rx [rad]	Ry [rad]	Rotation RSS [rad]
20°C to 35°C	6.567E-07	-2.517E-06	2.601E-06	-3.331E-05	-1.049E-05	-5.814E-07	-1.831E-07	6.095E-07
20°C to 5°C	-6.567E-07	2.517E-06	2.601E-06	3.331E-05	1.049E-05	5.814E-07	1.831E-07	6.095E-07
Delta 1°C	-4.378E-08	1.678E-07	1.734E-07	2.221E-06	6.993E-07	3.876E-08	1.221E-08	4.063E-08

SM translation specification is satisfied.

- 0.1734E-06 in < 0.66E-06 in

SM rotation specification is NOT satisfied.

- 0.04063E-06 rad > 0.037E-06 rad

Mechanical Engineering
University of Rochester

Figure 25. The Translation and Rotation of the SM for the Unoptimized Circular Model.

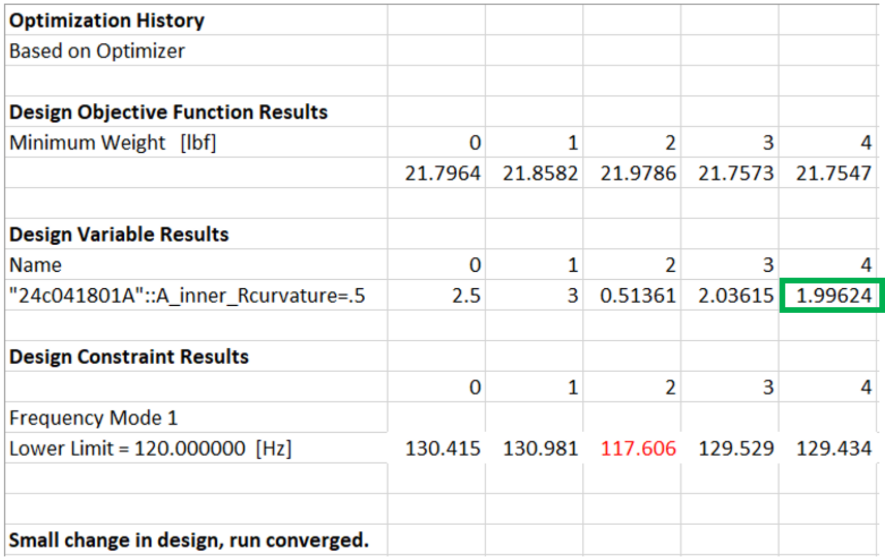

Optimization History					
Based on Optimizer					
Design Objective Function Results					
Minimum Weight [lbf]	0	1	2	3	4
	21.7964	21.8582	21.9786	21.7573	21.7547
Design Variable Results					
Name	0	1	2	3	4
"24c041801A"::A_inner_Rcurvature=.5	2.5	3	0.51361	2.03615	1.99624
Design Constraint Results					
	0	1	2	3	4
Frequency Mode 1					
Lower Limit = 120.000000 [Hz]	130.415	130.981	117.606	129.529	129.434
Small change in design, run converged.					

Figure 26: Shape Optimization of Concept 3 for the Inner Radius of Curvature for Each Leg.

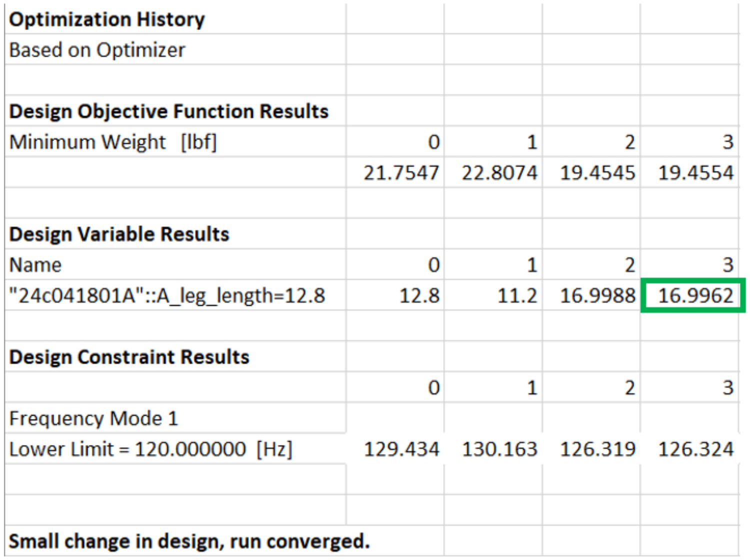

Optimization History				
Based on Optimizer				
Design Objective Function Results				
Minimum Weight [lbf]	0	1	2	3
	21.7547	22.8074	19.4545	19.4554
Design Variable Results				
Name	0	1	2	3
"24c041801A"::A_leg_length=12.8	12.8	11.2	16.9988	16.9962
Design Constraint Results				
	0	1	2	3
Frequency Mode 1				
Lower Limit = 120.000000 [Hz]	129.434	130.163	126.319	126.324
Small change in design, run converged.				

Figure 27: Shape Optimization of Concept 3 for the Length of Each Leg From the Mount Pad to the Interface of the Outer Curvature.

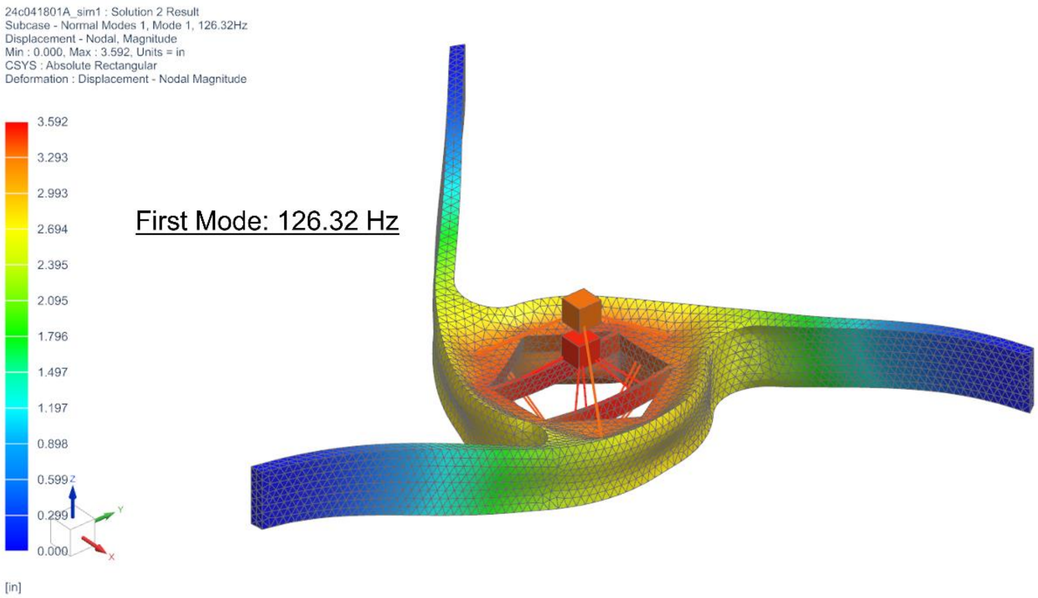

Figure 28. First Mode of Vibration for the Optimized Circular Model After the First Two Shape Optimization Runs.

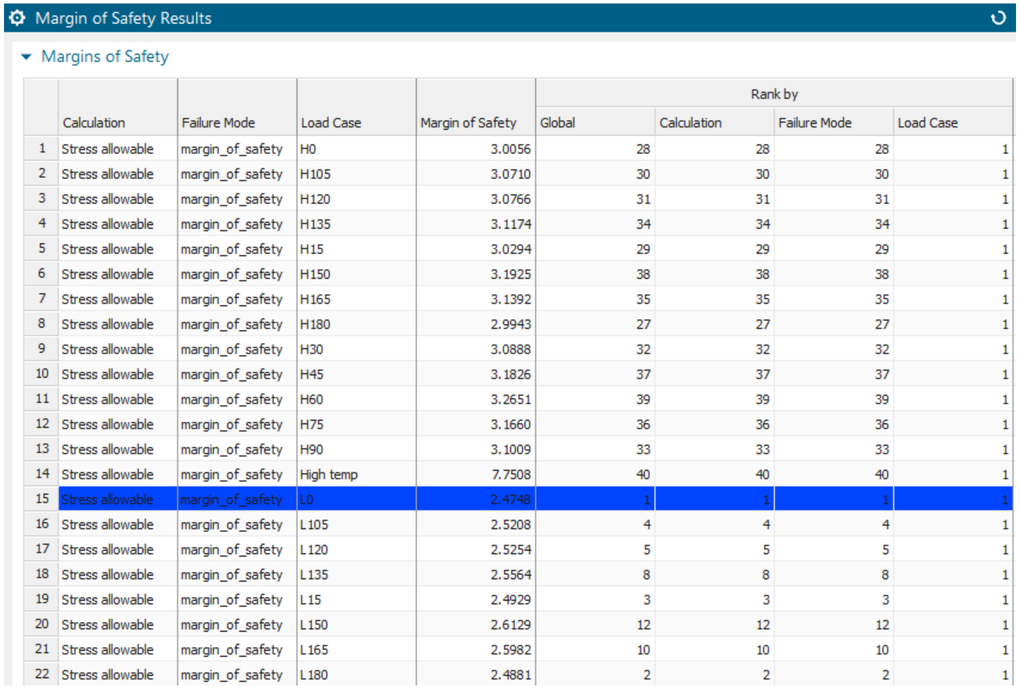

					Rank by			
	Calculation	Failure Mode	Load Case	Margin of Safety	Global	Calculation	Failure Mode	Load Case
1	Stress allowable	margin_of_safety	H0	3.0056	28	28	28	1
2	Stress allowable	margin_of_safety	H105	3.0710	30	30	30	1
3	Stress allowable	margin_of_safety	H120	3.0766	31	31	31	1
4	Stress allowable	margin_of_safety	H135	3.1174	34	34	34	1
5	Stress allowable	margin_of_safety	H15	3.0294	29	29	29	1
6	Stress allowable	margin_of_safety	H150	3.1925	38	38	38	1
7	Stress allowable	margin_of_safety	H165	3.1392	35	35	35	1
8	Stress allowable	margin_of_safety	H180	2.9943	27	27	27	1
9	Stress allowable	margin_of_safety	H30	3.0888	32	32	32	1
10	Stress allowable	margin_of_safety	H45	3.1826	37	37	37	1
11	Stress allowable	margin_of_safety	H60	3.2651	39	39	39	1
12	Stress allowable	margin_of_safety	H75	3.1660	36	36	36	1
13	Stress allowable	margin_of_safety	H90	3.1009	33	33	33	1
14	Stress allowable	margin_of_safety	High temp	7.7508	40	40	40	1
15	Stress allowable	margin_of_safety	L0	2.4748	1	1	1	1
16	Stress allowable	margin_of_safety	L105	2.5208	4	4	4	1
17	Stress allowable	margin_of_safety	L120	2.5254	5	5	5	1
18	Stress allowable	margin_of_safety	L135	2.5564	8	8	8	1
19	Stress allowable	margin_of_safety	L15	2.4929	3	3	3	1
20	Stress allowable	margin_of_safety	L150	2.6129	12	12	12	1
21	Stress allowable	margin_of_safety	L165	2.5982	10	10	10	1
22	Stress allowable	margin_of_safety	L180	2.4881	2	2	2	1

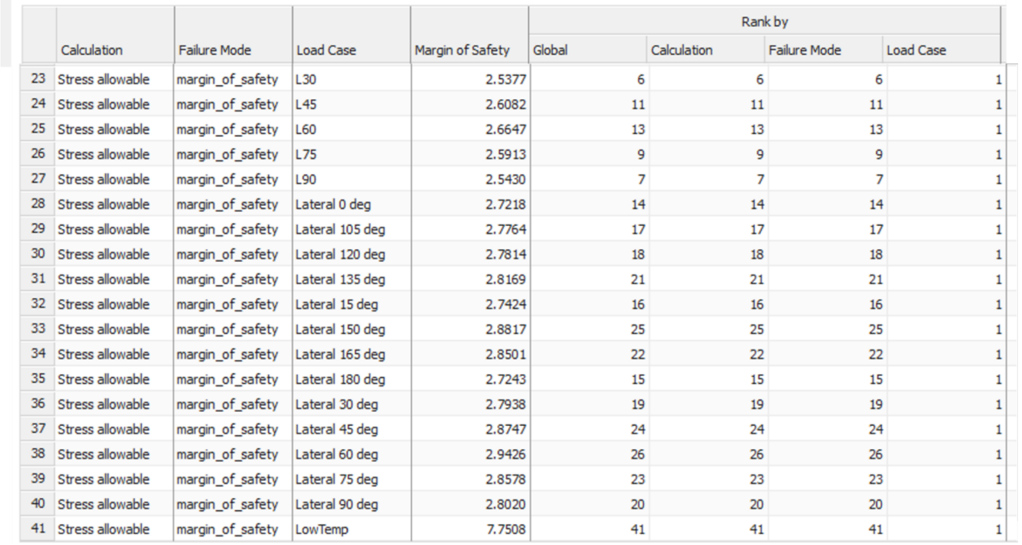

					Rank by			
	Calculation	Failure Mode	Load Case	Margin of Safety	Global	Calculation	Failure Mode	Load Case
23	Stress allowable	margin_of_safety	L30	2.5377	6	6	6	1
24	Stress allowable	margin_of_safety	L45	2.6082	11	11	11	1
25	Stress allowable	margin_of_safety	L60	2.6647	13	13	13	1
26	Stress allowable	margin_of_safety	L75	2.5913	9	9	9	1
27	Stress allowable	margin_of_safety	L90	2.5430	7	7	7	1
28	Stress allowable	margin_of_safety	Lateral 0 deg	2.7218	14	14	14	1
29	Stress allowable	margin_of_safety	Lateral 105 deg	2.7764	17	17	17	1
30	Stress allowable	margin_of_safety	Lateral 120 deg	2.7814	18	18	18	1
31	Stress allowable	margin_of_safety	Lateral 135 deg	2.8169	21	21	21	1
32	Stress allowable	margin_of_safety	Lateral 15 deg	2.7424	16	16	16	1
33	Stress allowable	margin_of_safety	Lateral 150 deg	2.8817	25	25	25	1
34	Stress allowable	margin_of_safety	Lateral 165 deg	2.8501	22	22	22	1
35	Stress allowable	margin_of_safety	Lateral 180 deg	2.7243	15	15	15	1
36	Stress allowable	margin_of_safety	Lateral 30 deg	2.7938	19	19	19	1
37	Stress allowable	margin_of_safety	Lateral 45 deg	2.8747	24	24	24	1
38	Stress allowable	margin_of_safety	Lateral 60 deg	2.9426	26	26	26	1
39	Stress allowable	margin_of_safety	Lateral 75 deg	2.8578	23	23	23	1
40	Stress allowable	margin_of_safety	Lateral 90 deg	2.8020	20	20	20	1
41	Stress allowable	margin_of_safety	LowTemp	7.7508	41	41	41	1

Figure 29. Margin of Safety Calculations for all Load Combined Load Cases on the Optimized Circular Model. The 18G Axial Load, 12G Lateral Load at 0°, and the 20°C to 5°C Temperature Change was Calculated to be the Worst-Case Loading While Maintaining a Positive Margin at 2.4748.

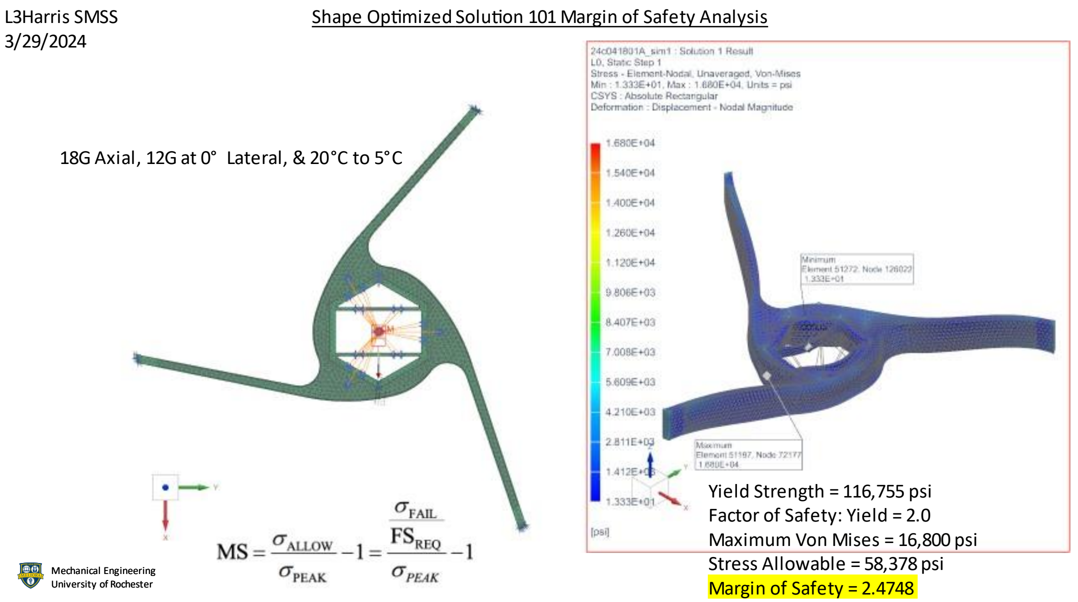

L3Harris SMSS
3/29/2024

Shape Optimized Solution 101 Margin of Safety Analysis

18G Axial, 12G at 0° Lateral, & 20°C to 5°C

24c041801A_sim1 : Solution 1 Result
LD, Static Step 1
Stress - Element-Nodal, Unaveraged, Von-Mises
Min : 1.333E+01, Max : 1.680E+04, Units = psi
CSYS : Absolute Rectangular
Deformation : Displacement - Nodal Magnitude

$$MS = \frac{\sigma_{ALLOW}}{\sigma_{PEAK}} - 1 = \frac{\frac{\sigma_{FAIL}}{FS_{REQ}}}{\sigma_{PEAK}} - 1$$

Yield Strength = 116,755 psi
Factor of Safety: Yield = 2.0
Maximum Von Mises = 16,800 psi
Stress Allowable = 58,378 psi
Margin of Safety = 2.4748

Mechanical Engineering
University of Rochester

Figure 30. The Stress Plot for the Worst-Case Load on the Optimized Circular Model with a Margin Calculation Confirming the NX Calculation.

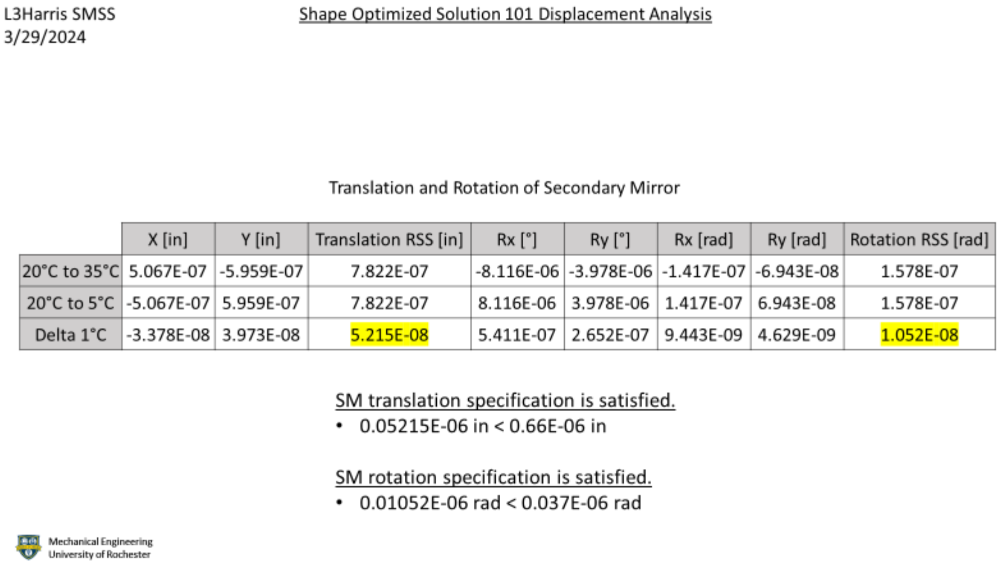

L3Harris SMSS
3/29/2024

Shape Optimized Solution 101 Displacement Analysis

Translation and Rotation of Secondary Mirror

	X [in]	Y [in]	Translation RSS [in]	Rx [°]	Ry [°]	Rx [rad]	Ry [rad]	Rotation RSS [rad]
20°C to 35°C	5.067E-07	-5.959E-07	7.822E-07	-8.116E-06	-3.978E-06	-1.417E-07	-6.943E-08	1.578E-07
20°C to 5°C	-5.067E-07	5.959E-07	7.822E-07	8.116E-06	3.978E-06	1.417E-07	6.943E-08	1.578E-07
Delta 1°C	-3.378E-08	3.973E-08	5.215E-08	5.411E-07	2.652E-07	9.443E-09	4.629E-09	1.052E-08

SM translation specification is satisfied.

- 0.05215E-06 in < 0.66E-06 in

SM rotation specification is satisfied.

- 0.01052E-06 rad < 0.037E-06 rad

Mechanical Engineering
University of Rochester

Figure 31. The Translation and Rotation of the SM for the Optimized Circular Model after the First Two Shape Optimization Runs.

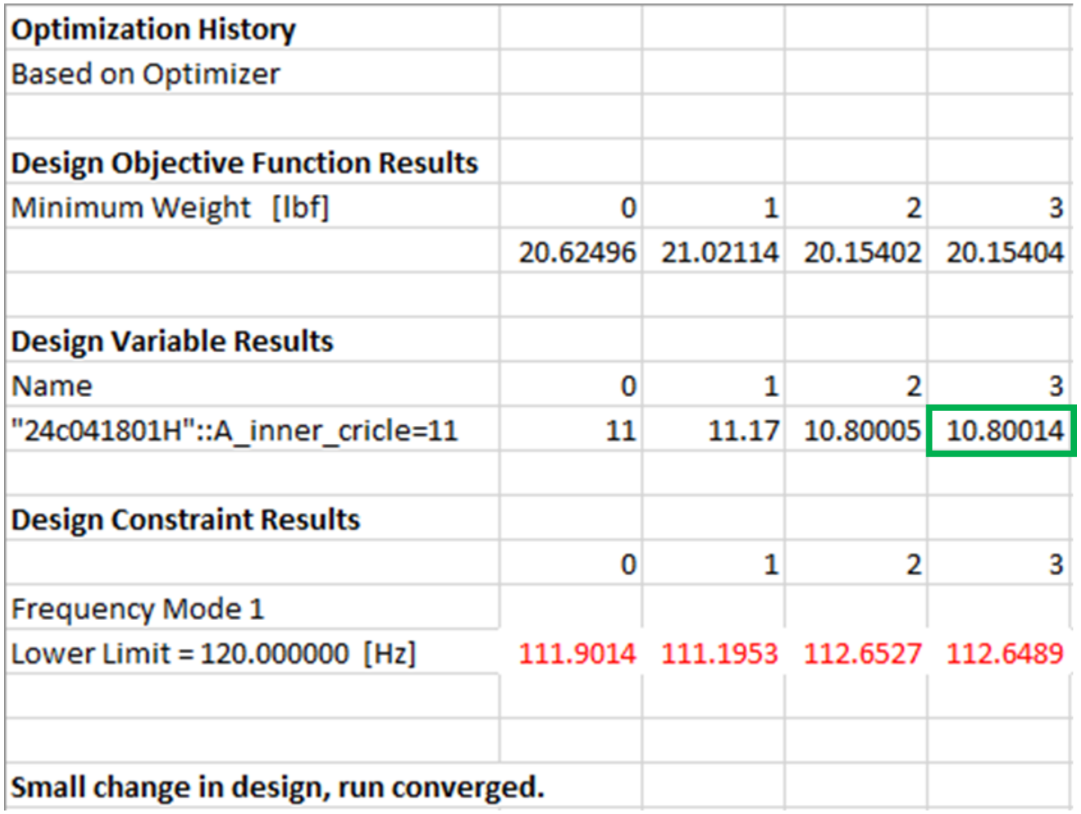

Optimization History				
Based on Optimizer				
Design Objective Function Results				
Minimum Weight [lbf]	0	1	2	3
	20.62496	21.02114	20.15402	20.15404
Design Variable Results				
Name	0	1	2	3
"24c041801H"::A_inner_cricle=11	11	11.17	10.80005	10.80014
Design Constraint Results				
	0	1	2	3
Frequency Mode 1				
Lower Limit = 120.000000 [Hz]	111.9014	111.1953	112.6527	112.6489
Small change in design, run converged.				

Figure 32. Shape Optimization for the Printable Model with a Circular Cut Out Instead of a Hexagonal Cut Out.

APPENDIX C

MANUFACTURING & TESTING

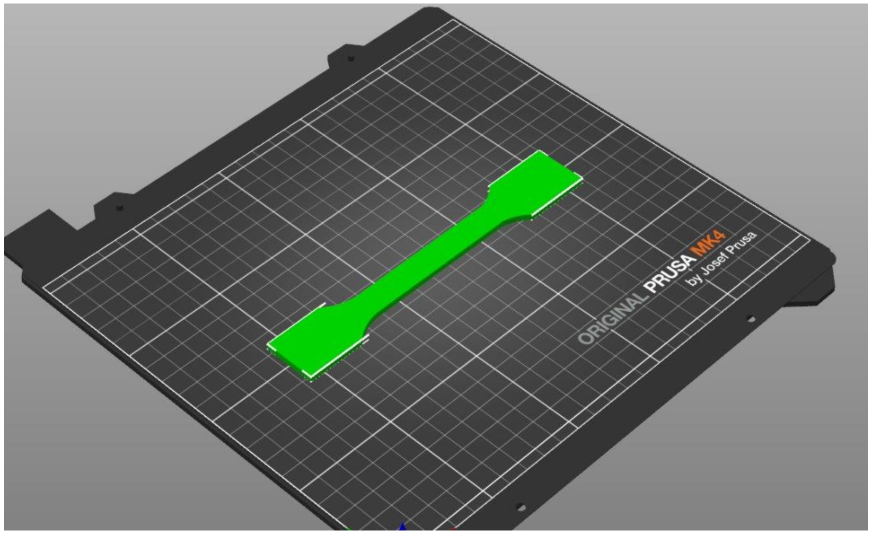

Figure 1. Slice of Coupon Sample Printed Horizontally.

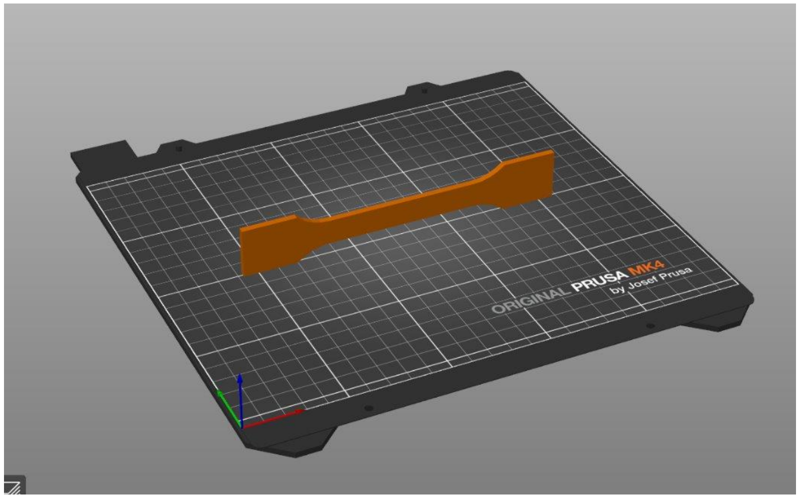

Figure 2. Slice of Coupon Sample Printed Vertically.

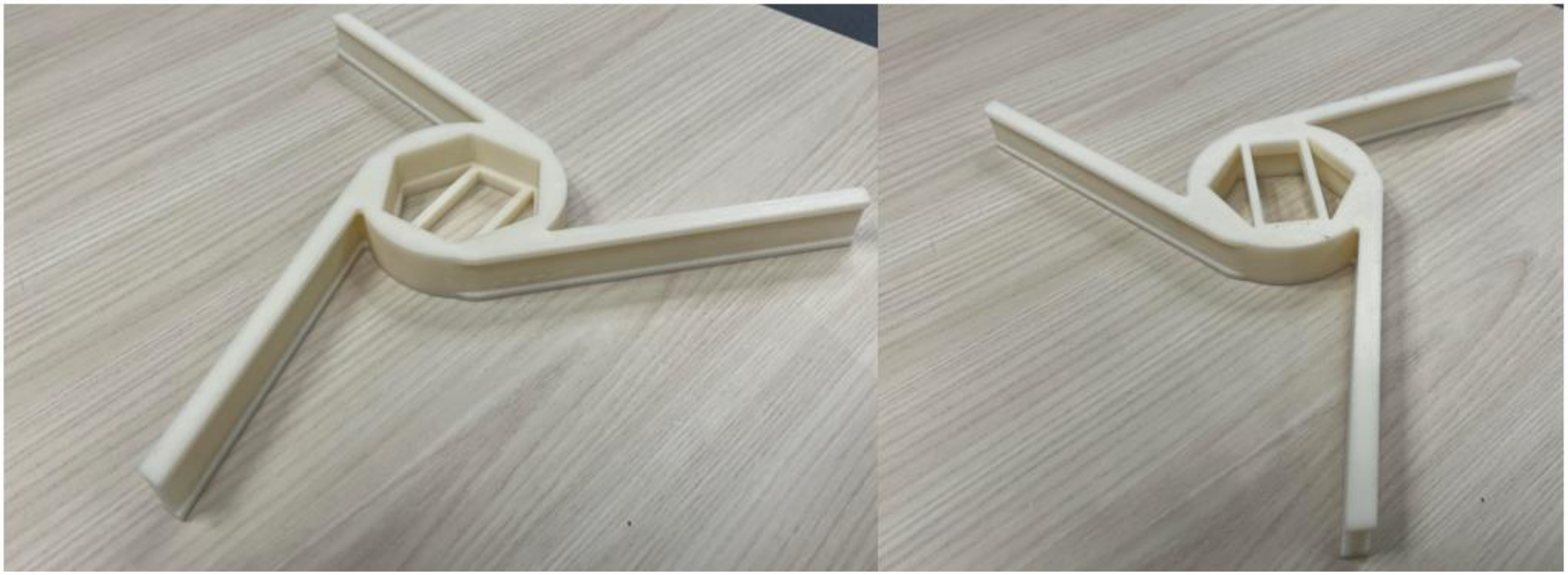

Figure 3. Print of 20% Scaled Model of Concept 5.

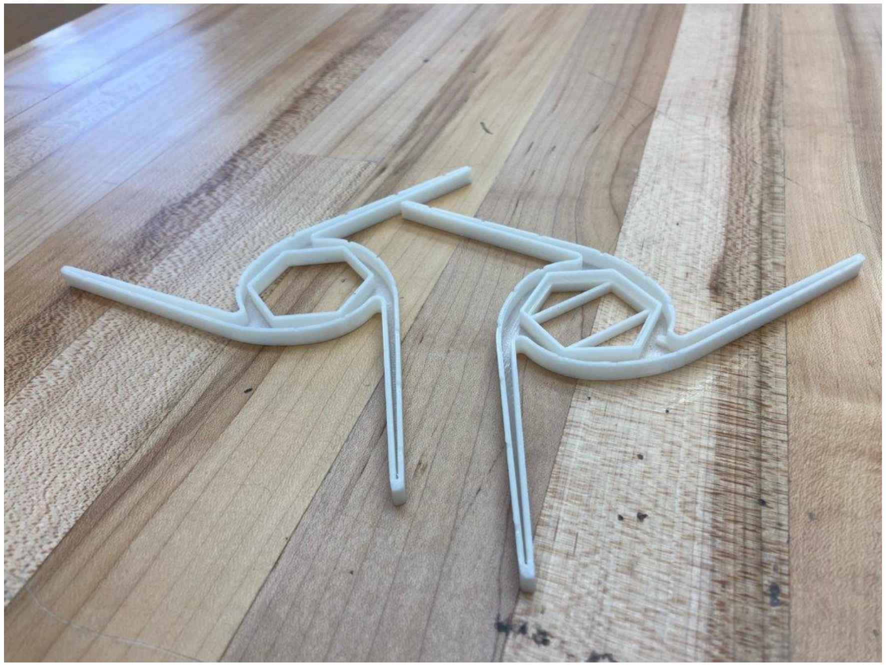

Figure 4. Print of 5% Scaled Model of Concept 3 Printed in Halves.

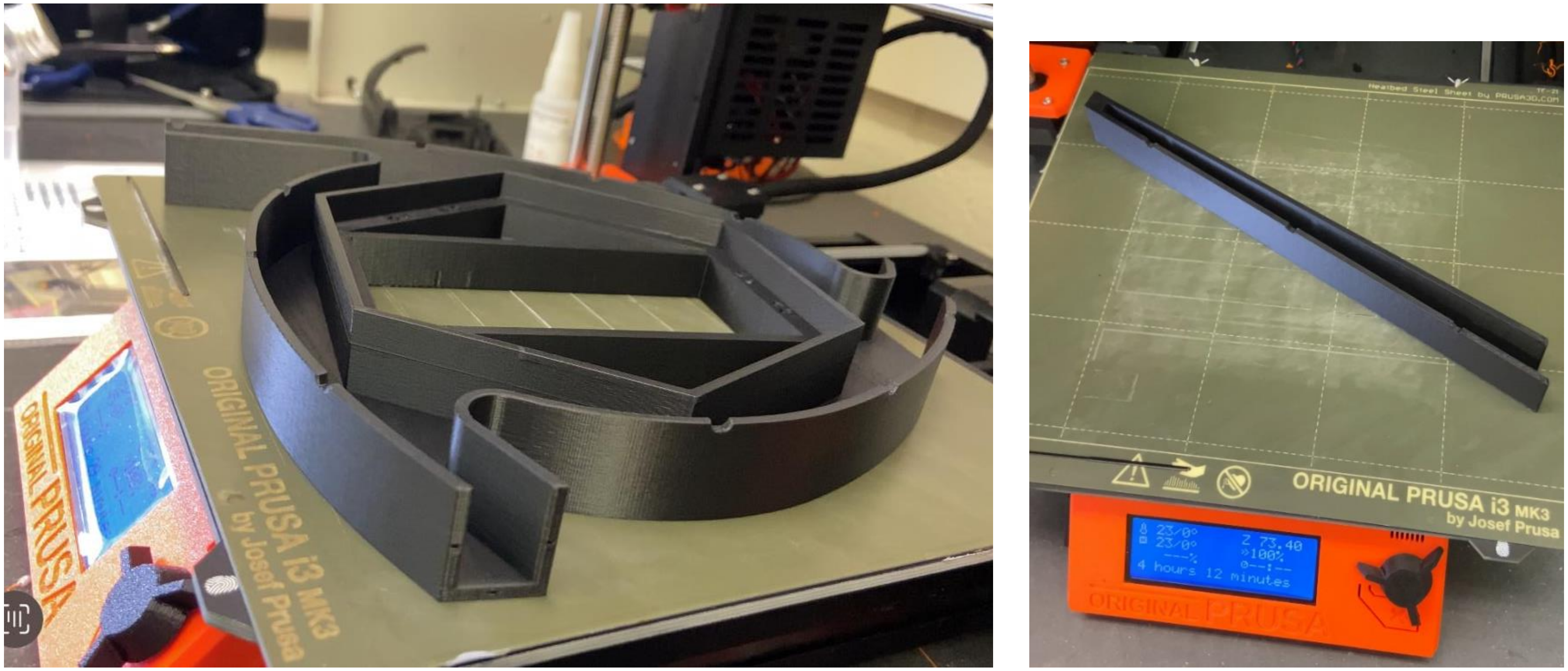

Figure 5. Sections of 55% Scaled Model of Concept 3 to Test In-House Printing.

Figure 6. Proof of Concept Overhang Angle Printing.

Figure 7. Print of 10% Scale Model for Proof of Overhang Angle Concept in Full Model.

Figure 8. 60% Scaled 3D Printed ASA Model from Xometry.

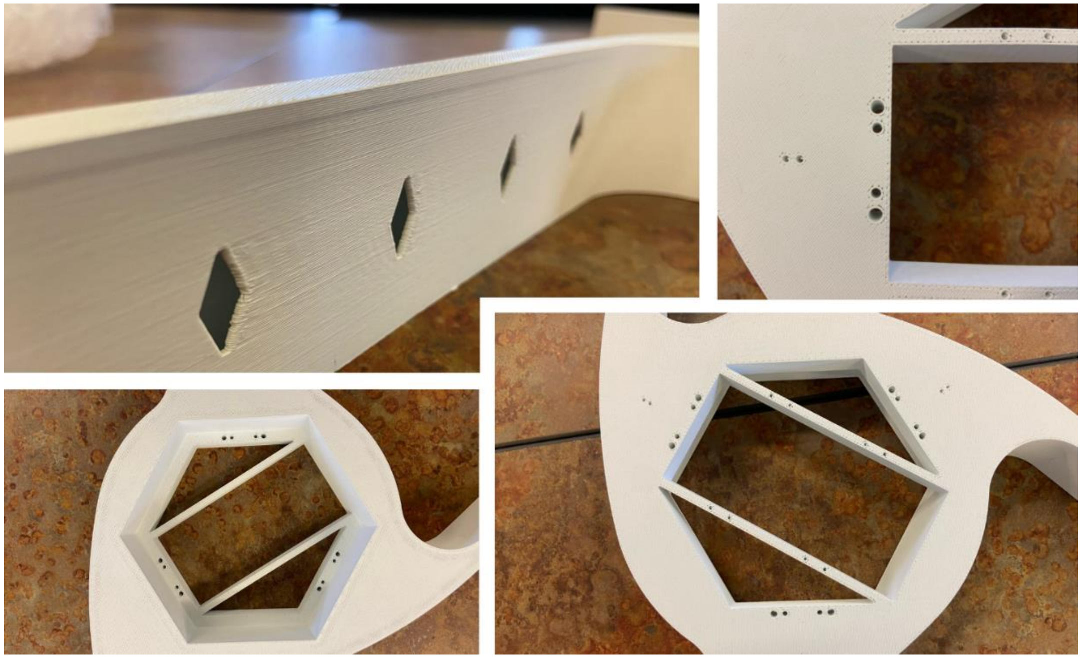

Figure 9. Closer View of Xometry 3D Printed ASA Model Showing All Mounting and Vent Holes.

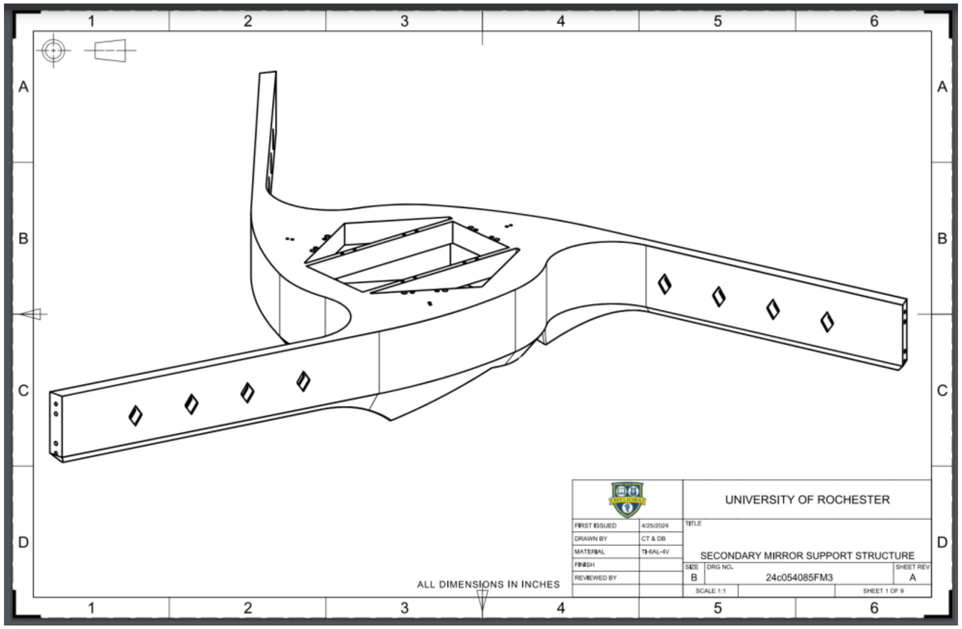

Figure 10: Trimetric View of Final Design

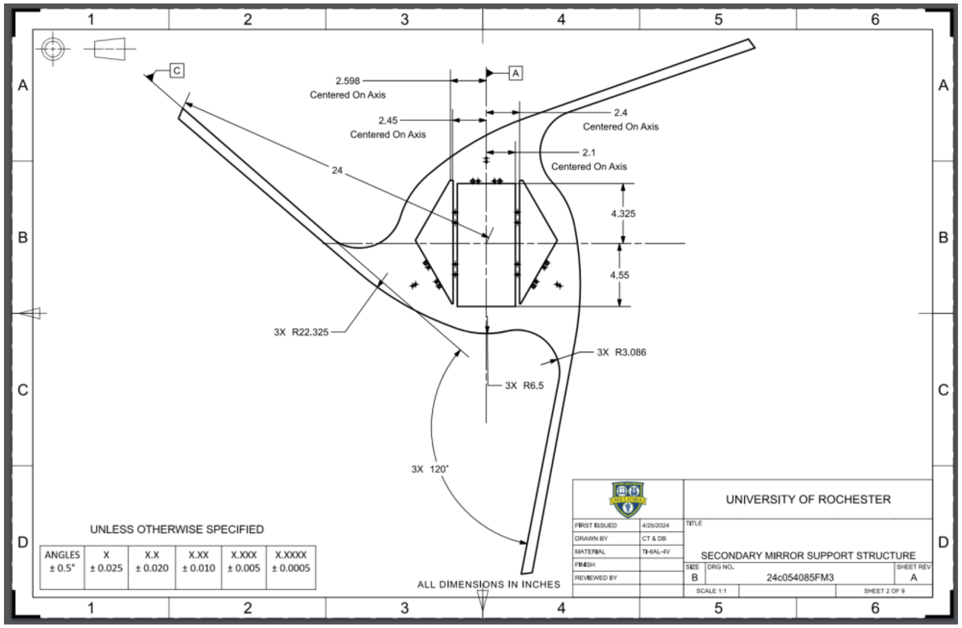

Figure 11: Top View Drawing with Large Geometry Dimensions

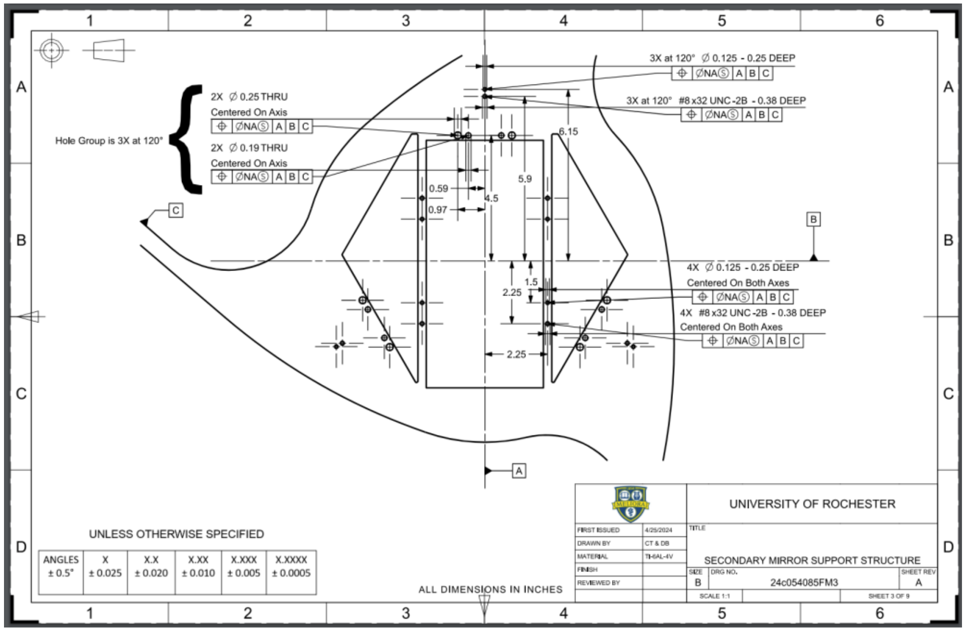

Figure 12: Top View Drawing with Mounting Hole Details.

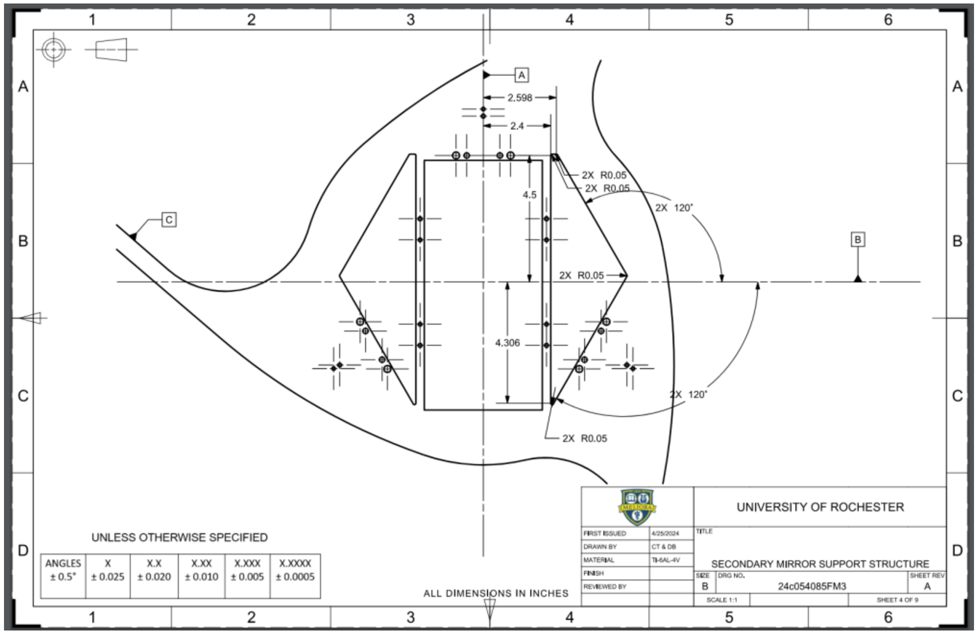

Figure 13: Top View Drawing with Triangular Cutout Dimensions.

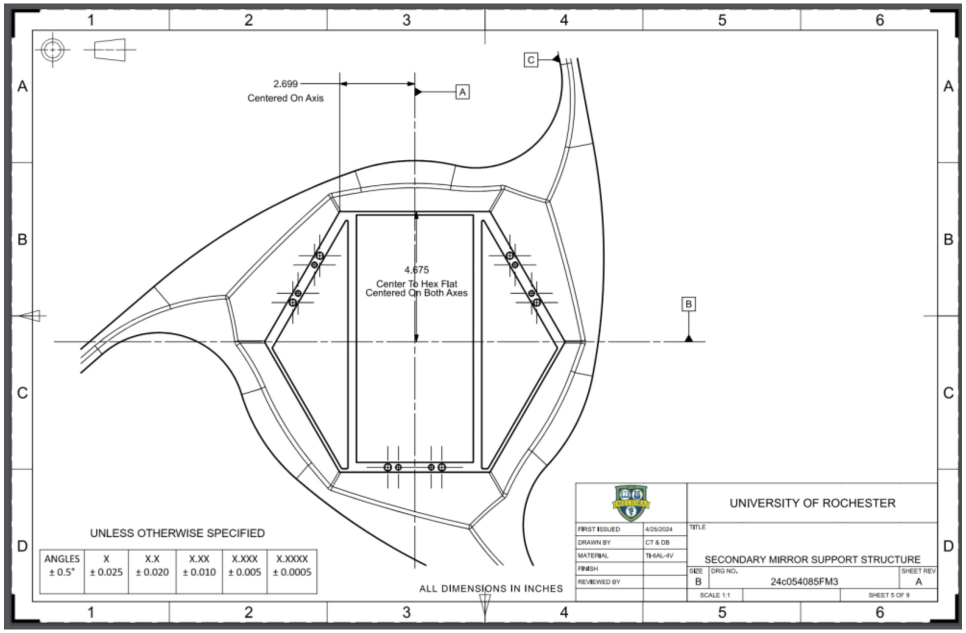

Figure 14: Bottom View Drawing with Inner Hex Dimensions.

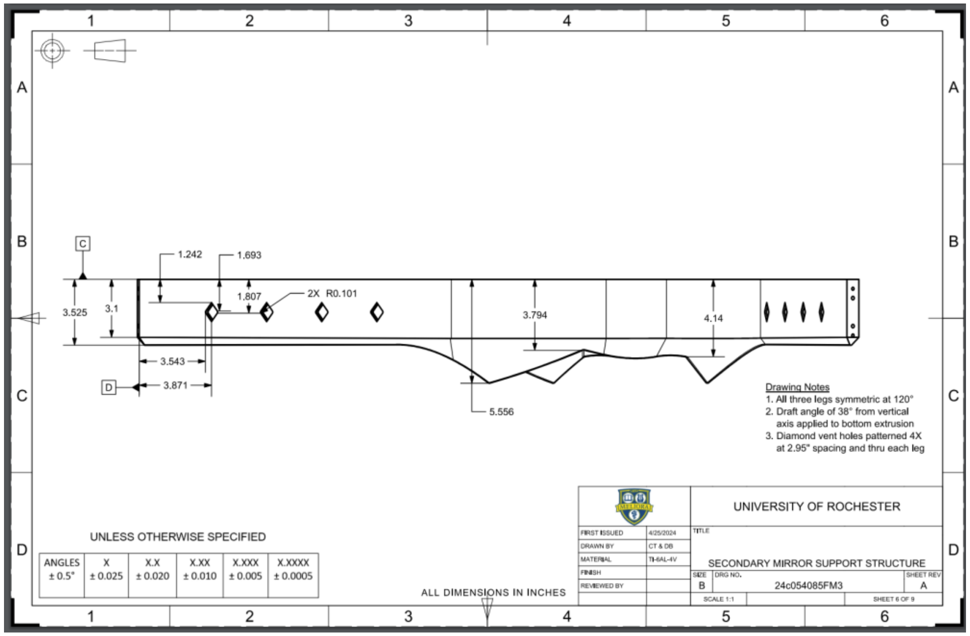

Drawing Notes

1. All three legs symmetric at 120°
2. Draft angle of 38° from vertical axis applied to bottom extrusion
3. Diamond vent holes patterned 4X at 2.95" spacing and thru each leg

Figure 15: Side View Drawing with Vent Holes and Draft Angle Dimensions.

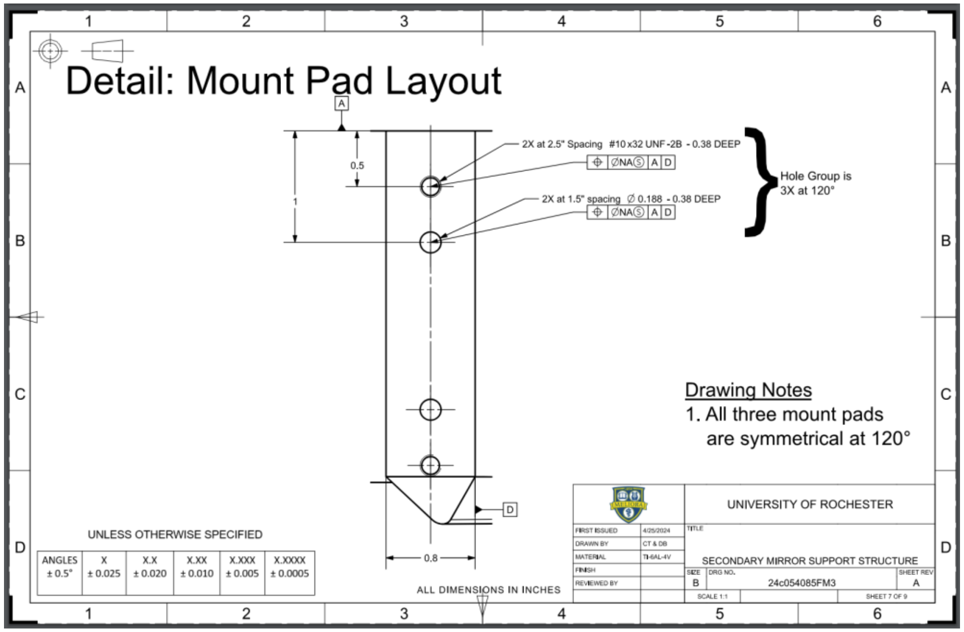

Figure 16: Mount Pad Detail Drawing.

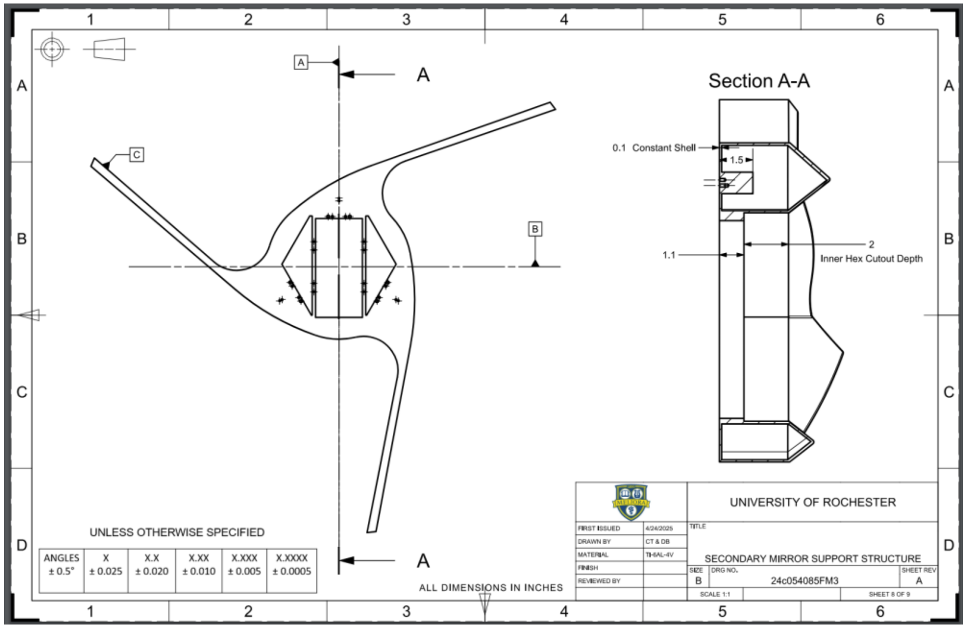

Figure 17: Section View Drawing for Shell Dimensions and Details.

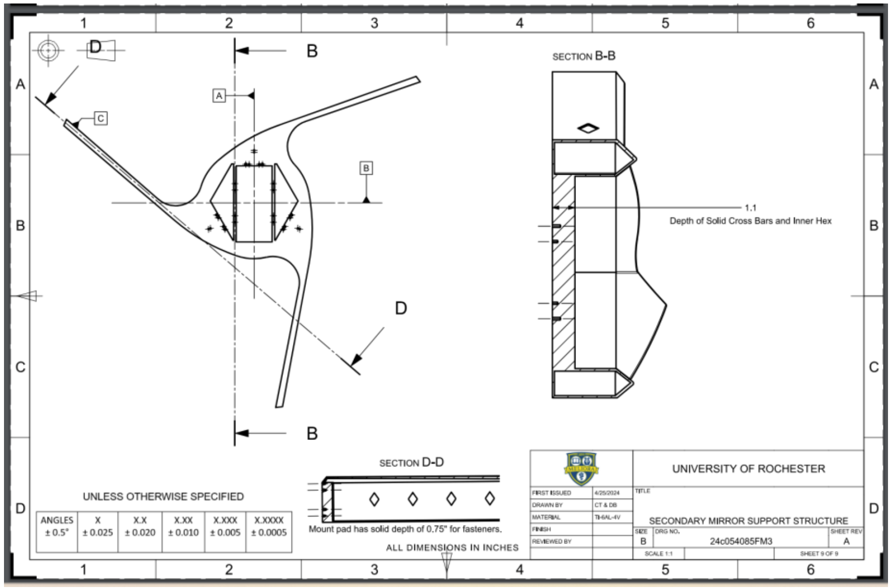

Figure 18: Section View Drawing for Solid Hex and Mount Pad Face Dimensions.

Figure 19. Group 1 Aluminum Coupons (5 Total in Group).

Figure 20. Group 2 Steel Coupons (6 total in Group).

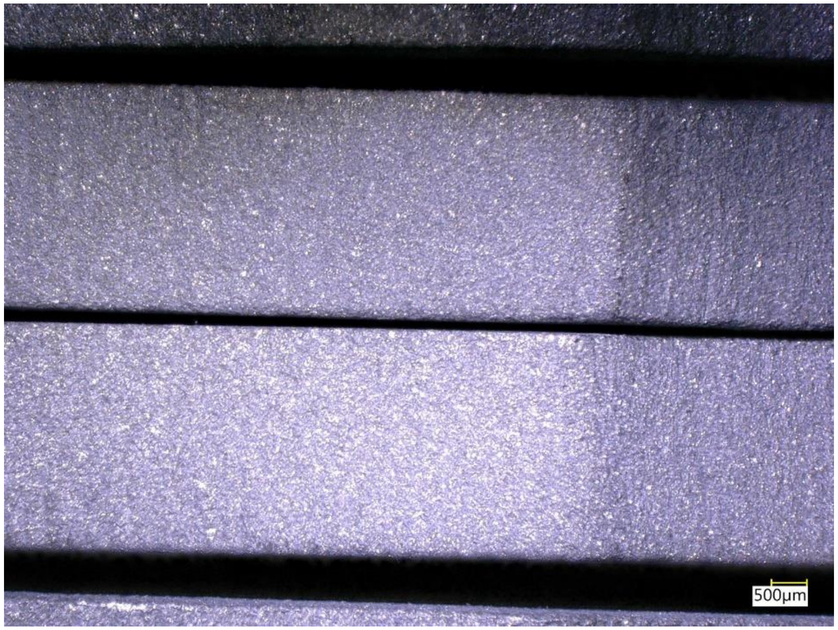

Figure 21. Group 3 Aluminum Coupons (4 total in Group).

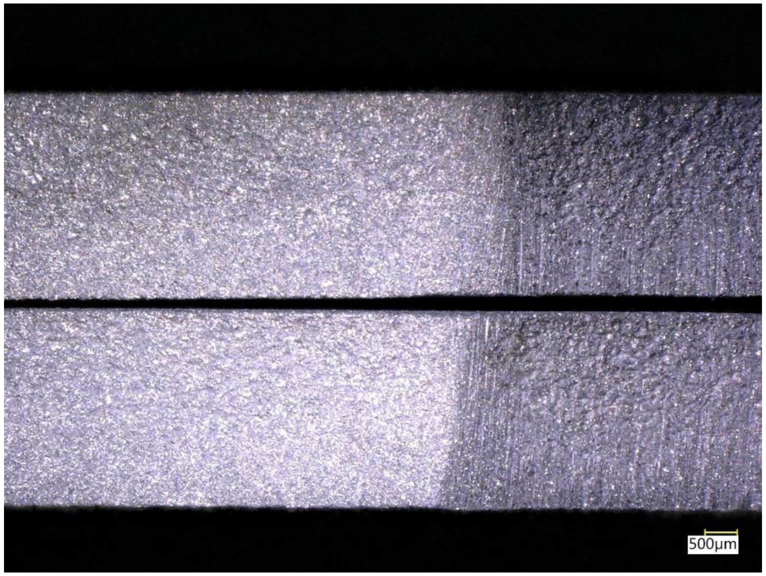

Figure 22. Group 3 Steel Coupons (2 total in Group). The Sandblasted Finish can be Faintly Seen on Both Coupons.

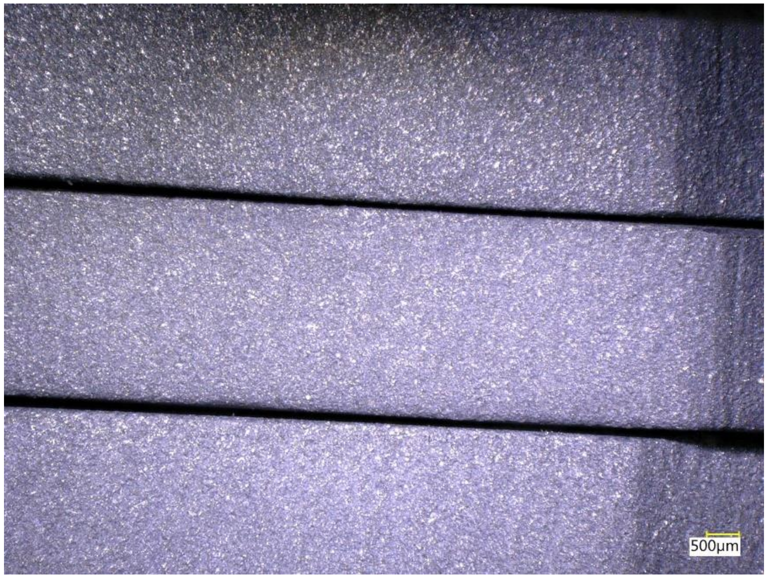

Figure 23. Group 4 Aluminum Coupons (3 Total in Group).

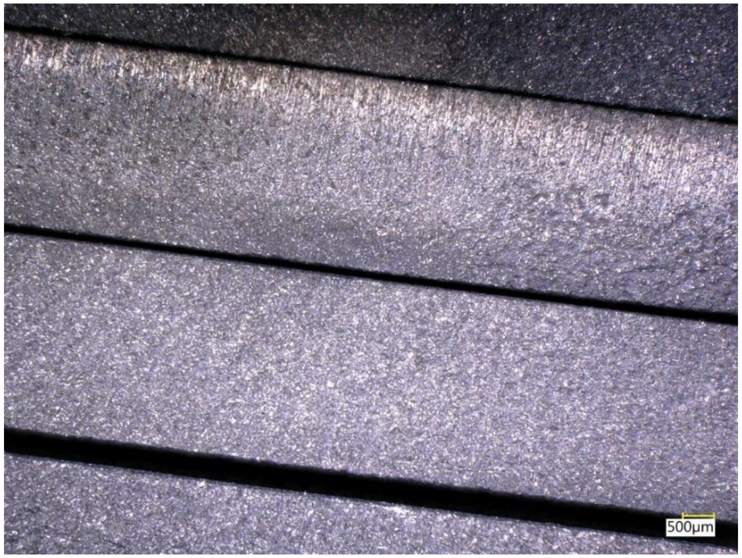

Figure 24. Group 4 Steel Coupons (4 total in Group). The Sandblasted Finish can be Faintly Seen on the Second Coupon From the Top.

Figure 25. 3D Printed Coupon Gage Width Measurement with Micrometer on an Aluminum Coupon.

Figure 26. 3D Printed Coupon Gage Thickness Measurement with Micrometer on a Steel Coupon.

Figure 27. 3D Printed Coupon Flatness Measurement.

TABLE 1
3D PRINTED ALUMINUM COUPON MEASUREMENTS AND CALCULATIONS.

3D Printed Aluminum Coupons (AlSi10Mg)							
Coupon	**Gage Width (in)**	**Gage Thickness (in)**	**Cross Sectional Area (in^2)**	**Flatness Peak to Valley (in)**	**Mass (g)**	**Volume (mL)**	**Density (lb/in^3)**
G1 Al1	0.498	0.130	0.0647	0.018	25.36	10.0	0.0916
G1 Al2	0.497	0.129	0.0641	0.016	24.92	9.0	0.1000
G1 Al3	0.501	0.130	0.0651	0.018	25.38	9.5	0.0965
G1 Al4	0.499	0.129	0.0644	0.018	25.33	9.5	0.0963
G1 Al5	0.499	0.126	0.0629	0.018	24.55	9.5	0.0934
G3 Al1	0.499	0.129	0.0644	0.022	25.30	9.5	0.0962
G3 Al2	0.498	0.129	0.0642	0.015	25.42	9.5	0.0967
G3 Al3	0.498	0.129	0.0642	0.019	25.38	10.0	0.0917
G3 Al4	0.498	0.129	0.0642	0.018	25.25	9.5	0.0960
G4 Al1	0.499	0.127	0.0634	0.018	25.06	9.5	0.0953
G4 Al2	0.499	0.128	0.0639	0.017	25.16	9.0	0.1010
G4 Al3	0.498	0.132	0.0657	0.020	25.50	9.5	0.0970
Average	0.4986	0.1289	0.06428	0.0181	25.218	9.50	0.09598
Standard Deviation	0.0010	0.0015	0.00074	0.0018	0.266	0.30	0.00283
Coefficient of Variation	0.0020	0.0117	0.0116	0.0985	0.0105	0.0317	0.0295
Minimum	0.497	0.126	0.0629	0.015	24.55	9.0	0.0916
Maximum	0.501	0.132	0.0657	0.022	25.50	10.0	0.1010

TABLE 2
3D PRINTED STEEL COUPON MEASUREMENTS AND CALCULATIONS.

3D Printed Steel Coupons (316L Stainless Steel)							
Coupon	**Gage Width (in)**	**Gage Thickness (in)**	**Cross Sectional Area (in^2)**	**Flatness Peak to Valley (in)**	**Mass (g)**	**Volume (mL)**	**Density (lb/in^3)**
G2 S1	0.497	0.122	0.0606	0.031	70.48	10.0	0.2546
G2 S2	0.497	0.125	0.0621	0.033	73.37	9.0	0.2945
G2 S3	0.496	0.124	0.0615	0.029	72.91	9.0	0.2927
G2 S4	0.497	0.124	0.0616	0.031	71.84	8.0	0.3244
G2 S5	0.497	0.121	0.0601	0.029	71.25	8.0	0.3218
G2 S6	0.497	0.123	0.0611	0.037	70.30	8.0	0.3175
G3 S1	0.496	0.126	0.0625	0.037	71.91	9.0	0.2887
G3 S2	0.497	0.124	0.0616	0.025	72.31	9.0	0.2903
G4 S1	0.496	0.121	0.0600	0.031	70.54	8.5	0.2998
G4 S2	0.496	0.121	0.0600	0.036	70.50	9.0	0.2830
G4 S3	0.496	0.123	0.0610	0.031	71.90	9.0	0.2886
G4 S4	0.496	0.121	0.0600	0.033	71.05	9.0	0.2852
Average	0.4965	0.1229	0.06103	0.0319	71.530	8.79	0.29508
Standard Deviation	0.0005	0.0017	0.00087	0.0036	1.011	0.58	0.01928
Coefficient of Variation	0.0011	0.0141	0.0143	0.1113	0.0141	0.0662	0.0653
Minimum	0.496	0.121	0.0600	0.025	70.30	8.0	0.2546
Maximum	0.497	0.126	0.0625	0.037	73.37	10.0	0.3244

Figure 28. Thermal Cycling Setup. The Group 2 Steel Coupons are Pictured Prior to the Start of the First Thermal Cycle.

Figure 29. Rockwell Hardness Test Setup With one of the 3D Printed Steel Coupons.

Figure 30. Rockwell Hardness Test Screen Setup for the Scale B 1/16-Inch Steel Ball Indenter With an Applied Force of 100 kg.

TABLE 3
ROCKWELL HARDNESS TEST DATA FOR ALUMINUM COUPONS.

3D Printed Aluminum Coupons (AlSi10Mg)							
Coupon	**Rockwell Hardness Number (Test 1)**	**Rockwell Hardness Number (Test 2)**	**Rockwell Hardness Number (Test 3)**	**Rockwell Hardness Number (Test 4)**	**Rockwell Hardness Number (Test 5)**	**Rockwell Hardness Number (Average)**	**Rockwell Hardness Number (STD)**
G1 Al1	67.6	68.3	70.2	70.5	70.8	69.48	1.434
G1 Al2	67.5	70.9	71.0	68.8	68.3	69.30	1.576
G1 Al3	67.7	69.5	69.4	69.2	72.1	69.58	1.587
G1 Al4	67.1	70.4	69.3	68.2	70.3	69.06	1.412
G1 Al5	67.3	68.1	67.6	69.0	66.1	67.62	1.066
G3 Al1	67.0	67.7	68.6	67.3	69.2	67.96	0.918
G3 Al2	69.4	69.0	67.4	69.6	70.7	69.22	1.197
G3 Al3	69.0	69.3	70.4	69.3	68.8	69.36	0.619
G3 Al4	70.1	70.2	71.2	70.1	69.3	70.18	0.676
G4 Al1	68.5	69.2	69.2	69.8	69.8	69.30	0.539
G4 Al2	69.4	69.2	72.1	70.7	71.0	70.48	1.199
G4 Al3	69.0	70.7	70.5	71.9	68.8	70.18	1.287

Average	69.310
Standard Deviation	0.839
Coefficient of Variation	0.0121
Minimum	67.62
Maximum	70.48

TABLE 4
ROCKWELL HARDNESS TEST DATA FOR STEEL COUPONS.

3D Printed Steel Coupons (316L Stainless Steel)							
Coupon	**Rockwell Hardness Number (Test 1)**	**Rockwell Hardness Number (Test 2)**	**Rockwell Hardness Number (Test 3)**	**Rockwell Hardness Number (Test 4)**	**Rockwell Hardness Number (Test 5)**	**Rockwell Hardness Number (Average)**	**Rockwell Hardness Number (STD)**
G2 S1	97.3	95.4	91.2	93.5	94.0	94.28	2.266
G2 S2	95.5	96.5	95.8	97.5	98.3	96.72	1.171
G2 S3	96.7	98.0	97.2	96.8	96.7	97.08	0.554
G2 S4	94.4	93.5	94.6	95.4	93.3	94.24	0.856
G2 S5	95.8	97.1	98.1	97.0	96.0	96.80	0.930
G2 S6	88.8	86.2	88.2	91.0	89.5	88.74	1.763
G3 S1	95.5	96.6	96.2	95.9	95.3	95.90	0.524
G3 S2	97.8	98.6	97.9	97.6	96.9	97.76	0.611
G4 S1	95.4	94.7	93.7	94.1	92.6	94.10	1.056
G4 S2	92.8	93.1	92.8	95.2	95.8	93.94	1.445
G4 S3	94.0	94.9	95.7	92.3	96.0	94.58	1.492
G4 S4	96.6	96.9	96.8	97.9	96.4	96.92	0.581
					Average	95.088	
					Standard Deviation	2.430	
					Coefficient of Variation	0.0256	
					Minimum	88.74	
					Maximum	97.76	

Figure 31. The 3-point Bend Test Setup on the MTS Machine With a 3D Printed Steel Coupon.

Figure 32. Tensile Test Setup on the MTS Machine With a 3D printed Steel Coupon in the Grippers.

TABLE 5
MATERIAL PROPERTIES FOR INDIVIDUAL 3D PRINTED ALUMINUM COUPONS AND THE STATISTICS OF THE MATERIAL PROPERTIES.

3D Printed Aluminum Coupons (AlSi10Mg)				
Coupon	**Elastic Modulus (psi)**	**Yield Strength (psi)**	**Ultimate Stress (psi)**	**Flexural Modulus (psi)**
G1 Al1	9.985E+06	3.801E+04	5.640E+04	2.551E+06
G1 Al2	9.400E+06	3.739E+04	5.376E+04	2.531E+06
G1 Al3	8.805E+06	3.854E+04	5.659E+04	2.516E+06
G1 Al4	8.066E+06	3.894E+04	5.595E+04	2.629E+06
G1 Al5	8.083E+06	3.735E+04	5.375E+04	2.536E+06
G3 Al1	1.006E+07	3.681E+04	5.536E+04	2.851E+06
G3 Al2	1.014E+07	3.660E+04	5.602E+04	3.003E+06
G3 Al3	9.252E+06	3.795E+04	5.605E+04	3.105E+06
G3 Al4	9.976E+06	3.757E+04	5.540E+04	3.041E+06
G4 Al1	9.933E+06	3.710E+04	5.405E+04	2.920E+06
G4 Al2	9.901E+06	3.720E+04	5.519E+04	2.585E+06
G4 Al3	9.934E+06	3.824E+04	5.555E+04	2.681E+06
Average	9.461E+06	3.764E+04	5.534E+04	2.746E+06
Standard Deviation	7.581E+05	7.087E+02	9.889E+02	2.232E+05
Coefficient of Variation	0.0801	0.0188	0.0179	0.0813
Minimum	8.066E+06	3.660E+04	5.375E+04	2.516E+06
Maximum	1.014E+07	3.894E+04	5.659E+04	3.105E+06
Craftcloud Expected Minimum	1.015E+07	-	4.815E+04	-
Craftcloud Expected Maximum	1.102E+07	-	6.962E+04	-

TABLE 6
MATERIAL PROPERTIES FOR INDIVIDUAL 3D PRINTED STEEL COUPONS AND THE STATISTICS OF THE MATERIAL PROPERTIES.

3D Printed Steel Coupons (316L Stainless Steel)				
Coupon	**Elastic Modulus (psi)**	**Yield Strength (psi)**	**Ultimate Stress (psi)**	**Flexural Modulus (psi)**
G2 S2	2.715E+07	7.921E+04	9.861E+04	4.587E+06
G2 S3	2.483E+07	7.804E+04	9.709E+04	4.321E+06
G2 S4	2.365E+07	7.314E+04	9.196E+04	4.062E+06
G2 S5	2.848E+07	7.577E+04	9.482E+04	4.109E+06
G2 S6	2.420E+07	6.814E+04	8.688E+04	4.622E+06
G3 S1	2.425E+07	7.476E+04	9.349E+04	4.907E+06
G3 S2	2.649E+07	7.682E+04	9.574E+04	4.879E+06
G4 S1	2.504E+07	7.492E+04	9.345E+04	4.945E+06
G4 S2	2.467E+07	7.369E+04	9.193E+04	5.415E+06
G4 S3	2.618E+07	7.599E+04	9.475E+04	5.065E+06
G4 S4	2.470E+07	7.708E+04	9.542E+04	3.867E+06
Average	2.542E+07	7.523E+04	9.401E+04	4.616E+06
Standard Deviation	1.472E+06	2.964E+03	3.111E+03	4.812E+05
Coefficient of Variation	0.0579	0.0394	0.0331	0.1042
Minimum	2.365E+07	6.814E+04	8.688E+04	3.867E+06
Maximum	2.848E+07	7.921E+04	9.861E+04	5.415E+06
Craftcloud Expected Minimum	2.611E+07	-	8.557E+04	-
Craftcloud Expected Maximum	2.683E+07	-	1.015E+05	-

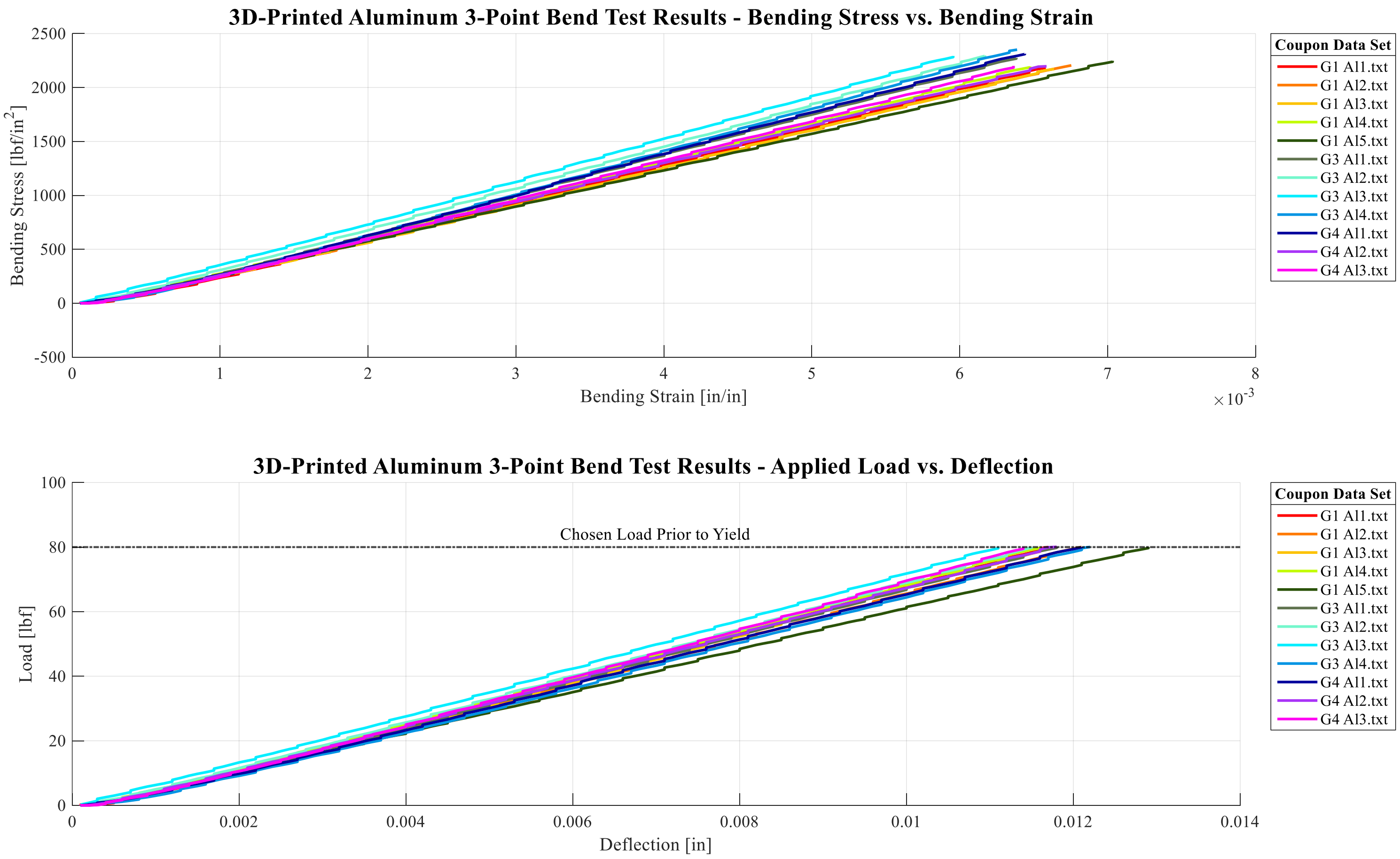

Figure 33. Aluminum Coupon 3-point Bending Test Plots.

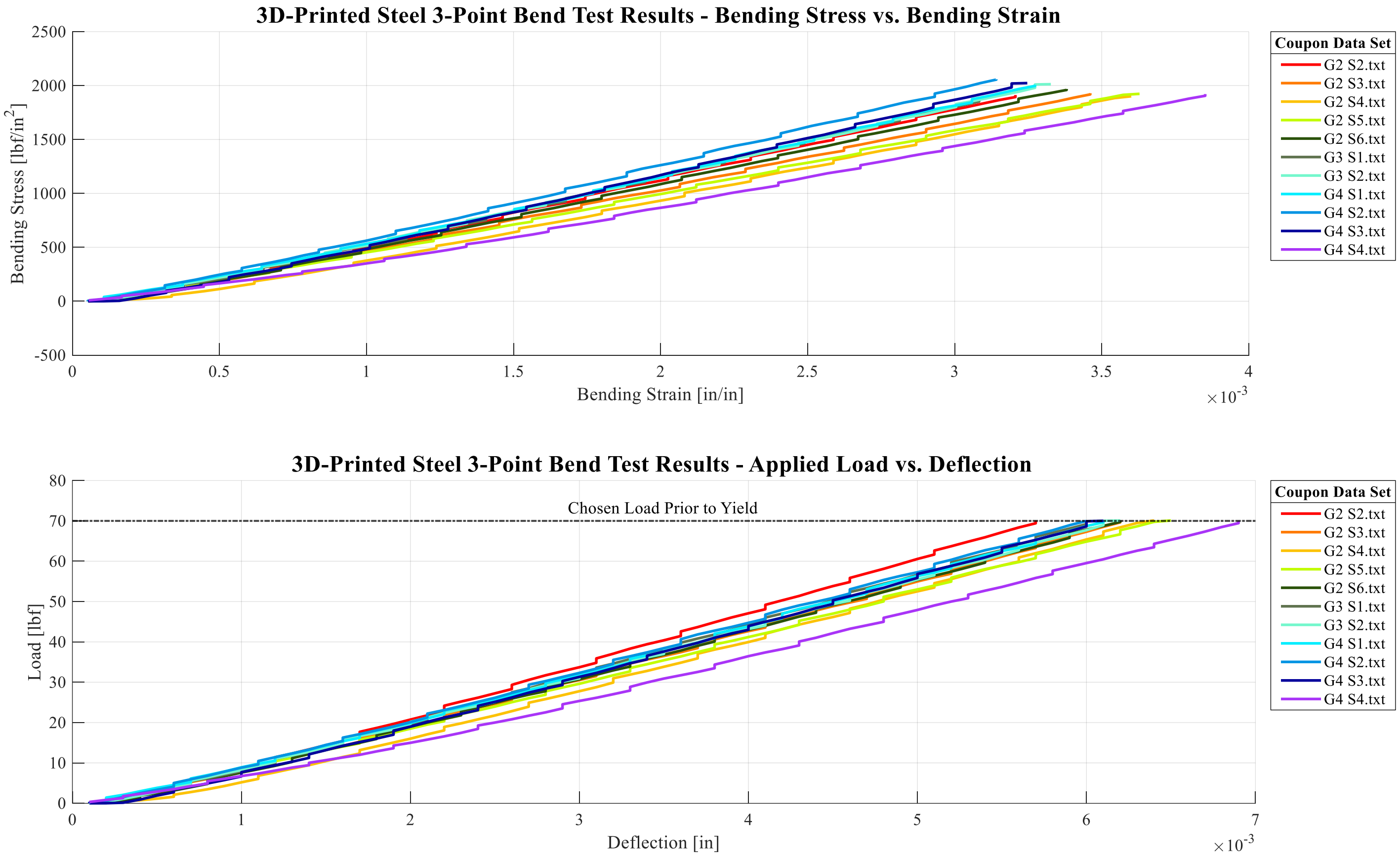

Figure 34. Steel Coupon 3-point Bending Test Plots.

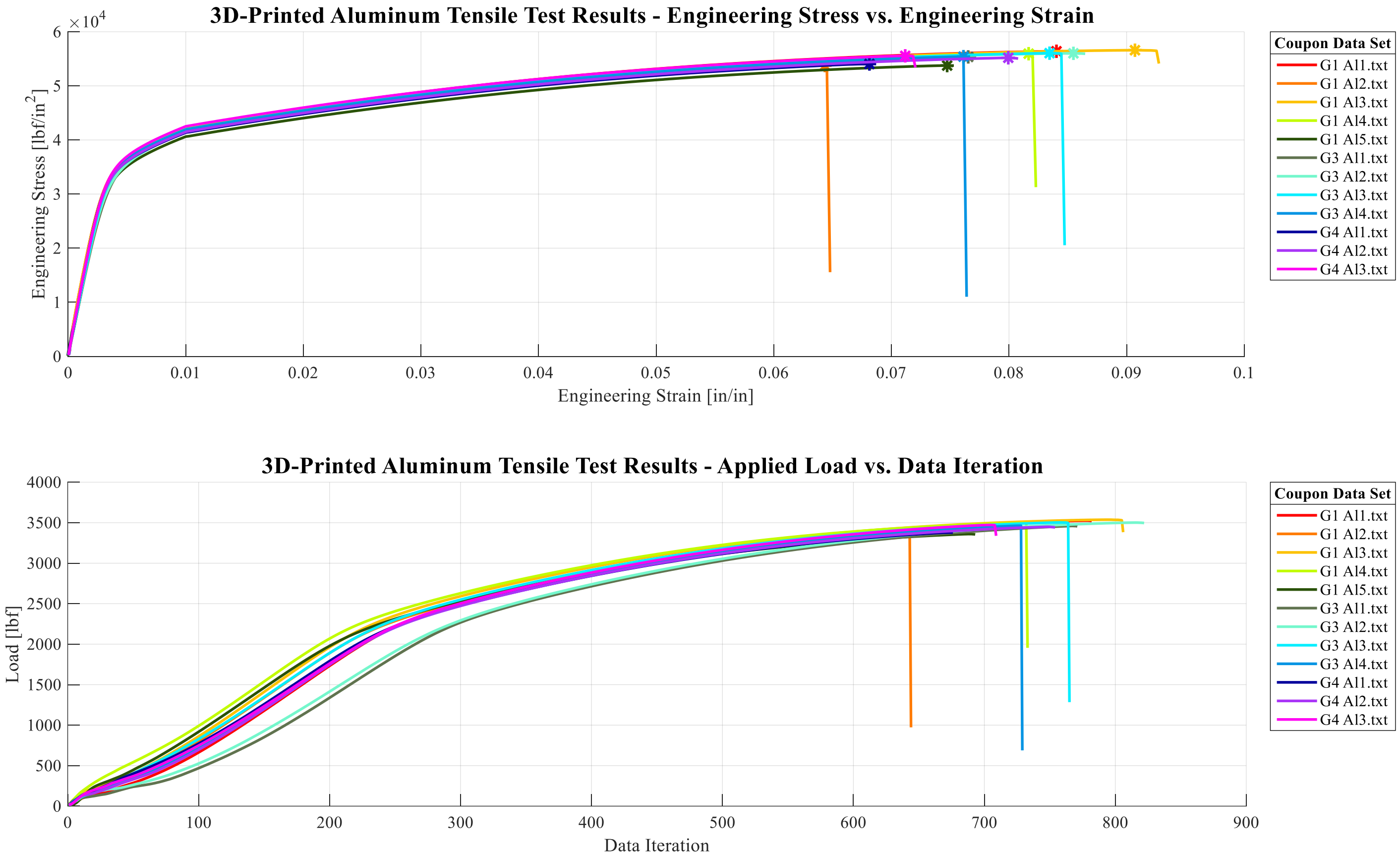

Figure 35. Aluminum Coupon Tensile Test Plots.

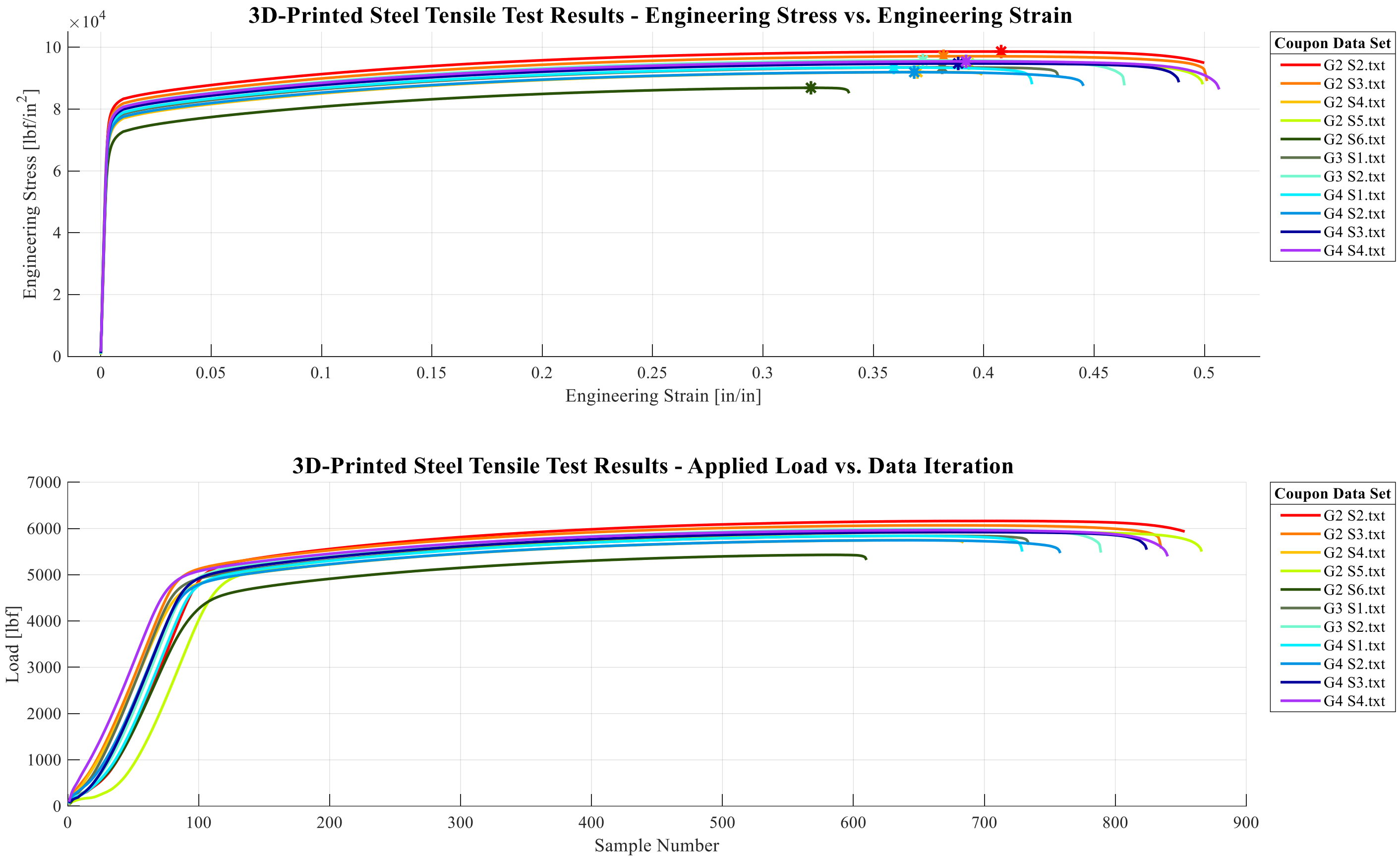

Figure 36. Steel Coupon Tensile Test Plots.

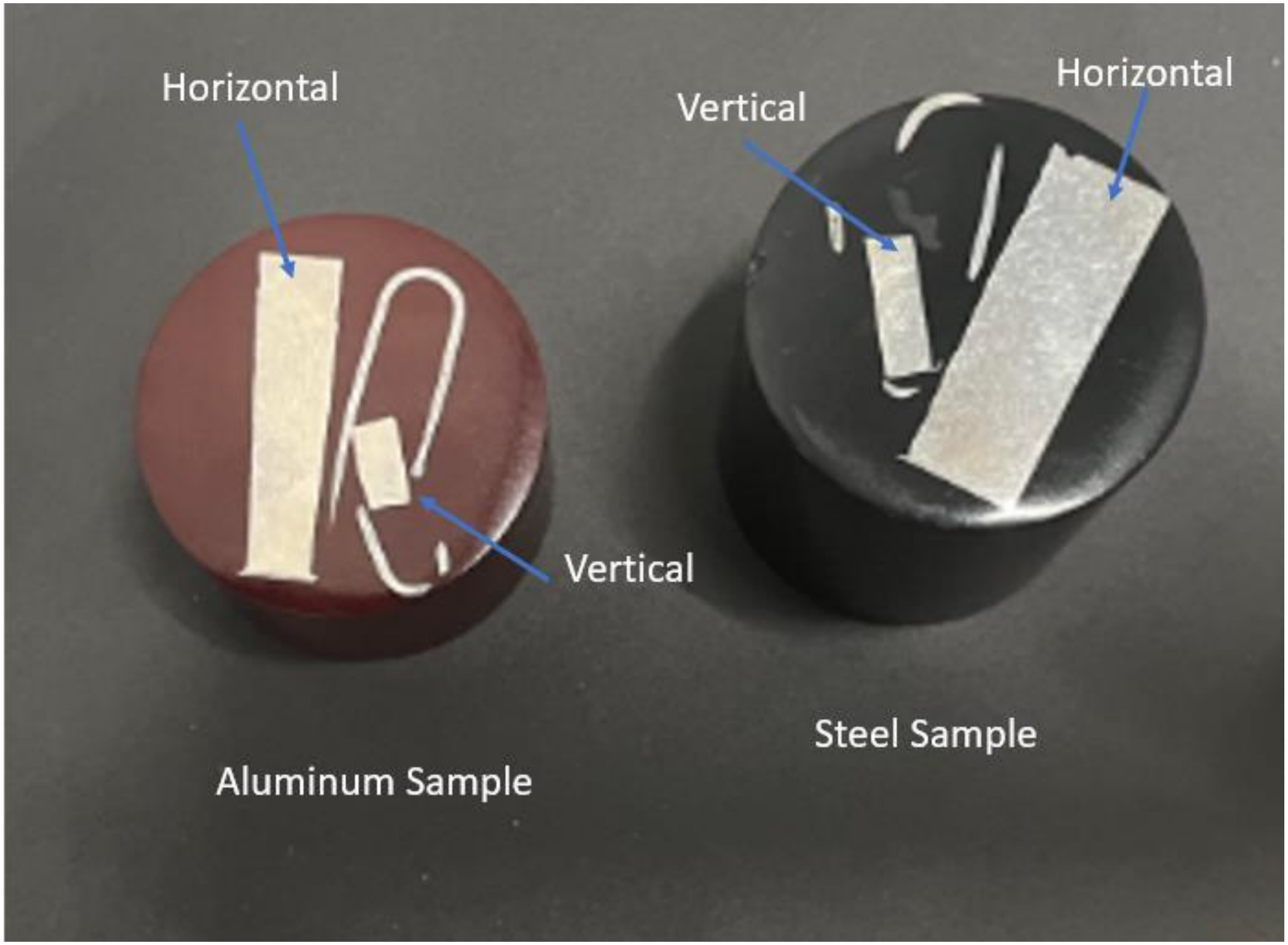

Figure 37. Mold Images for Polishing and Etching

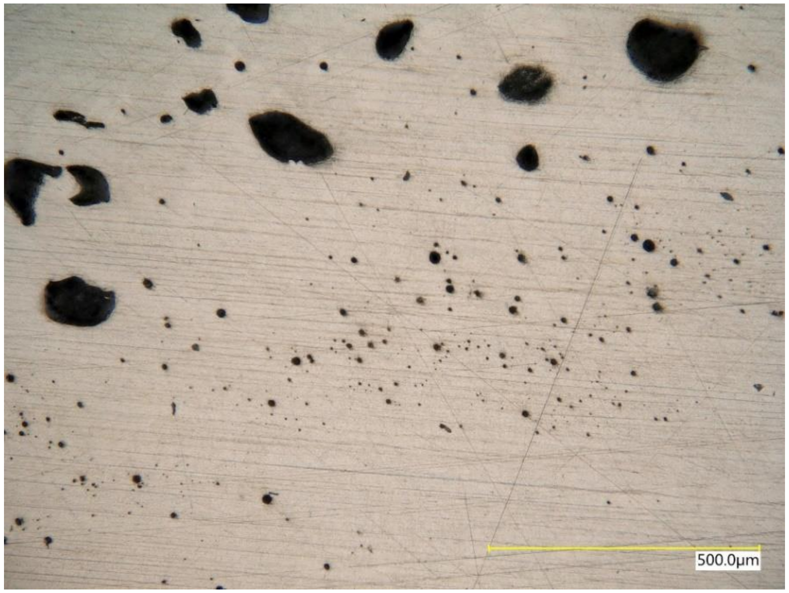

Figure 38. Polishing and Etching Aluminum Edge Sample 250X Magnification Unetched

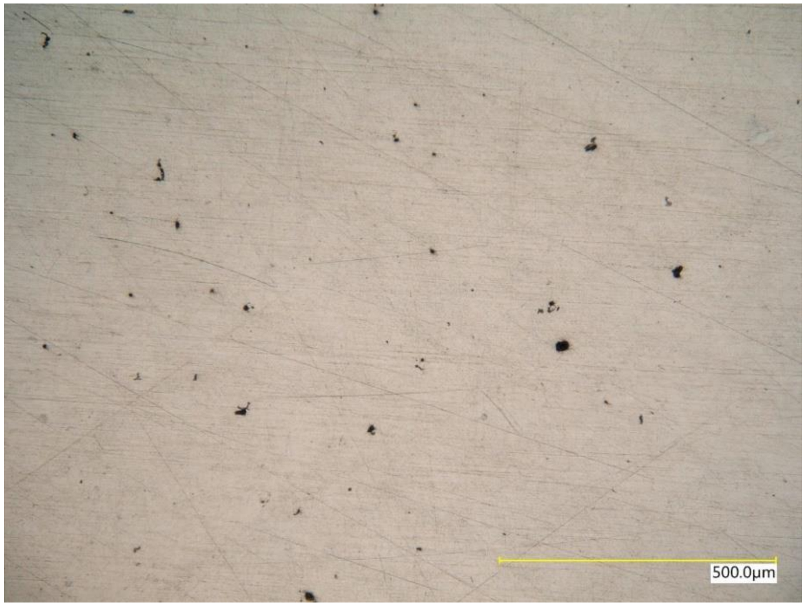

Figure 39. Polishing and Etching Aluminum Flat Sample 250X Magnification Unetched

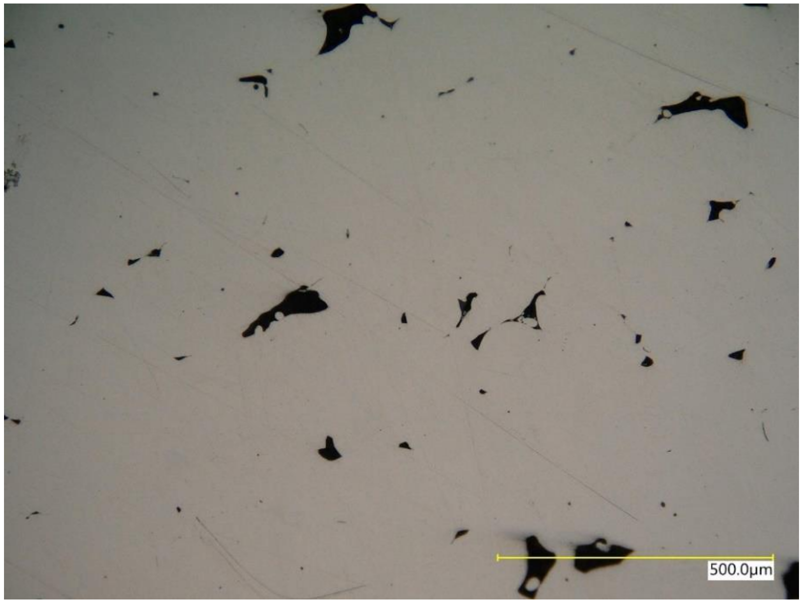

Figure 40. Polishing and Etching Steel Edge Sample 250X Magnification Unetched

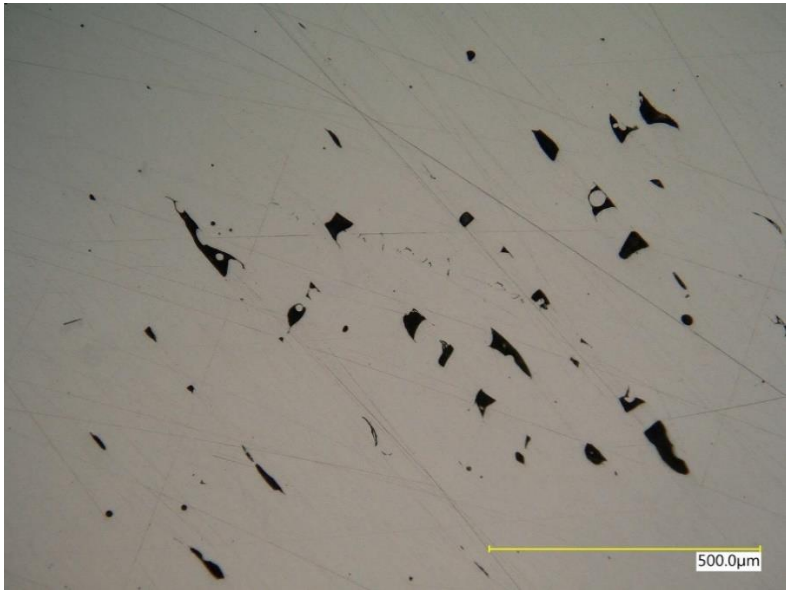

Figure 41. Polishing and Etching Steel Flat 250X Magnification Unetched

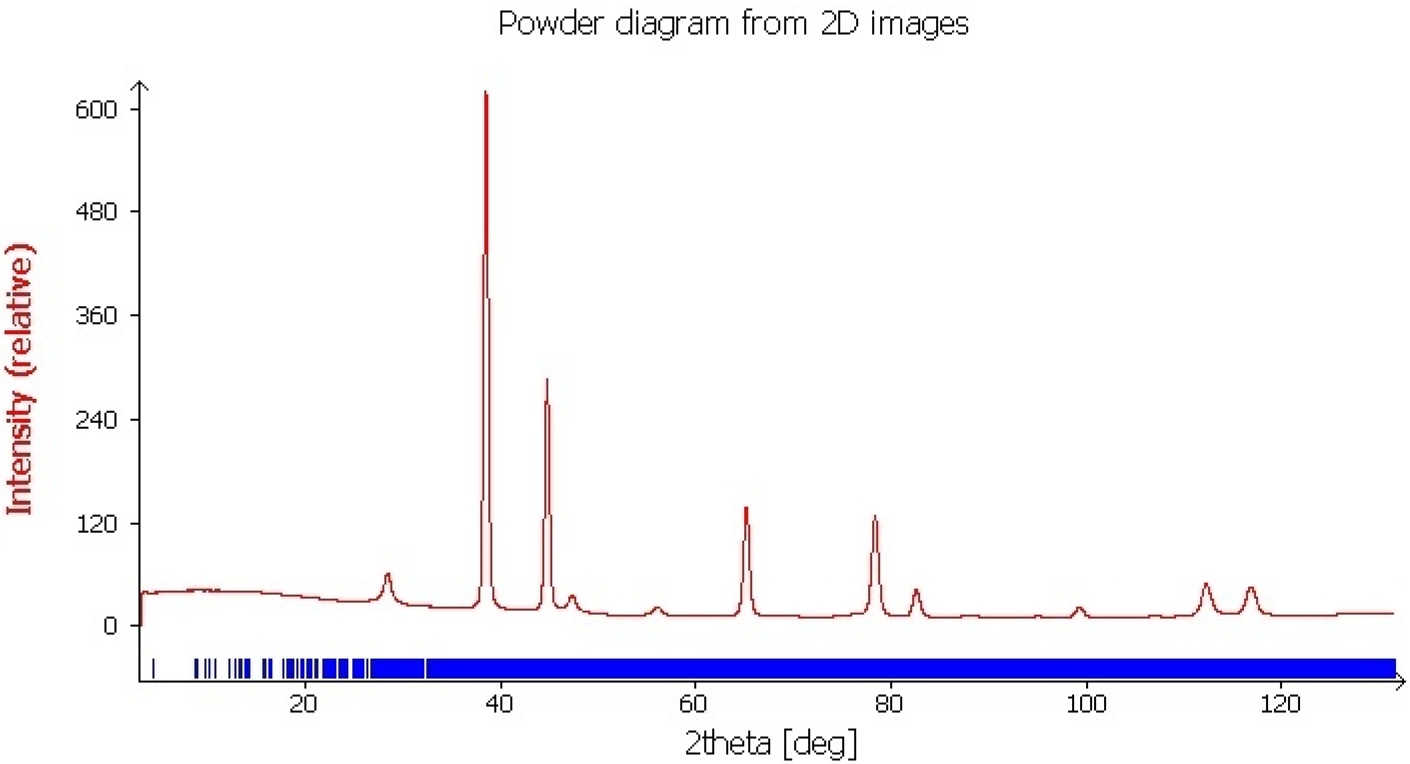

Figure 42. Intensity vs 2theta Plot for Aluminum Using Copper Radiation

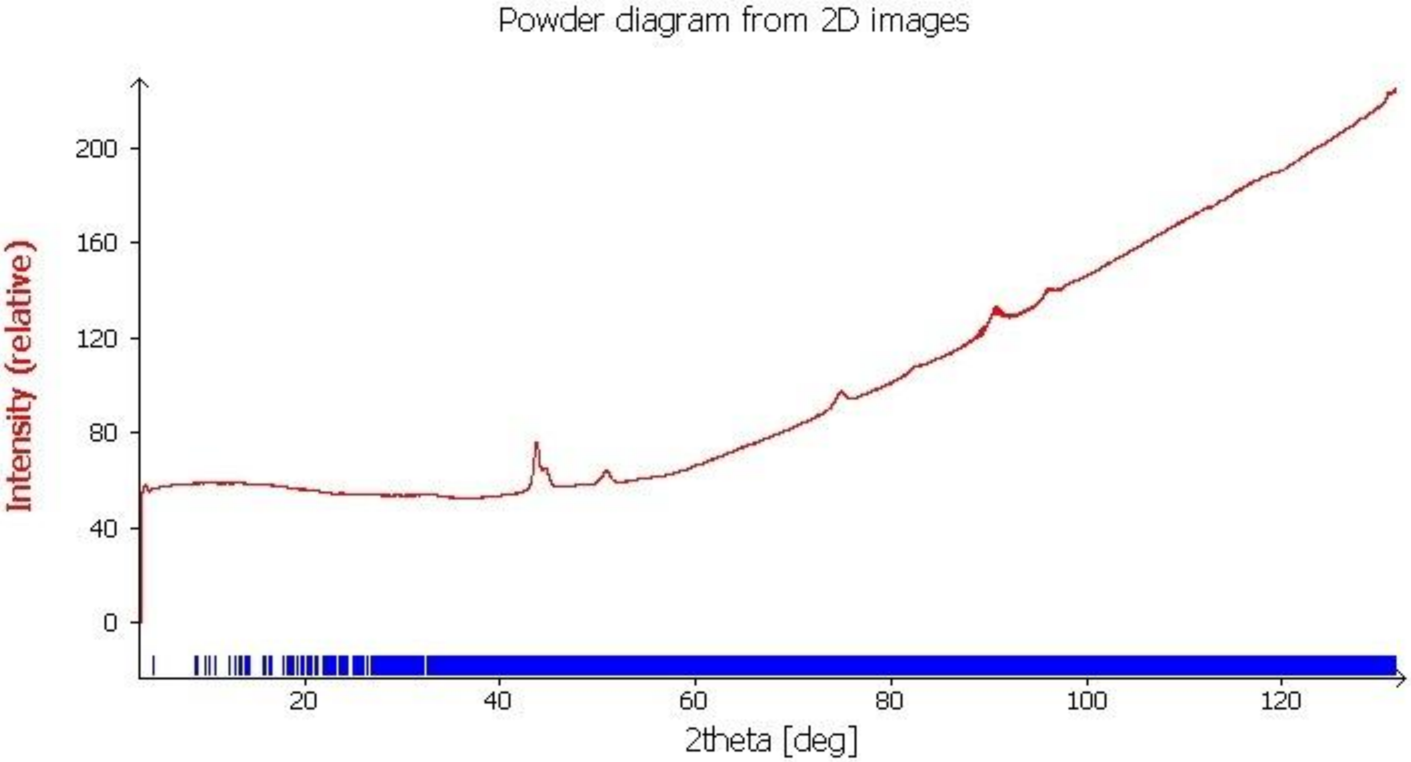

Figure 43. Intensity vs 2theta Plot for Steel Using Copper Radiation, was Deemed a Bad Plot and the XRD was Redone.

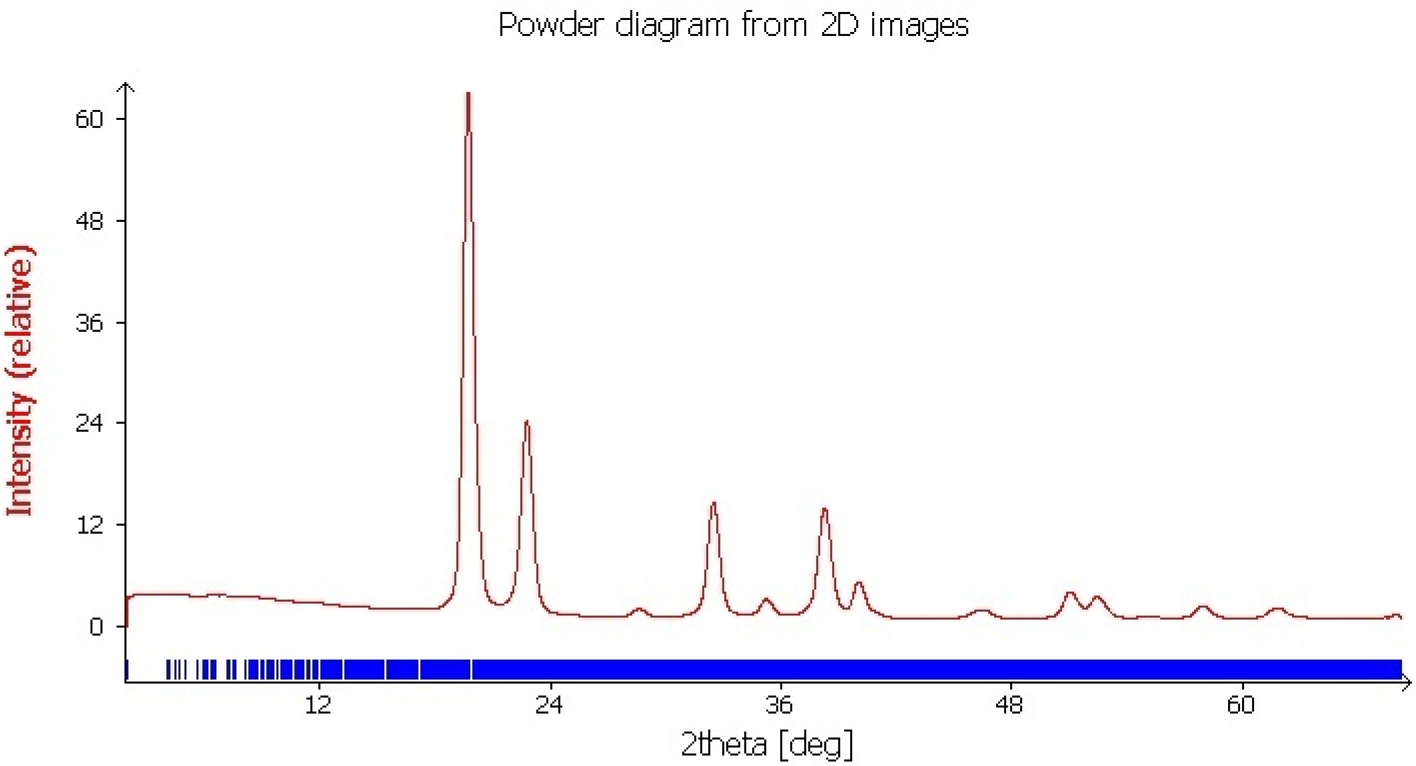

Figure 44. Intensity vs 2theta Plot for Steel Using Molybdenum Radiation

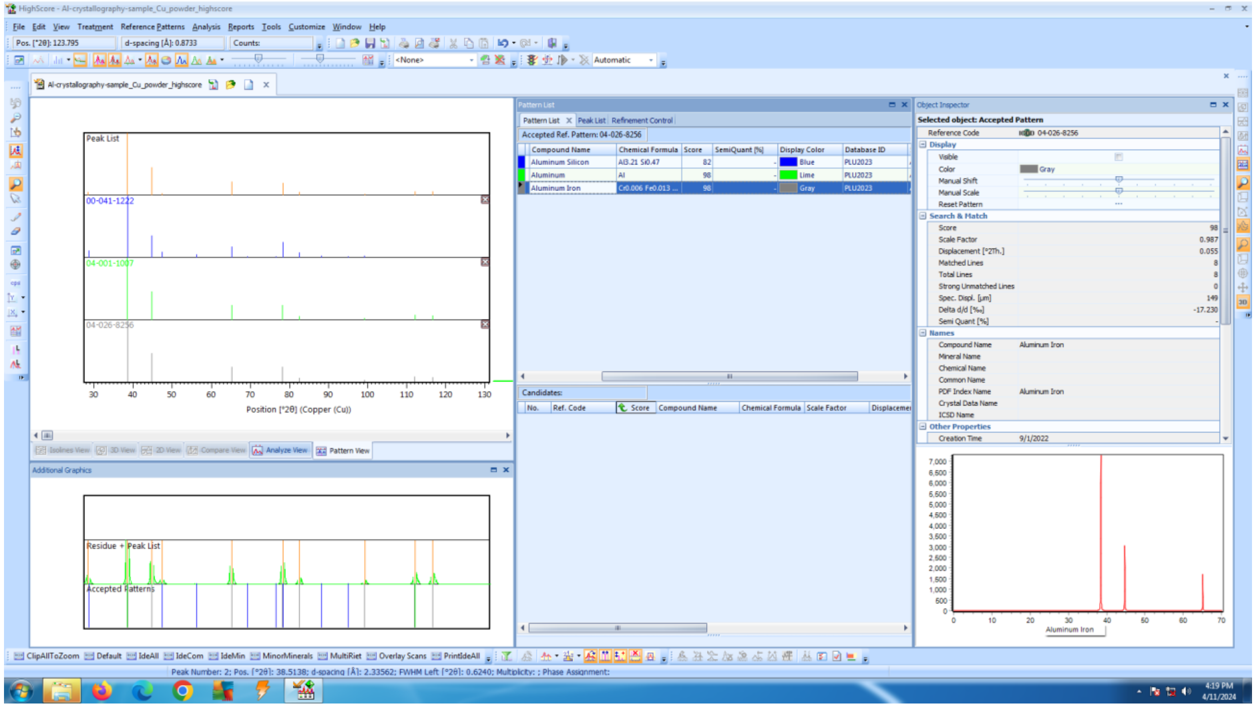

Accepted Ref. Pattern: 04-026-8256

	Compound Name	Chemical Formula	Score	SemiQuant [%]	Display Color	Database ID
🟦	Aluminum Silicon	Al3.21 Si0.47	82	-	🟦 Blue	PLU2023
🟩	Aluminum	Al	98	-	🟩 Lime	PLU2023
▶	Aluminum Iron	Cr0.006 Fe0.013 ...	98	-	▨ Gray	PLU2023

Selected object: Accepted Pattern

Reference Code 04-026-8256

Display
- Visible ☐
- Color ▨ Gray
- Manual Shift
- Manual Scale
- Reset Pattern ...

Search & Match
- Score 98
- Scale Factor 0.987
- Displacement [°2Th.] 0.055
- Matched Lines 8
- Total Lines 8
- Strong Unmatched Lines 0
- Spec. Displ. [µm] 149
- Delta d/d [‰] -17.230
- Semi Quant [%] -

Names
- Compound Name Aluminum Iron
- Mineral Name
- Chemical Name
- Common Name
- PDF Index Name Aluminum Iron
- Crystal Data Name
- ICSD Name

Other Properties
- Creation Time 9/1/2022

Peak Number: 2; Pos. [°2θ]: 38.5138; d-spacing [Å]: 2.33562; FWHM Left [°2θ]: 0.6240; Multiplicity: ; Phase Assignment:

Figure 45. Results From XRD Material Comparison Using HighScore Software

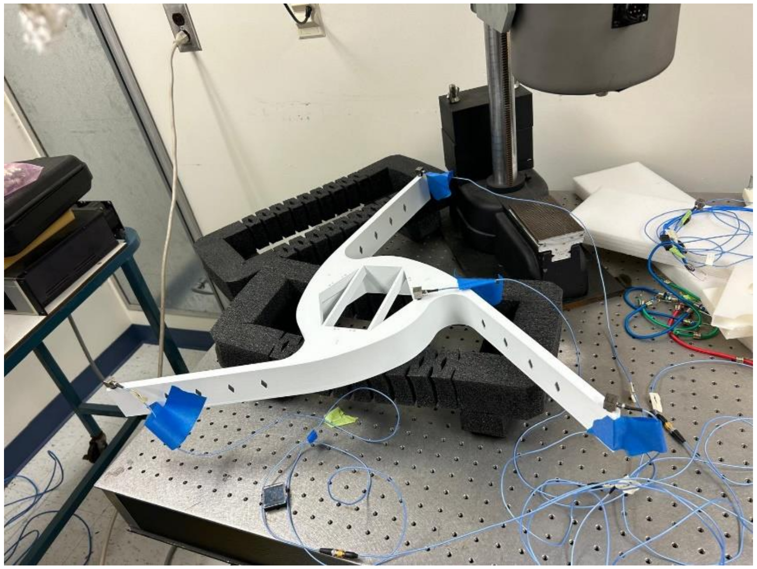

Figure 46. Initial Setup of Vibration Test Using Foam Cushion.

Figure 47. The Modal Strike Test With the Hanging Setup.

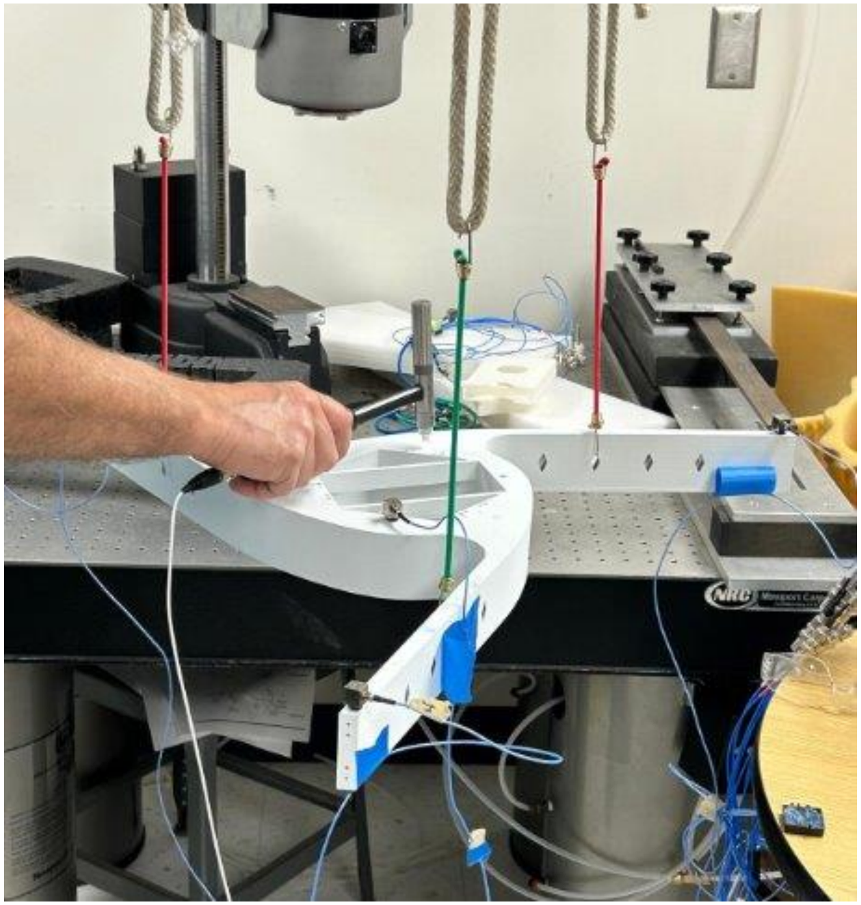

Figure 48. The Modal Strike Test in the Hanging Setup With the Hammer Strike Location.

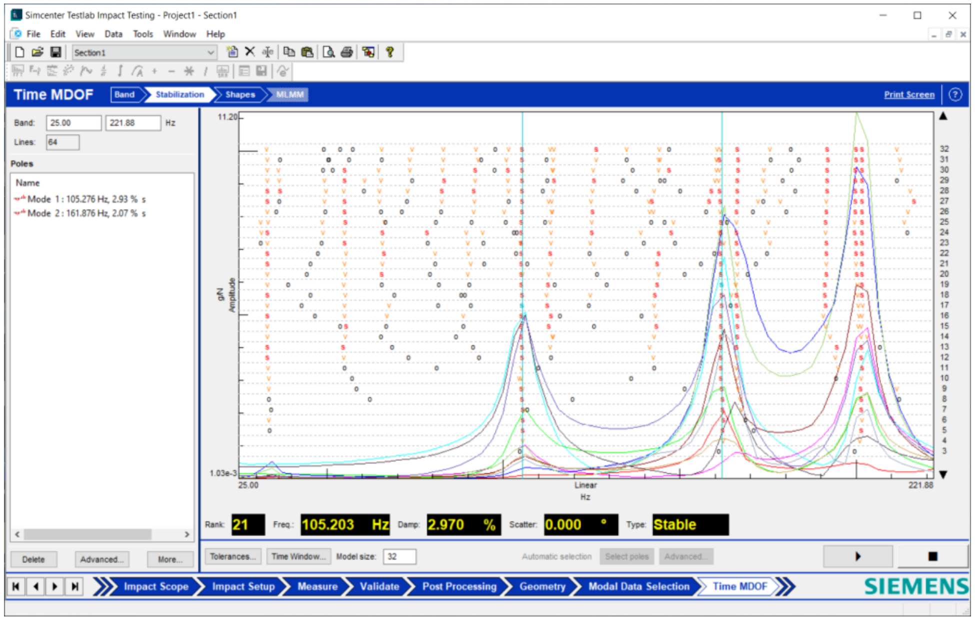

Band: 25.00 221.88 Hz

Lines: 64

Poles

Name

Mode 1 : 105.276 Hz, 2.93 % s

Mode 2 : 161.876 Hz, 2.07 % s

Rank: 21 Freq.: 105.203 Hz Damp: 2.970 % Scatter: 0.000 ° Type: Stable

Model size: 32

Figure 49. Modal Strike Data With the First Mode at 105.276 Hz.

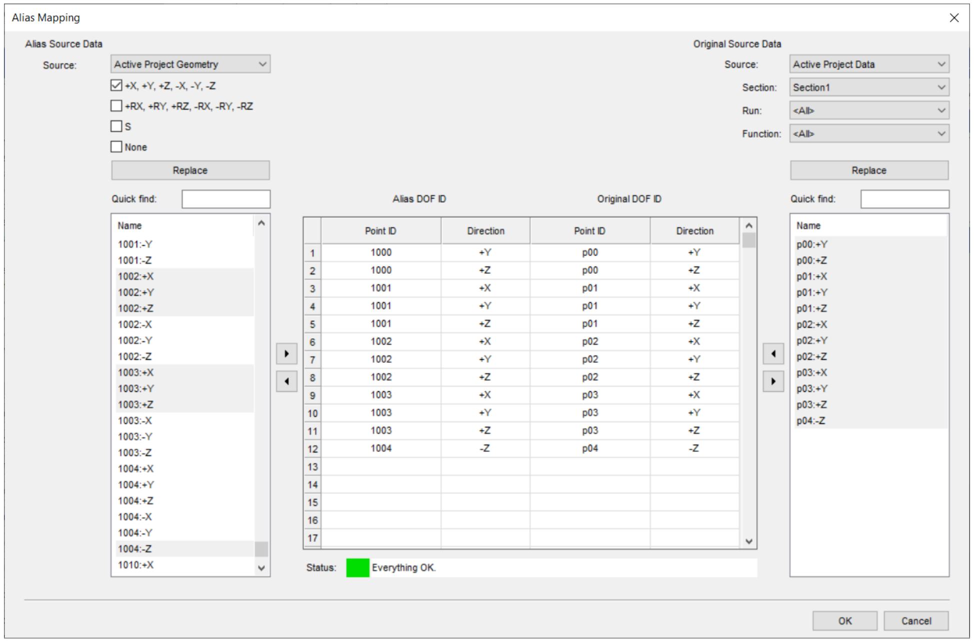

Alias Source Data

Source: Active Project Geometry

☑ +X, +Y, +Z, -X, -Y, -Z

☐ +RX, +RY, +RZ, -RX, -RY, -RZ

☐ S

☐ None

Original Source Data

Source: Active Project Data

Section: Section1

Run: <All>

Function: <All>

Name

1001:-Y
1001:-Z
1002:+X
1002:+Y
1002:+Z
1002:-X
1002:-Y
1002:-Z
1003:+X
1003:+Y
1003:+Z
1003:-X
1003:-Y
1003:-Z
1004:+X
1004:+Y
1004:+Z
1004:-X
1004:-Y
1004:-Z
1010:+X

	Alias DOF ID		Original DOF ID	
	Point ID	Direction	Point ID	Direction
1	1000	+Y	p00	+Y
2	1000	+Z	p00	+Z
3	1001	+X	p01	+X
4	1001	+Y	p01	+Y
5	1001	+Z	p01	+Z
6	1002	+X	p02	+X
7	1002	+Y	p02	+Y
8	1002	+Z	p02	+Z
9	1003	+X	p03	+X
10	1003	+Y	p03	+Y
11	1003	+Z	p03	+Z
12	1004	-Z	p04	-Z
13				
14				
15				
16				
17				

Status: Everything OK.

Name

p00:+Y
p00:+Z
p01:+X
p01:+Y
p01:+Z
p02:+X
p02:+Y
p02:+Z
p03:+X
p03:+Y
p03:+Z
p04:-Z

Figure 50. Alias Mapping of Accelerometer Data to Universal Model for the Modal Strike Test in the Hanging Setup.

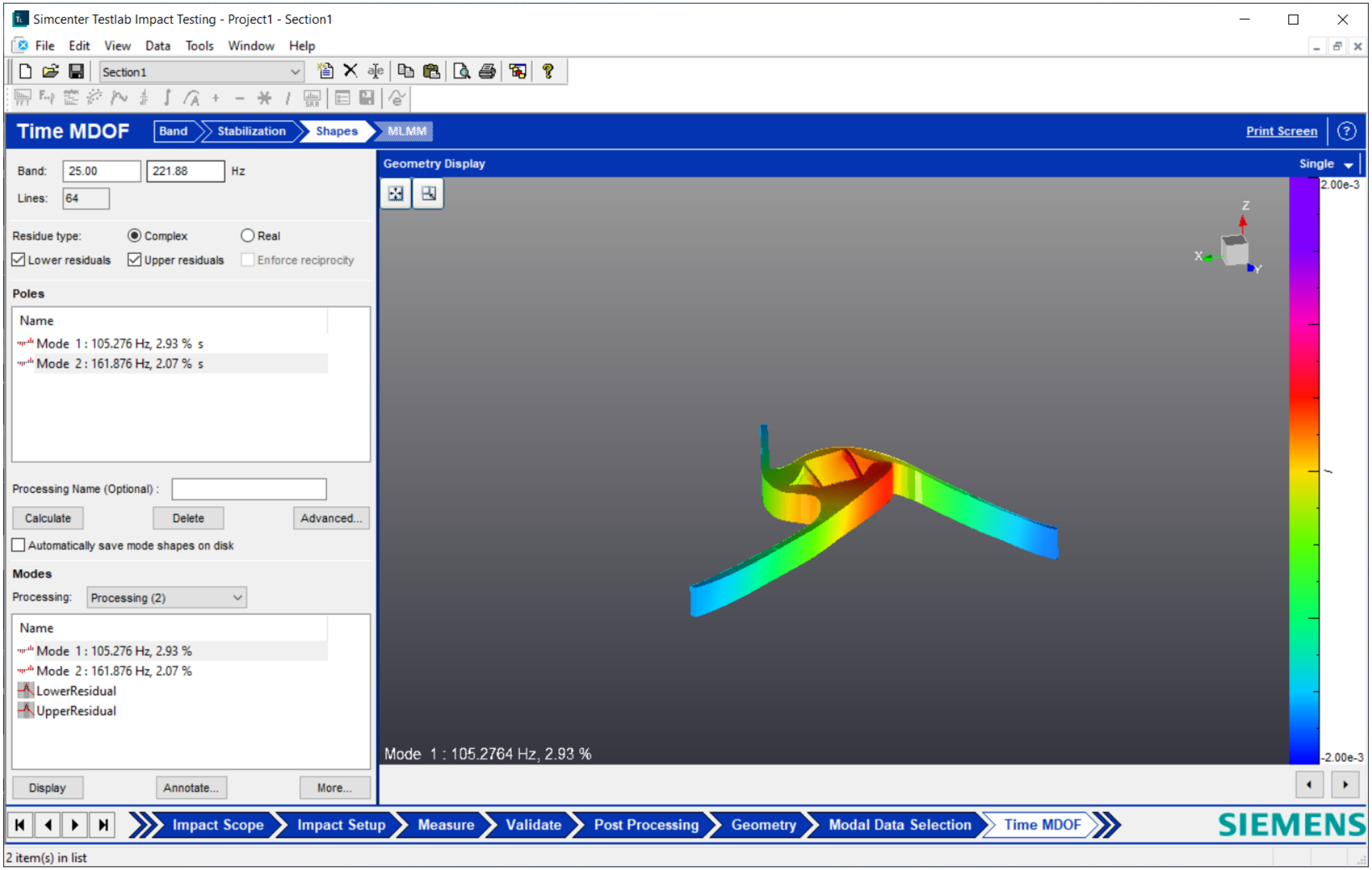

Band: 25.00 221.88 Hz

Lines: 64

Residue type: ● Complex ○ Real

☑ Lower residuals ☑ Upper residuals ☐ Enforce reciprocity

Poles

Name
Mode 1 : 105.276 Hz, 2.93 % s
Mode 2 : 161.876 Hz, 2.07 % s

Processing Name (Optional) :

☐ Automatically save mode shapes on disk

Modes

Processing: Processing (2)

Name
Mode 1 : 105.276 Hz, 2.93 %
Mode 2 : 161.876 Hz, 2.07 %
LowerResidual
UpperResidual

Mode 1 : 105.2764 Hz, 2.93 %

2 item(s) in list

Figure 51. Mode 1 Frequency Plot for the Modal Strike Test in the Hanging Setup With the Model Geometry Mapped Onto the Plot.

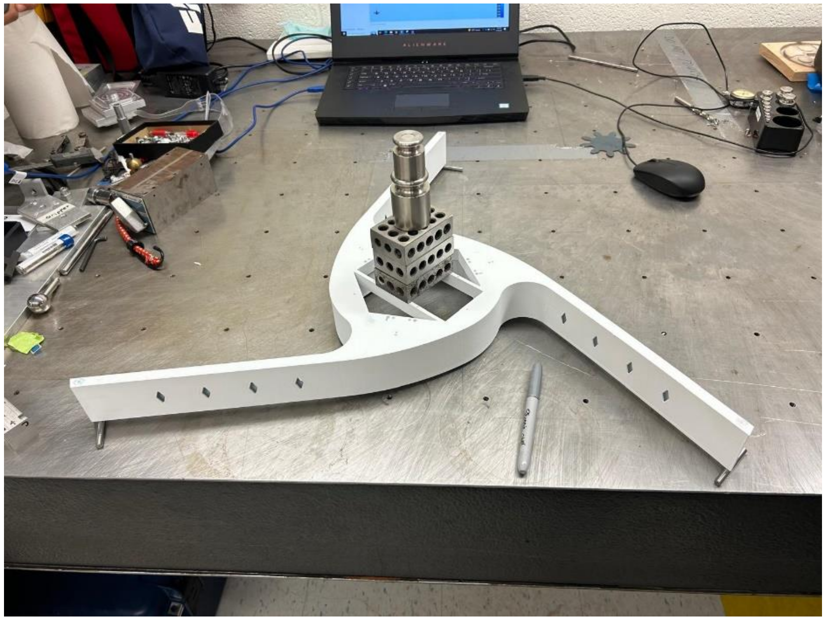

Figure 52. Initial Displacement Test Setup With 1-2-3-Inch Blocks, Lab Weights, and Small Metal Cylinders.

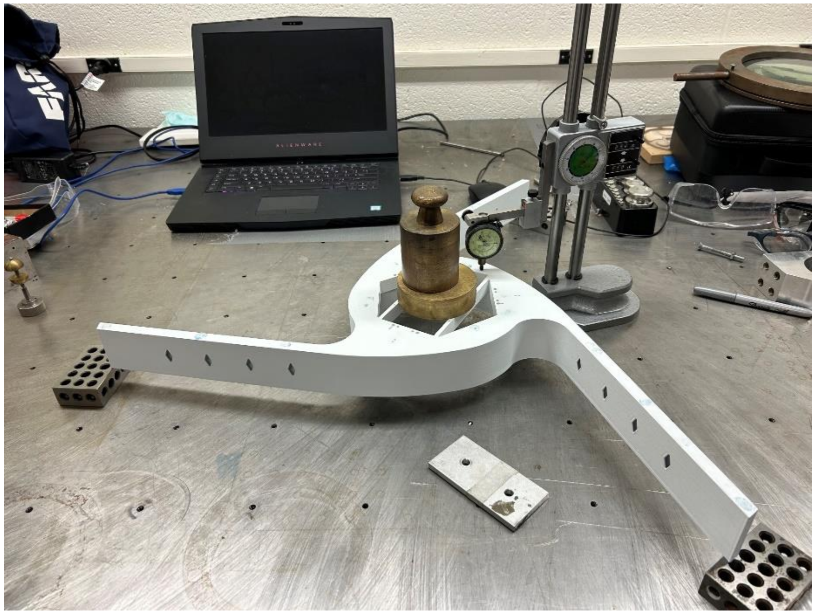

Figure 53. Analog Displacement Test Setup With 3,434.2 Grams of Mass Placed on the Model.

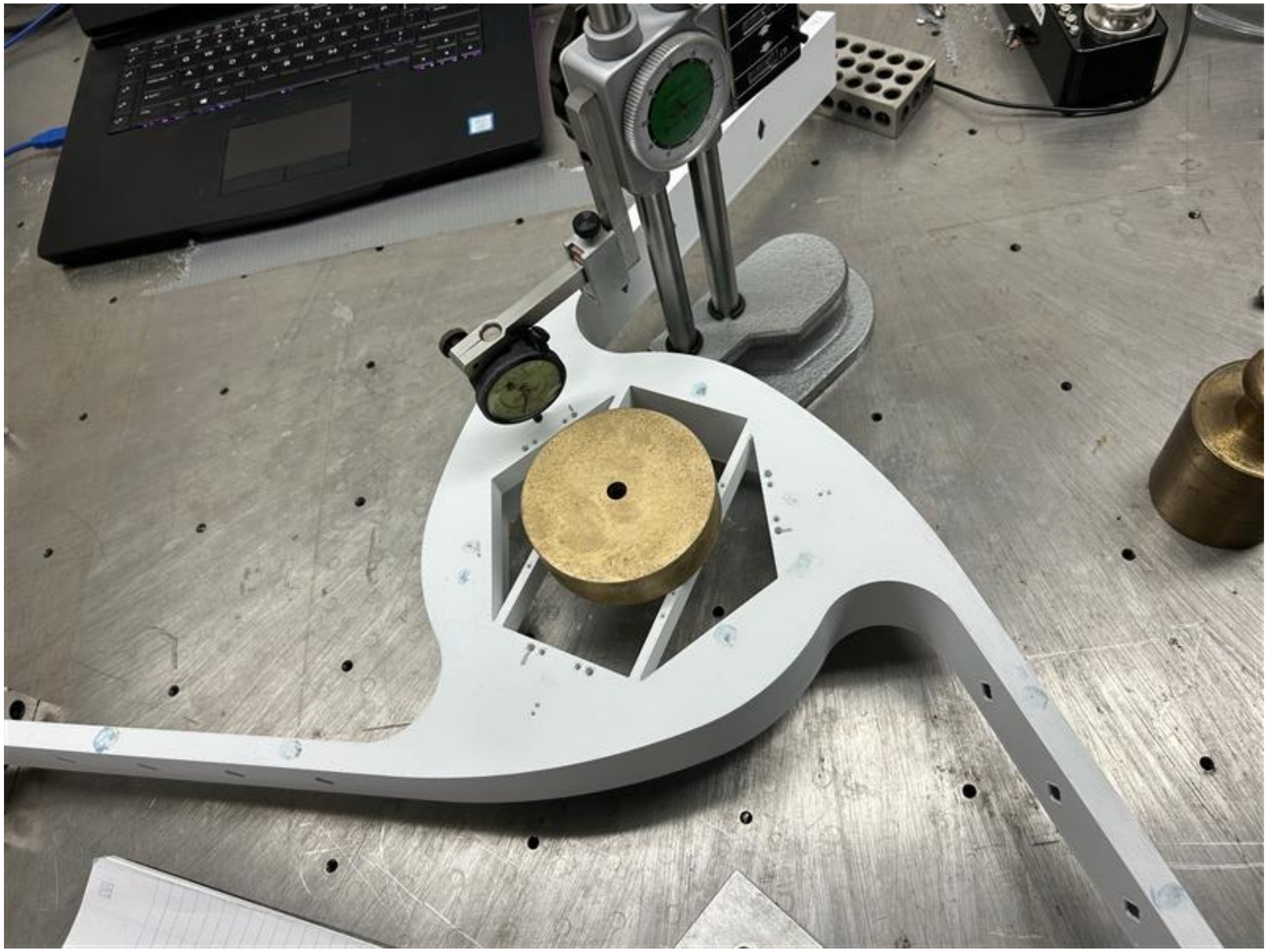

Figure 54. Second Measurement Location for Analog Displacement Test.

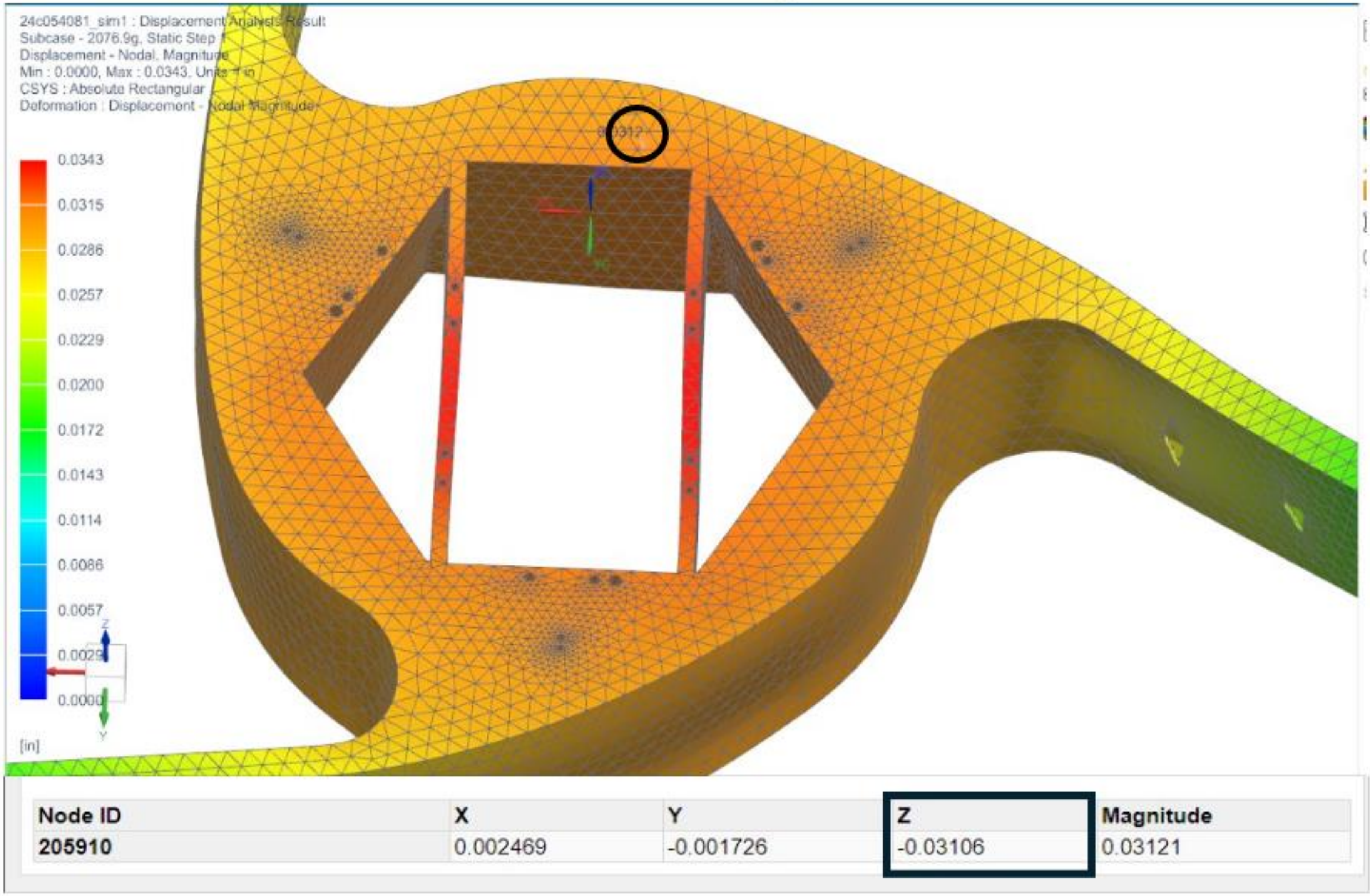

```
24c054081_sim1 : Displacement Analysis Result
Subcase - 2076.9g, Static Step 1
Displacement - Nodal, Magnitude
Min : 0.0000, Max : 0.0343, Units = in
CSYS : Absolute Rectangular
Deformation : Displacement - Nodal Magnitude
```

Node ID	X	Y	Z	Magnitude
205910	0.002469	-0.001726	-0.03106	0.03121

Figure 55. NX Displacement Plot Simulating the Second Displacement Test With a Displacement Measurement From the First Measurement Location. The Simulated Displacement was 0.03106 Inches With 2,076.9 Grams Applied.

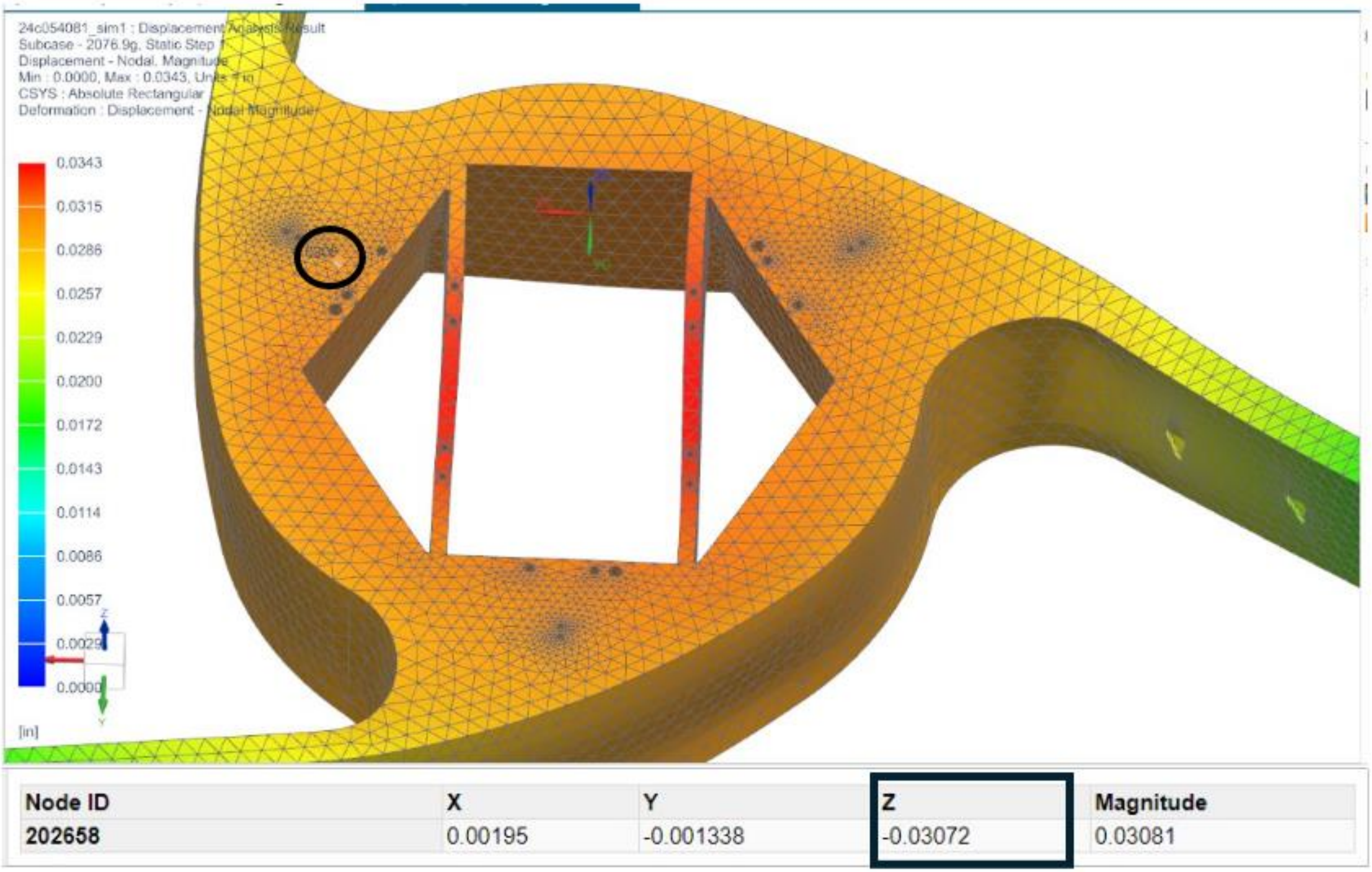

```
24c054081_sim1 : Displacement Analysis Result
Subcase - 2076.9g, Static Step 1
Displacement - Nodal, Magnitude
Min : 0.0000, Max : 0.0343, Units = in
CSYS : Absolute Rectangular
Deformation : Displacement - Nodal Magnitude
```

Node ID	X	Y	Z	Magnitude
202658	0.00195	-0.001338	-0.03072	0.03081

Figure 56. NX Displacement Plot Simulating the Second Displacement Test With a Displacement Measurement From the Second Measurement Location. The Simulated Displacement was 0.03072 Inches With 2,076.9 Grams Applied.

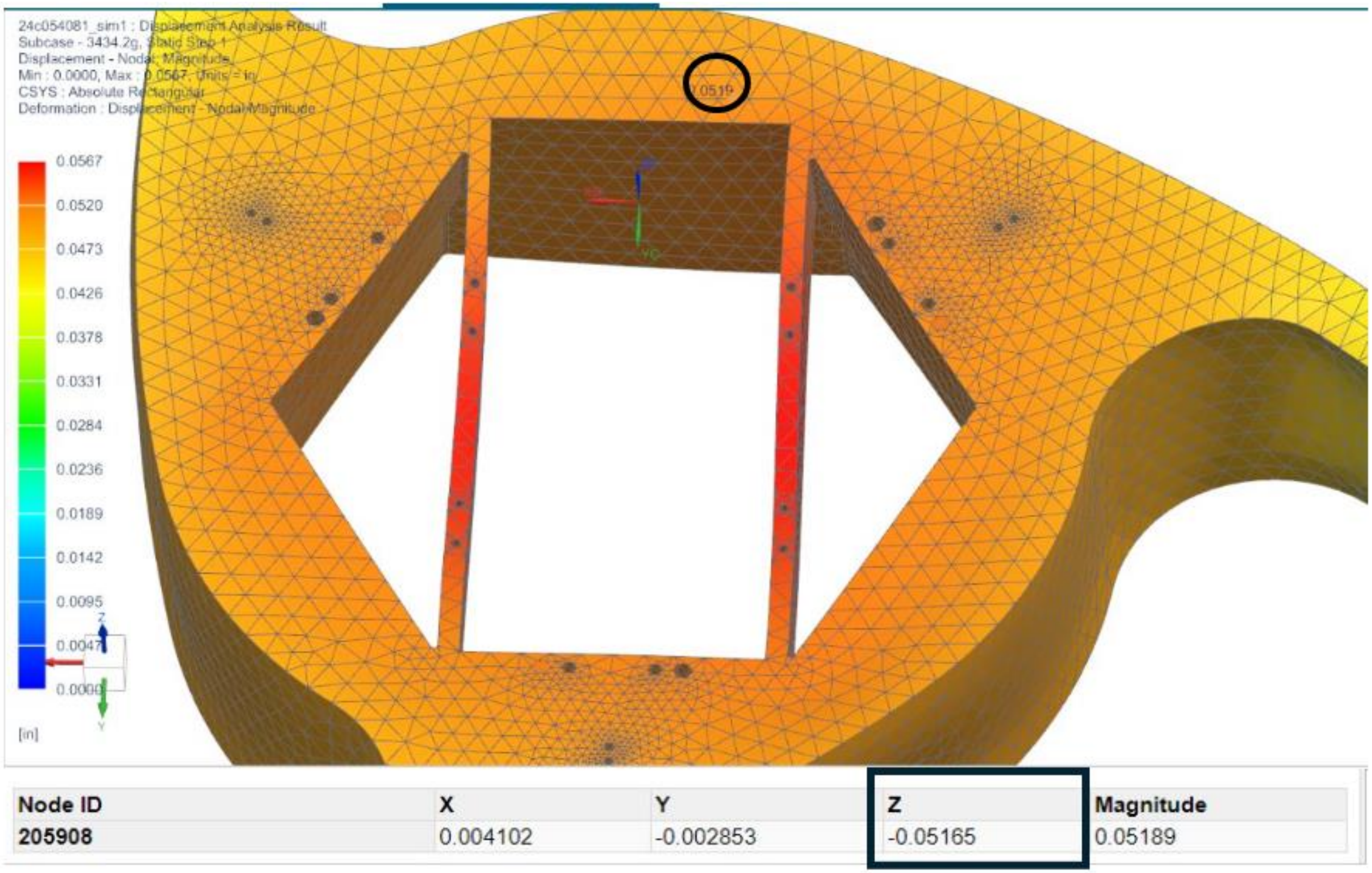

24c054081_sim1 : Displacement Analysis Result
Subcase - 3434.2g, Static Step 1
Displacement - Nodal, Magnitude
Min : 0.0000, Max : 0.0567, Units = in
CSYS : Absolute Rectangular
Deformation : Displacement - Nodal Magnitude

Node ID	X	Y	Z	Magnitude
205908	0.004102	-0.002853	-0.05165	0.05189

Figure 57. NX Displacement Plot Simulating the Second Displacement Test With a Displacement Measurement From the First Measurement Location. The Simulated Displacement was 0.05165 Inches With 3,434.2 Grams Applied.

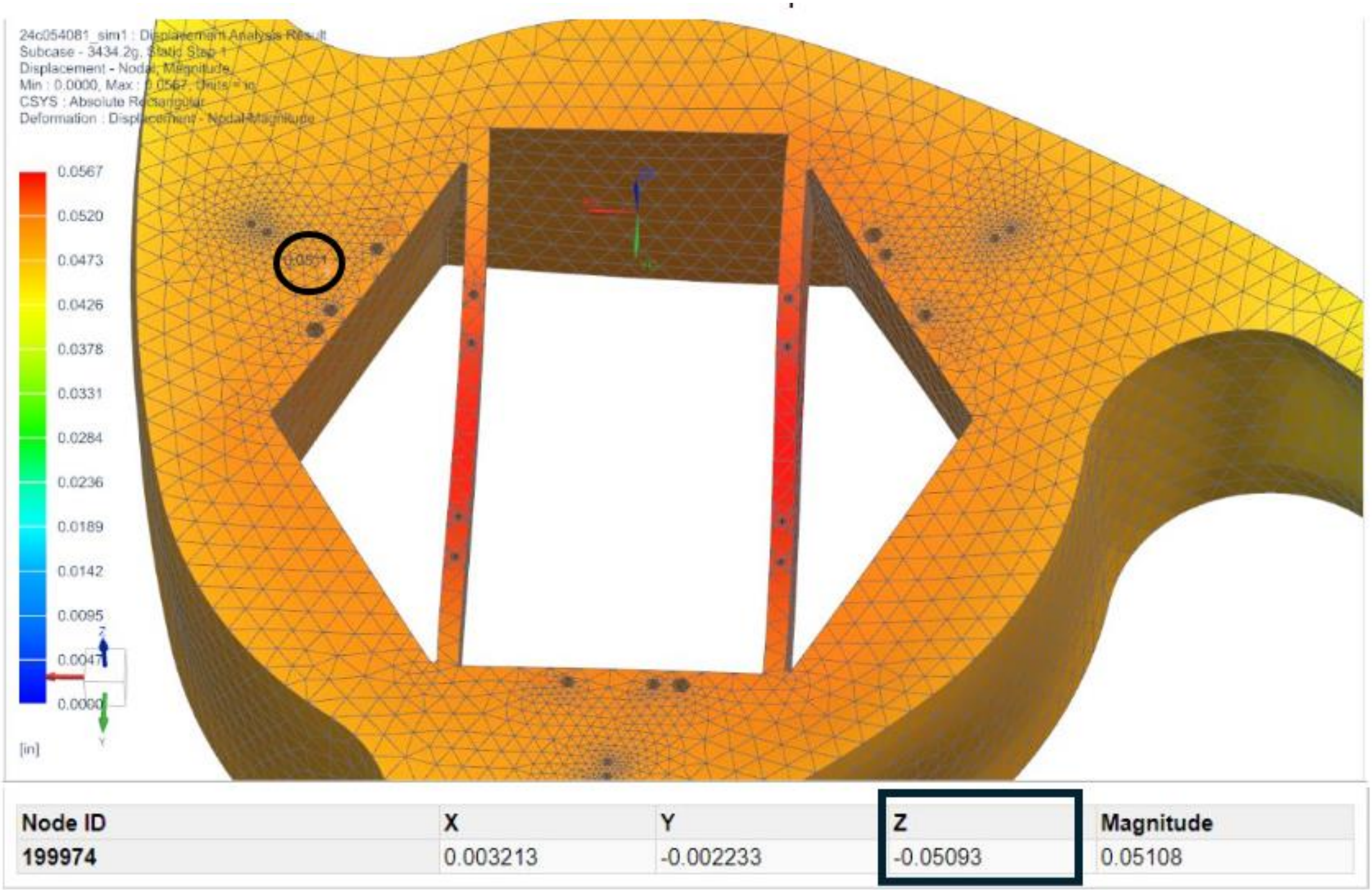

24c054081_sim1 : Displacement Analysis Result
Subcase - 3434.2g, Static Step 1
Displacement - Nodal, Magnitude
Min : 0.0000, Max : 0.0567, Units = in
CSYS : Absolute Rectangular
Deformation : Displacement - Nodal Magnitude

Node ID	X	Y	Z	Magnitude
199974	0.003213	-0.002233	-0.05093	0.05108

Figure 58. NX Displacement Plot Simulating the Second Displacement Test With a Displacement Measurement From the Second Measurement Location. The Simulated Displacement was 0.05093 Inches with 3,434.2 Grams Applied.

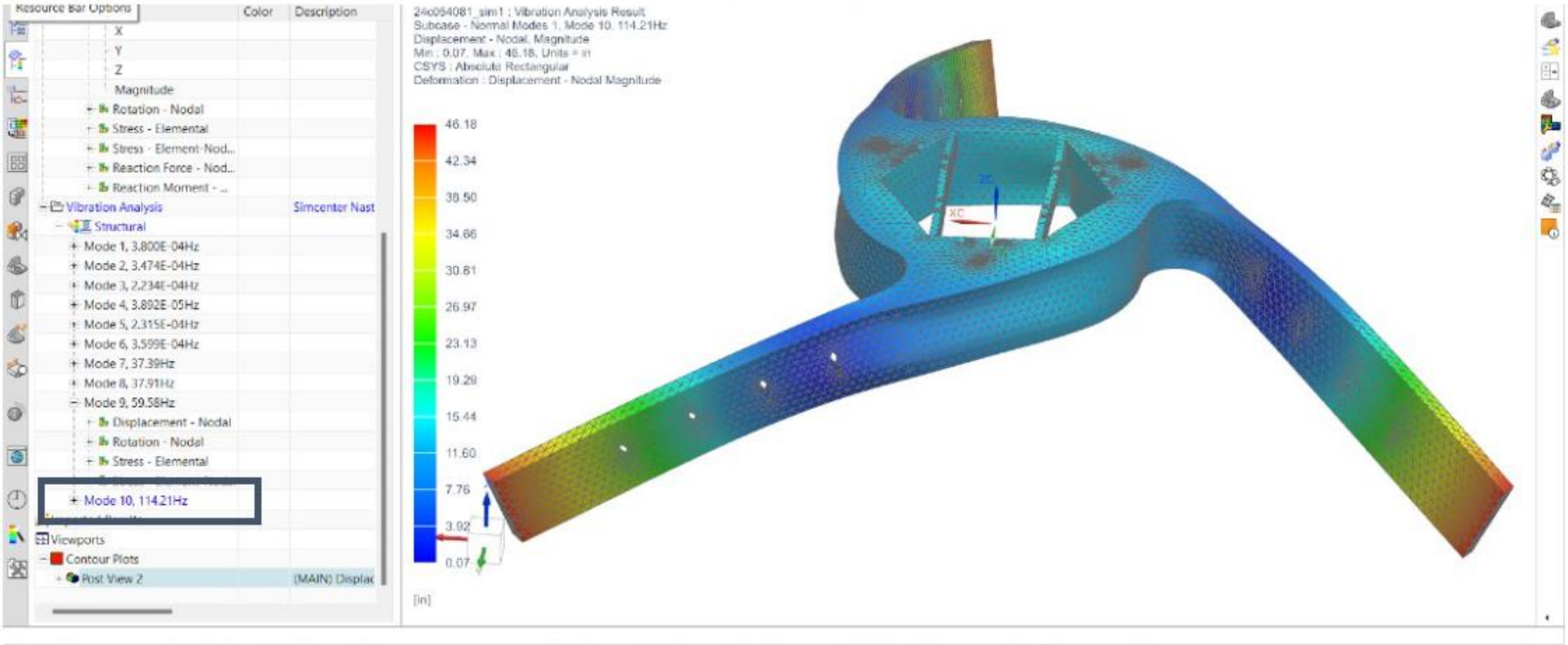

24c054081_sim1 : Vibration Analysis Result
Subcase - Normal Modes 1, Mode 10, 114.21Hz
Displacement - Nodal, Magnitude
Min : 0.07, Max : 46.18, Units = in
CSYS : Absolute Rectangular
Deformation : Displacement - Nodal Magnitude

Figure 59. NX Modal Simulation of the Printed Model with Free-Free Boundary Conditions. The First Nonzero Piston Mode was Mode 10 With a Natural Frequency of 114.21 Hz.

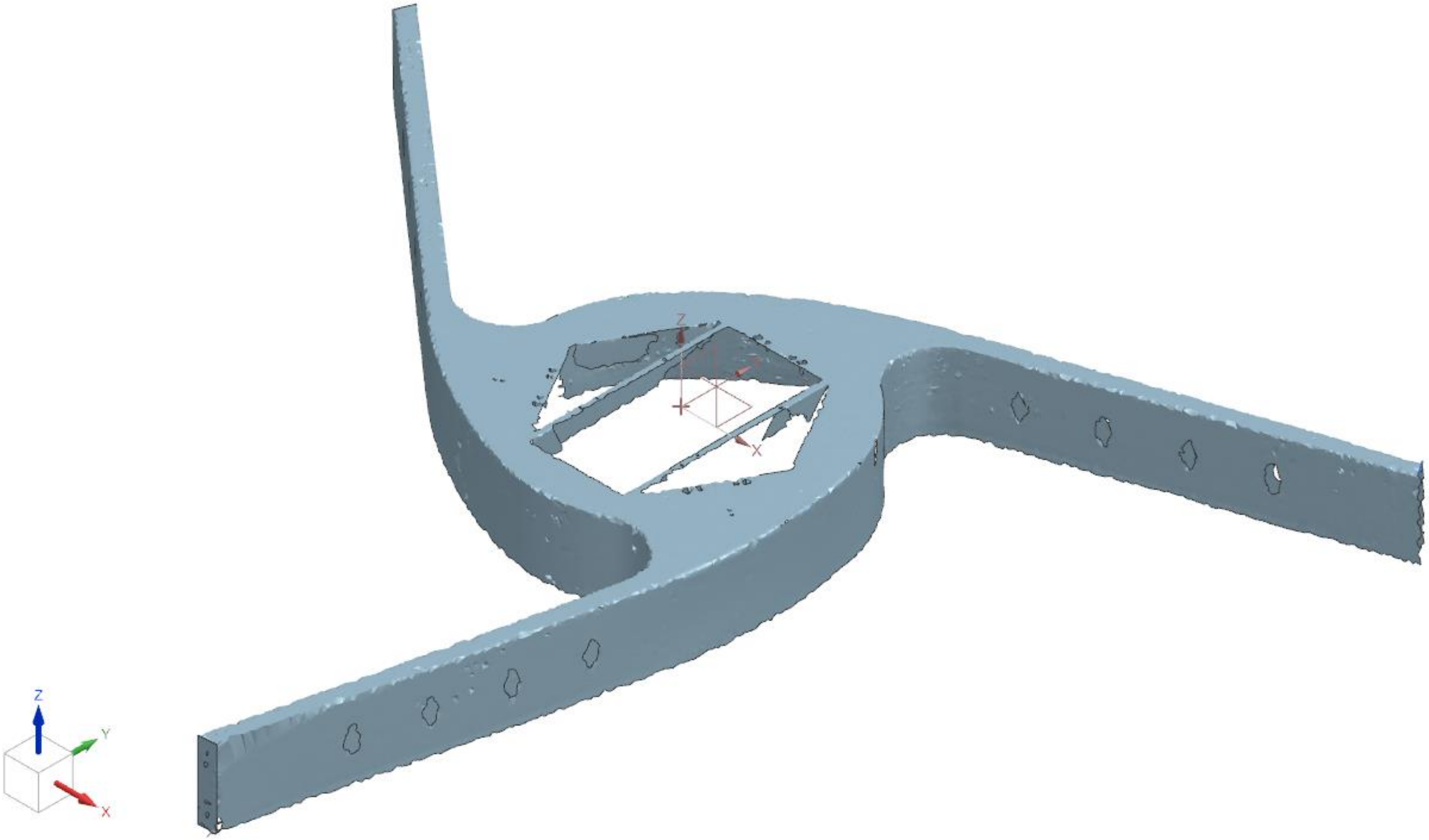

Figure 60. Point Cloud Scan of Prototype Model Loaded in NX

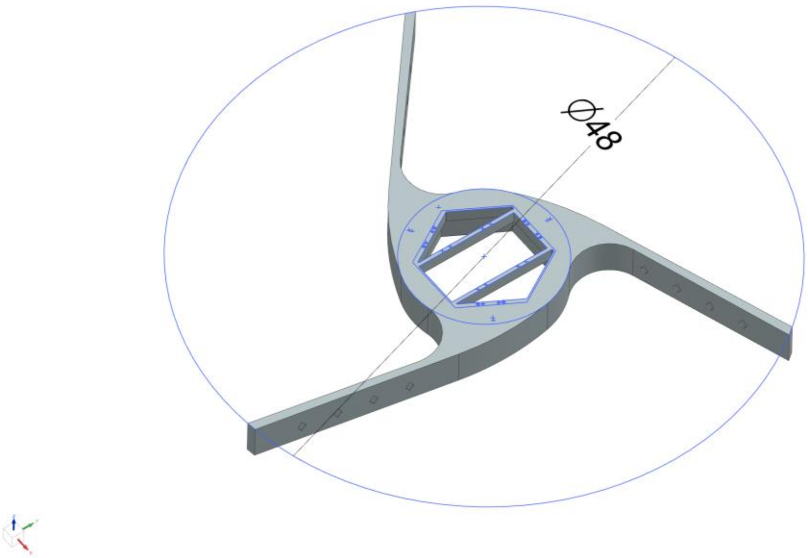

Figure 61. NX Verification of Diameter Specification.

\

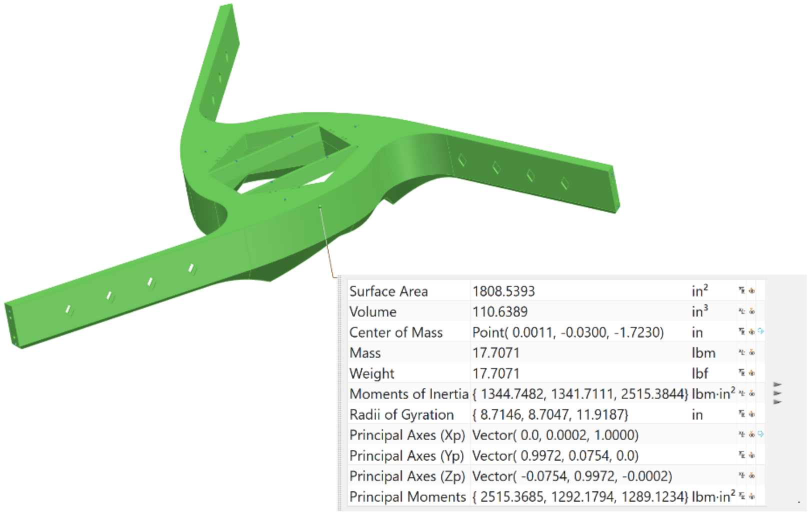

Surface Area	1808.5393	in^2	
Volume	110.6389	in^3	
Center of Mass	Point(0.0011, -0.0300, -1.7230)	in	
Mass	17.7071	lbm	
Weight	17.7071	lbf	
Moments of Inertia	{ 1344.7482, 1341.7111, 2515.3844}	$lbm{\cdot}in^2$	
Radii of Gyration	{ 8.7146, 8.7047, 11.9187}	in	
Principal Axes (Xp)	Vector(0.0, 0.0002, 1.0000)		
Principal Axes (Yp)	Vector(0.9972, 0.0754, 0.0)		
Principal Axes (Zp)	Vector(-0.0754, 0.9972, -0.0002)		
Principal Moments	{ 2515.3685, 1292.1794, 1289.1234}	$lbm{\cdot}in^2$	

Figure 62. Mass Verification of Final Model

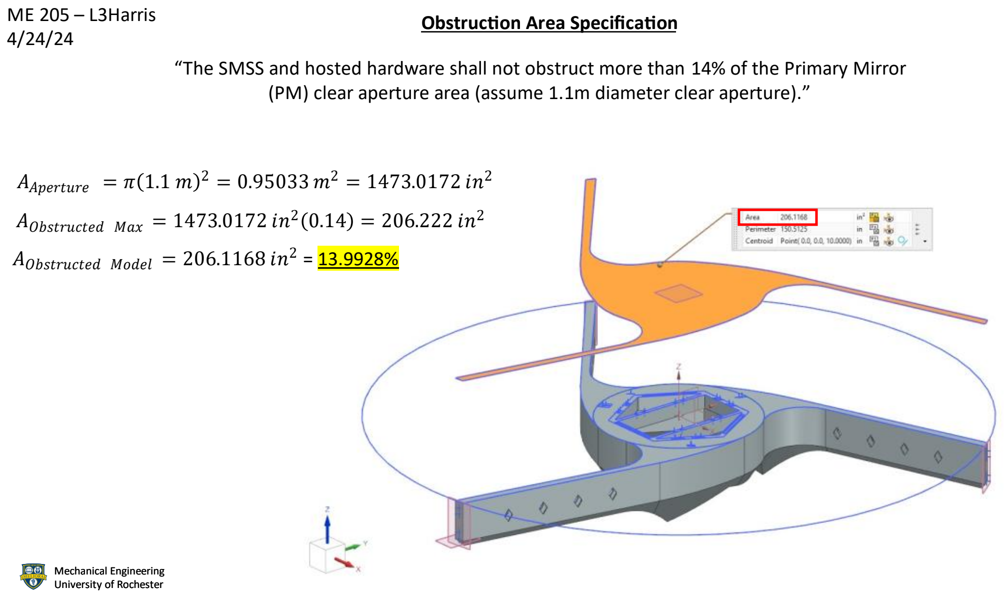

ME 205 – L3Harris
4/24/24

Obstruction Area Specification

"The SMSS and hosted hardware shall not obstruct more than 14% of the Primary Mirror (PM) clear aperture area (assume 1.1m diameter clear aperture)."

$$A_{Aperture} = \pi(1.1\,m)^2 = 0.95033\,m^2 = 1473.0172\,in^2$$

$$A_{Obstructed\ \ Max} = 1473.0172\,in^2(0.14) = 206.222\,in^2$$

$$A_{Obstructed\ \ Model} = 206.1168\,in^2 = 13.9928\%$$

Area	206.1168	in^2
Perimeter	150.5125	in
Centroid	Point(0.0, 0.0, 10.0000)	in

Mechanical Engineering
University of Rochester

Figure 63. Verification of Obstruction Area Specification

ME 205 – L3Harris
4/24/24

Modal Analysis – Solution 103: Real Eigenvalue

1st Mode Displacement

Mode 1 = 123.38 Hz

1st Mode Strain Energy Density

Highest strain energy density underneath SMSS where draft extrusions meet at hex vertices.

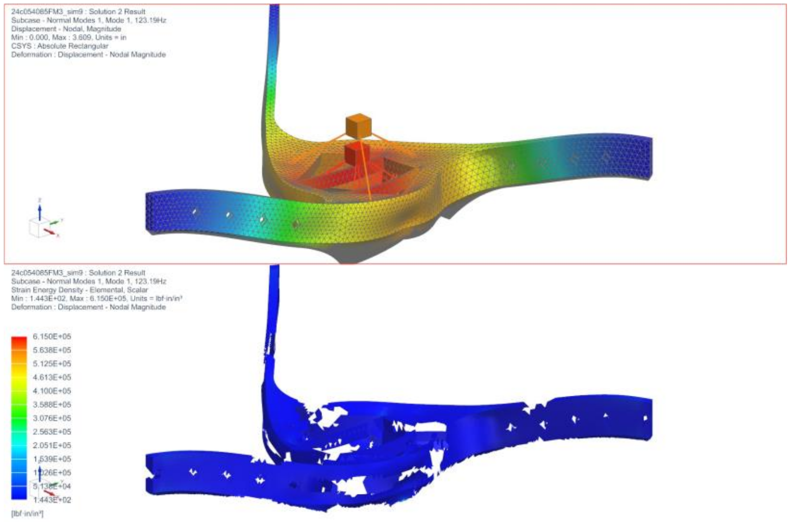

Figure 64. First Mode of the Final Model Found Using Solution 103 in NX

ME 205 – L3Harris
4/24/24

Yield Stress Margin of Safety Computations

Von Mises Element Nodal Stresses – Maximum Values Across All Nodes

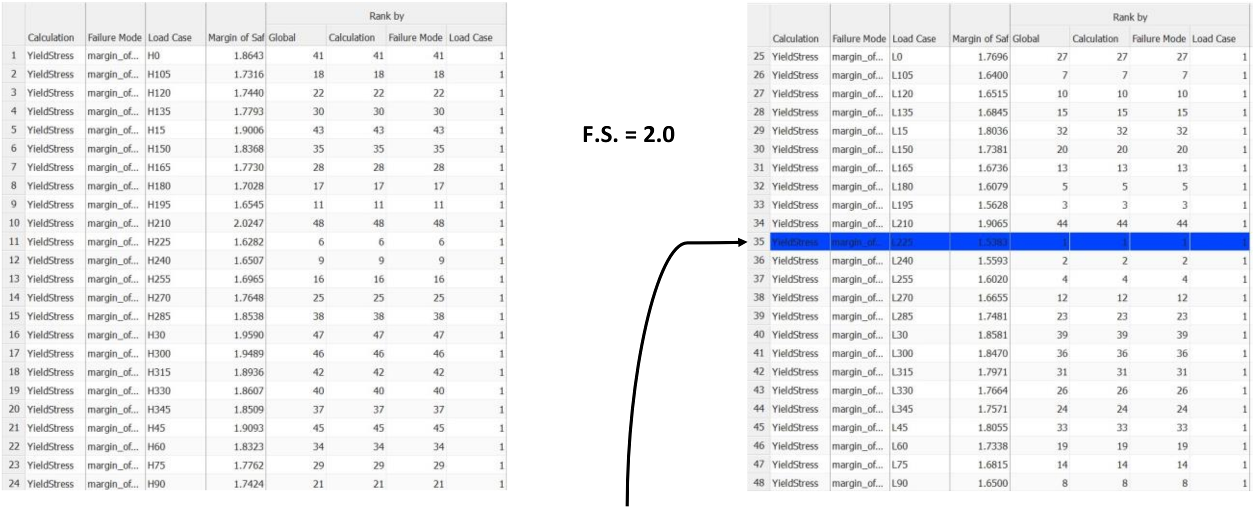

	Calculation	Failure Mode	Load Case	Margin of Saf	Rank by			
					Global	Calculation	Failure Mode	Load Case
1	YieldStress	margin_of...	H0	1.8643	41	41	41	1
2	YieldStress	margin_of...	H105	1.7316	18	18	18	1
3	YieldStress	margin_of...	H120	1.7440	22	22	22	1
4	YieldStress	margin_of...	H135	1.7793	30	30	30	1
5	YieldStress	margin_of...	H15	1.9006	43	43	43	1
6	YieldStress	margin_of...	H150	1.8368	35	35	35	1
7	YieldStress	margin_of...	H165	1.7730	28	28	28	1
8	YieldStress	margin_of...	H180	1.7028	17	17	17	1
9	YieldStress	margin_of...	H195	1.6545	11	11	11	1
10	YieldStress	margin_of...	H210	2.0247	48	48	48	1
11	YieldStress	margin_of...	H225	1.6282	6	6	6	1
12	YieldStress	margin_of...	H240	1.6507	9	9	9	1
13	YieldStress	margin_of...	H255	1.6965	16	16	16	1
14	YieldStress	margin_of...	H270	1.7648	25	25	25	1
15	YieldStress	margin_of...	H285	1.8538	38	38	38	1
16	YieldStress	margin_of...	H30	1.9590	47	47	47	1
17	YieldStress	margin_of...	H300	1.9489	46	46	46	1
18	YieldStress	margin_of...	H315	1.8936	42	42	42	1
19	YieldStress	margin_of...	H330	1.8607	40	40	40	1
20	YieldStress	margin_of...	H345	1.8509	37	37	37	1
21	YieldStress	margin_of...	H45	1.9093	45	45	45	1
22	YieldStress	margin_of...	H60	1.8323	34	34	34	1
23	YieldStress	margin_of...	H75	1.7762	29	29	29	1
24	YieldStress	margin_of...	H90	1.7424	21	21	21	1
25	YieldStress	margin_of...	L0	1.7696	27	27	27	1
26	YieldStress	margin_of...	L105	1.6400	7	7	7	1
27	YieldStress	margin_of...	L120	1.6515	10	10	10	1
28	YieldStress	margin_of...	L135	1.6845	15	15	15	1
29	YieldStress	margin_of...	L15	1.8036	32	32	32	1
30	YieldStress	margin_of...	L150	1.7381	20	20	20	1
31	YieldStress	margin_of...	L165	1.6736	13	13	13	1
32	YieldStress	margin_of...	L180	1.6079	5	5	5	1
33	YieldStress	margin_of...	L195	1.5628	3	3	3	1
34	YieldStress	margin_of...	L210	1.9065	44	44	44	1
35	YieldStress	margin_of...	L225	1.5383	1	1	1	1
36	YieldStress	margin_of...	L240	1.5593	2	2	2	1
37	YieldStress	margin_of...	L255	1.6020	4	4	4	1
38	YieldStress	margin_of...	L270	1.6655	12	12	12	1
39	YieldStress	margin_of...	L285	1.7481	23	23	23	1
40	YieldStress	margin_of...	L30	1.8581	39	39	39	1
41	YieldStress	margin_of...	L300	1.8470	36	36	36	1
42	YieldStress	margin_of...	L315	1.7971	31	31	31	1
43	YieldStress	margin_of...	L330	1.7664	26	26	26	1
44	YieldStress	margin_of...	L345	1.7571	24	24	24	1
45	YieldStress	margin_of...	L45	1.8055	33	33	33	1
46	YieldStress	margin_of...	L60	1.7338	19	19	19	1
47	YieldStress	margin_of...	L75	1.6815	14	14	14	1
48	YieldStress	margin_of...	L90	1.6500	8	8	8	1

F.S. = 2.0

Lowest Margin = 1.5383 (low temperature, 225° from +XC)

Figure 65. Margin of Safety Calculation for Yield Stress Using Solution 101 in NX

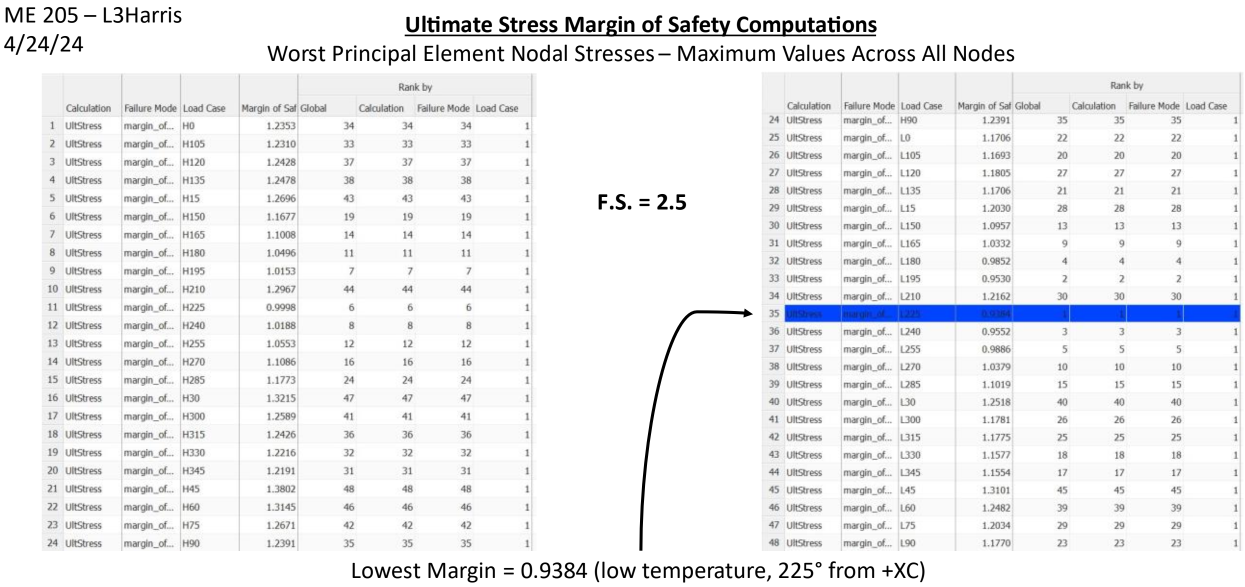

ME 205 – L3Harris
4/24/24

Ultimate Stress Margin of Safety Computations

Worst Principal Element Nodal Stresses – Maximum Values Across All Nodes

	Calculation	Failure Mode	Load Case	Margin of Saf	Rank by Global	Rank by Calculation	Rank by Failure Mode	Rank by Load Case
1	UltStress	margin_of...	H0	1.2353	34	34	34	1
2	UltStress	margin_of...	H105	1.2310	33	33	33	1
3	UltStress	margin_of...	H120	1.2428	37	37	37	1
4	UltStress	margin_of...	H135	1.2478	38	38	38	1
5	UltStress	margin_of...	H15	1.2696	43	43	43	1
6	UltStress	margin_of...	H150	1.1677	19	19	19	1
7	UltStress	margin_of...	H165	1.1008	14	14	14	1
8	UltStress	margin_of...	H180	1.0496	11	11	11	1
9	UltStress	margin_of...	H195	1.0153	7	7	7	1
10	UltStress	margin_of...	H210	1.2967	44	44	44	1
11	UltStress	margin_of...	H225	0.9998	6	6	6	1
12	UltStress	margin_of...	H240	1.0188	8	8	8	1
13	UltStress	margin_of...	H255	1.0553	12	12	12	1
14	UltStress	margin_of...	H270	1.1086	16	16	16	1
15	UltStress	margin_of...	H285	1.1773	24	24	24	1
16	UltStress	margin_of...	H30	1.3215	47	47	47	1
17	UltStress	margin_of...	H300	1.2589	41	41	41	1
18	UltStress	margin_of...	H315	1.2426	36	36	36	1
19	UltStress	margin_of...	H330	1.2216	32	32	32	1
20	UltStress	margin_of...	H345	1.2191	31	31	31	1
21	UltStress	margin_of...	H45	1.3802	48	48	48	1
22	UltStress	margin_of...	H60	1.3145	46	46	46	1
23	UltStress	margin_of...	H75	1.2671	42	42	42	1
24	UltStress	margin_of...	H90	1.2391	35	35	35	1

F.S. = 2.5

	Calculation	Failure Mode	Load Case	Margin of Saf	Rank by Global	Rank by Calculation	Rank by Failure Mode	Rank by Load Case
24	UltStress	margin_of...	H90	1.2391	35	35	35	1
25	UltStress	margin_of...	L0	1.1706	22	22	22	1
26	UltStress	margin_of...	L105	1.1693	20	20	20	1
27	UltStress	margin_of...	L120	1.1805	27	27	27	1
28	UltStress	margin_of...	L135	1.1706	21	21	21	1
29	UltStress	margin_of...	L15	1.2030	28	28	28	1
30	UltStress	margin_of...	L150	1.0957	13	13	13	1
31	UltStress	margin_of...	L165	1.0332	9	9	9	1
32	UltStress	margin_of...	L180	0.9852	4	4	4	1
33	UltStress	margin_of...	L195	0.9530	2	2	2	1
34	UltStress	margin_of...	L210	1.2162	30	30	30	1
35	UltStress	margin_of...	L225	0.9384	1	1	1	1
36	UltStress	margin_of...	L240	0.9552	3	3	3	1
37	UltStress	margin_of...	L255	0.9886	5	5	5	1
38	UltStress	margin_of...	L270	1.0379	10	10	10	1
39	UltStress	margin_of...	L285	1.1019	15	15	15	1
40	UltStress	margin_of...	L30	1.2518	40	40	40	1
41	UltStress	margin_of...	L300	1.1781	26	26	26	1
42	UltStress	margin_of...	L315	1.1775	25	25	25	1
43	UltStress	margin_of...	L330	1.1577	18	18	18	1
44	UltStress	margin_of...	L345	1.1554	17	17	17	1
45	UltStress	margin_of...	L45	1.3101	45	45	45	1
46	UltStress	margin_of...	L60	1.2482	39	39	39	1
47	UltStress	margin_of...	L75	1.2034	29	29	29	1
48	UltStress	margin_of...	L90	1.1770	23	23	23	1

Lowest Margin = 0.9384 (low temperature, 225° from +XC)

Figure 66. Margin of Safety Calculation for Ultimate Stress Using Solution 101 in NX

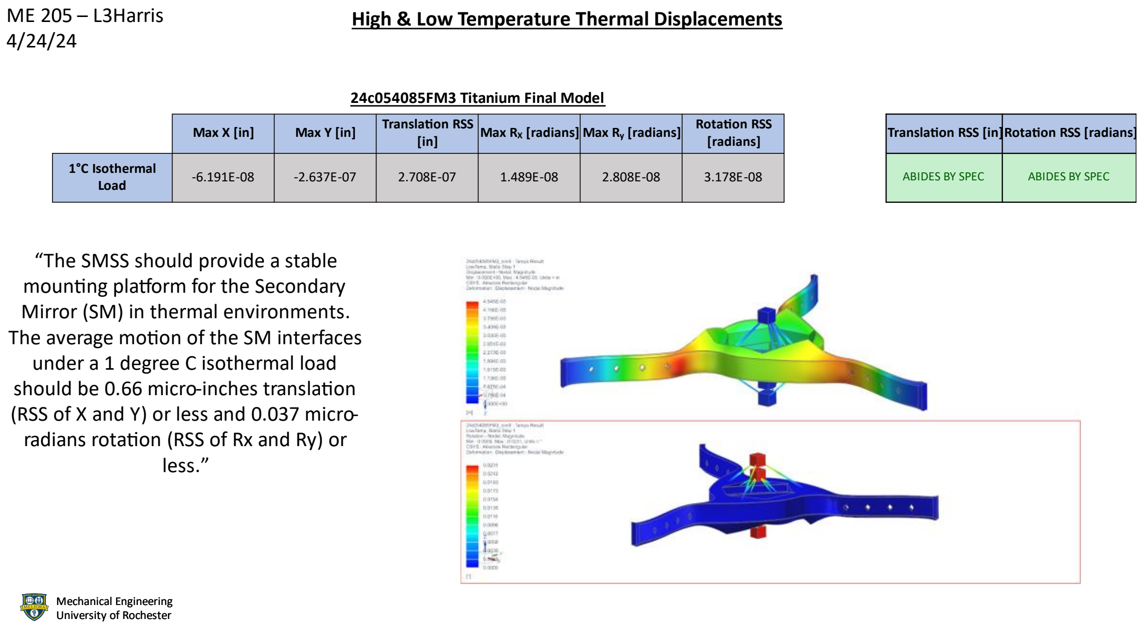

ME 205 – L3Harris
4/24/24

High & Low Temperature Thermal Displacements

24c054085FM3 Titanium Final Model

	Max X [in]	Max Y [in]	Translation RSS [in]	Max R_X [radians]	Max R_Y [radians]	Rotation RSS [radians]
1°C Isothermal Load	-6.191E-08	-2.637E-07	2.708E-07	1.489E-08	2.808E-08	3.178E-08

Translation RSS [in]	Rotation RSS [radians]
ABIDES BY SPEC	ABIDES BY SPEC

"The SMSS should provide a stable mounting platform for the Secondary Mirror (SM) in thermal environments. The average motion of the SM interfaces under a 1 degree C isothermal load should be 0.66 micro-inches translation (RSS of X and Y) or less and 0.037 micro-radians rotation (RSS of Rx and Ry) or less."

Mechanical Engineering
University of Rochester

Figure 67. Verification of Thermal Translation of Secondary Mirror Specification Using Solution 101 in NX.

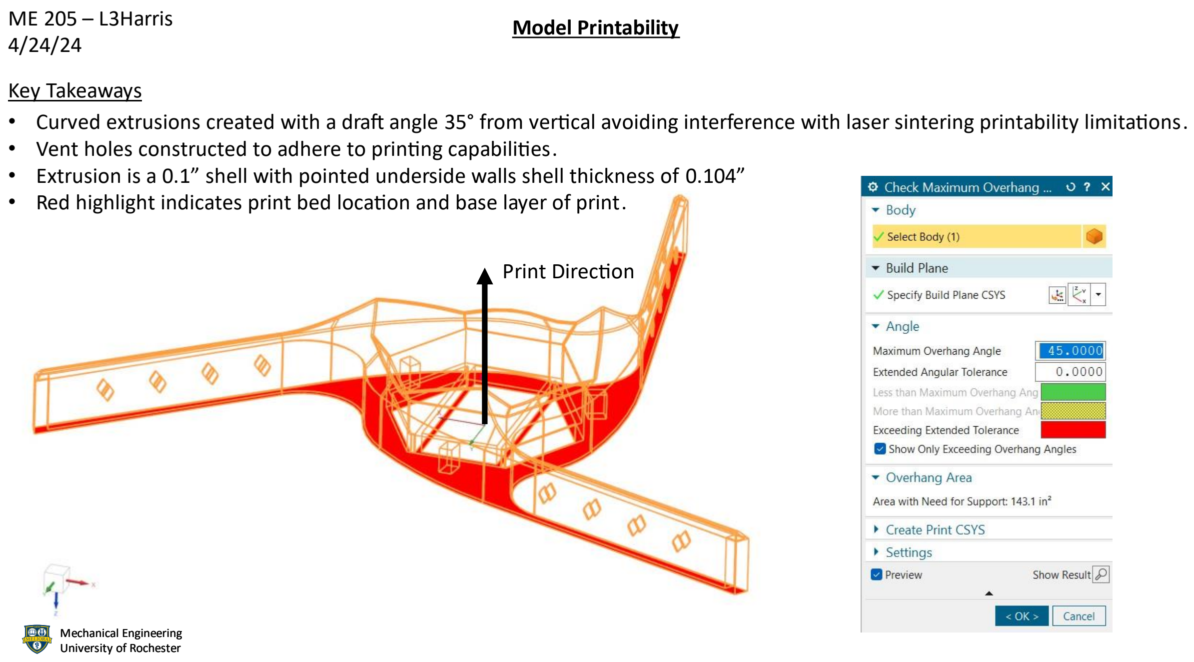

ME 205 – L3Harris
4/24/24

Model Printability

Key Takeaways

- Curved extrusions created with a draft angle 35° from vertical avoiding interference with laser sintering printability limitations.
- Vent holes constructed to adhere to printing capabilities.
- Extrusion is a 0.1” shell with pointed underside walls shell thickness of 0.104”
- Red highlight indicates print bed location and base layer of print.

✓ Select Body (1)
✓ Specify Build Plane CSYS
Maximum Overhang Angle 45.0000
Extended Angular Tolerance 0.0000
Less than Maximum Overhang Ang 🟩
More than Maximum Overhang An 🟨
Exceeding Extended Tolerance 🟥
☑ Show Only Exceeding Overhang Angles
Area with Need for Support: 143.1 in^2
☑ Preview

Figure 68. Verification of Printability Using Powder Bed Printing Using NX’s Maximum Overhang Angle Tool.

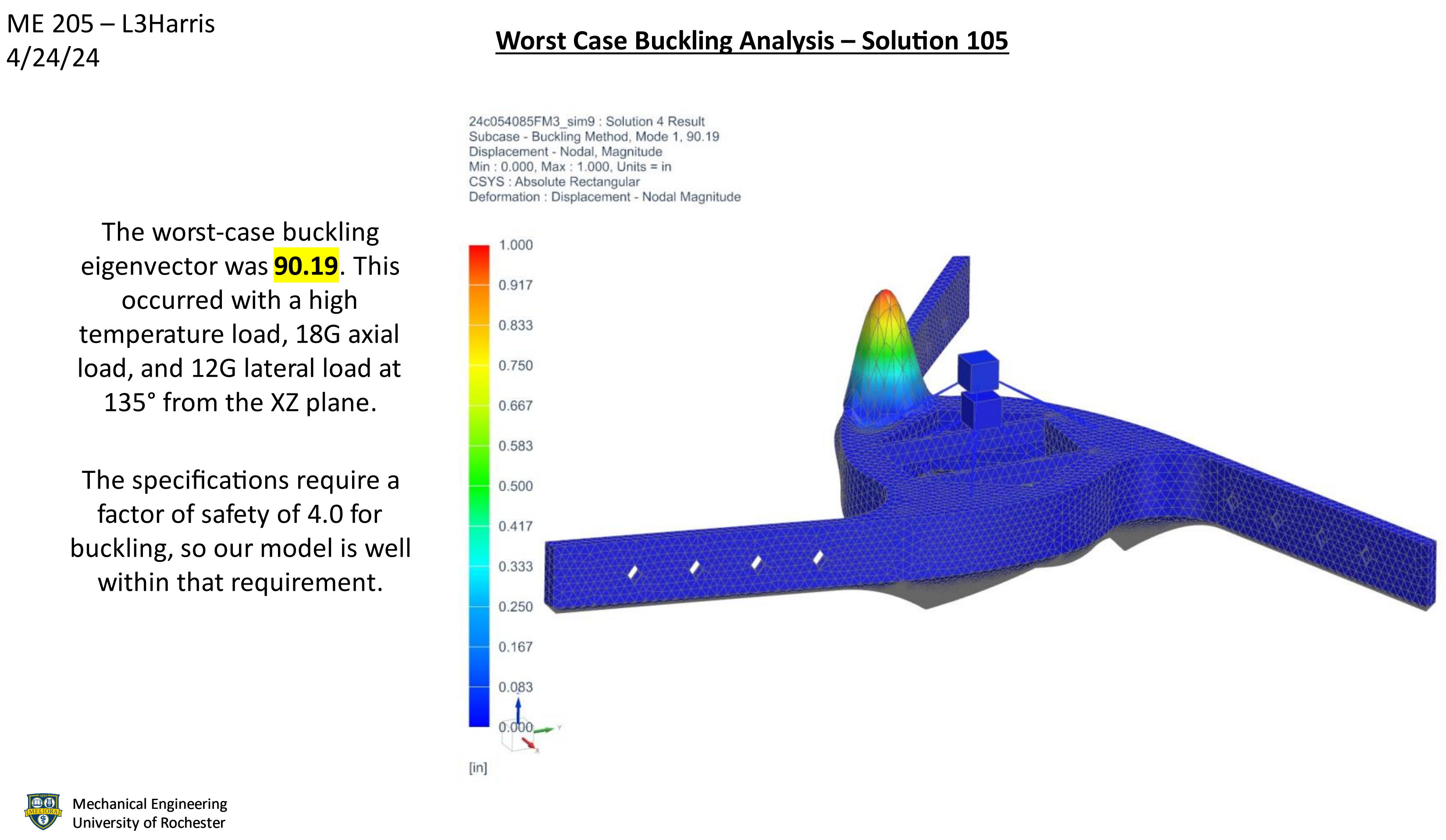

ME 205 – L3Harris
4/24/24

Worst Case Buckling Analysis – Solution 105

The worst-case buckling eigenvector was **90.19**. This occurred with a high temperature load, 18G axial load, and 12G lateral load at 135° from the XZ plane.

The specifications require a factor of safety of 4.0 for buckling, so our model is well within that requirement.

```
24c054085FM3_sim9 : Solution 4 Result
Subcase - Buckling Method, Mode 1, 90.19
Displacement - Nodal, Magnitude
Min : 0.000, Max : 1.000, Units = in
CSYS : Absolute Rectangular
Deformation : Displacement - Nodal Magnitude
```

Mechanical Engineering
University of Rochester

Figure 69. Verification of Positive Margin of Safety Against Buckling Using Solution 105 in NX.

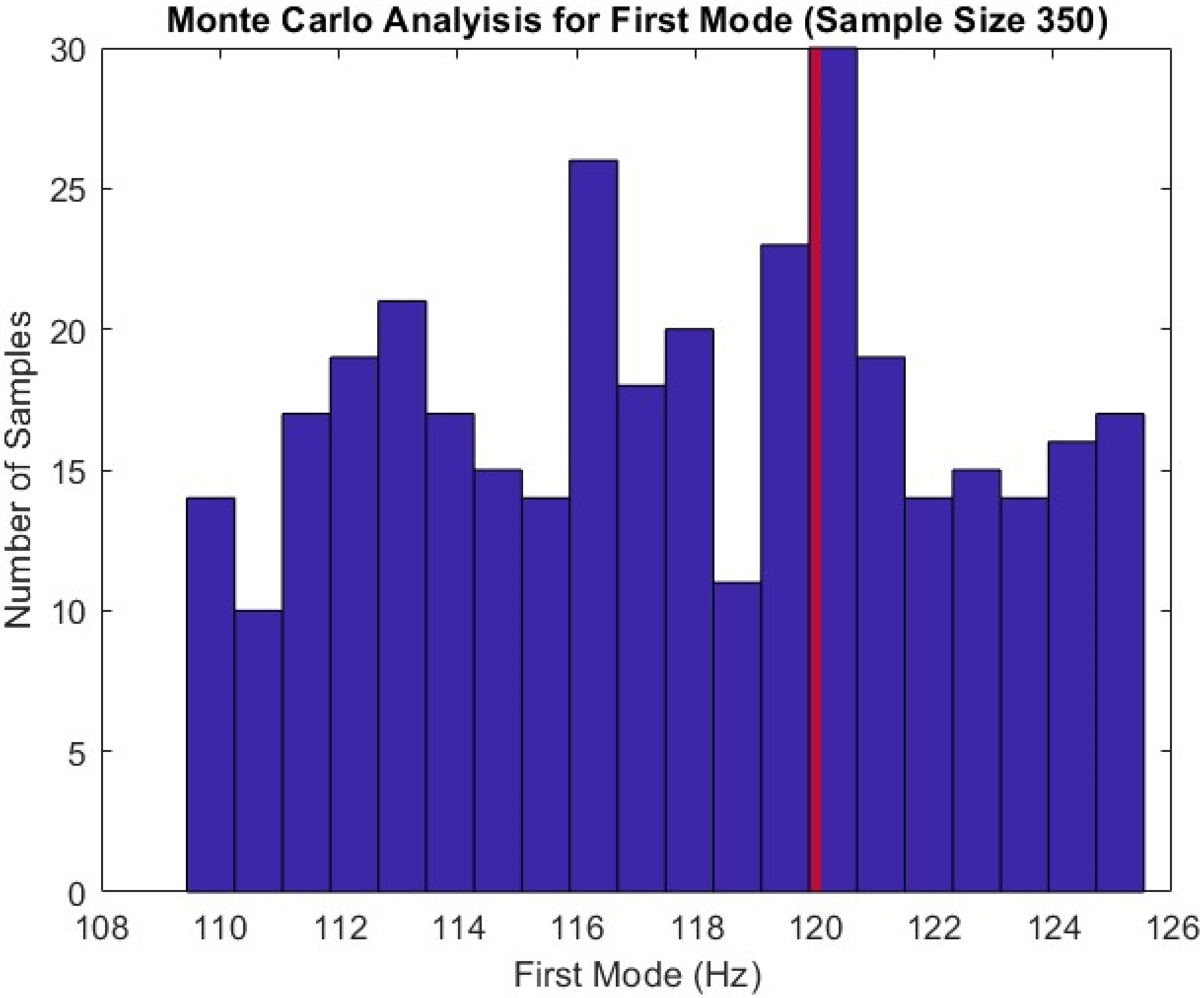

Figure 70. Histogram From Monte Carlo Analysis Showing the Distribution of First Modes

APPENDIX D

INTELLECTUAL PROPERTY

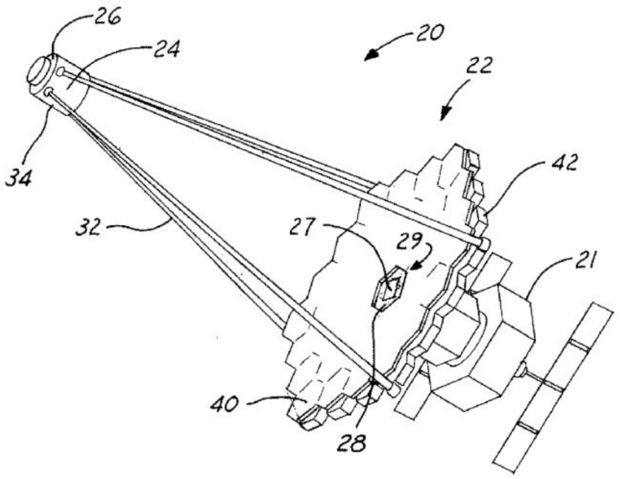

Figure 1. Patent Search Example 1, Patented Design by the Boeing Company (US 9823459B2).

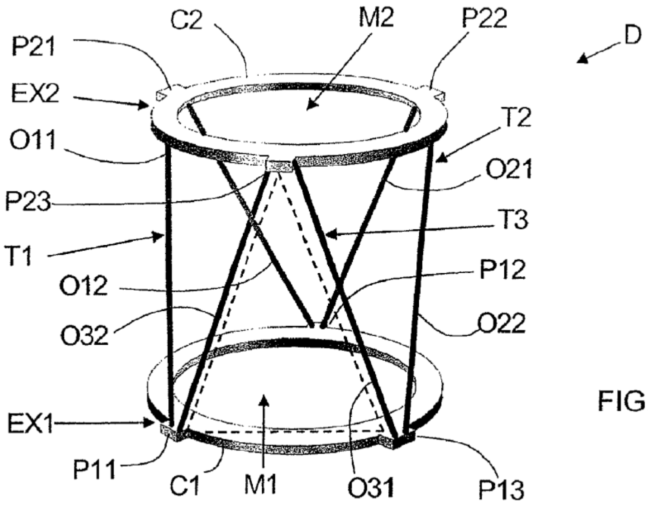

FIG.4

Figure 2. Patent search example 2, patented design by the Thales Company (US 8,186,121 B2).

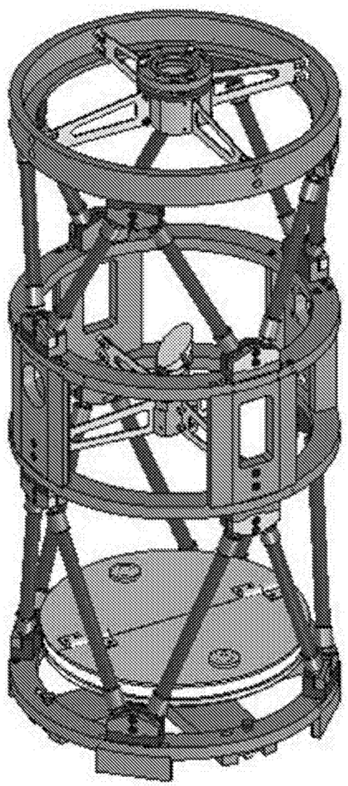

Figure 3. Patent Search Example 3, Application Number 201610208574.7.

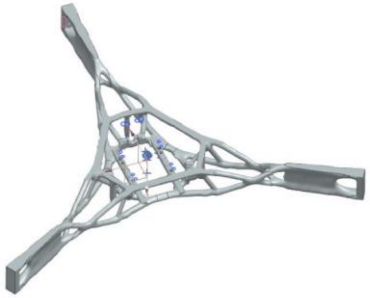

Figure 4. 2022’s L3 Harris Capstone Project Design

Figure 5. 2023’s L3 Harris Capstone Project Design